

FEDERAL UNIVERSITY OF ABC
NANOSCIENCE AND ADVANCED MATERIALS GRADUATE PROGRAM

Asaph Armando Jacinto

**NANOCELLULOSE EXTRACTED FROM DIFFERENT CELLULOSE SOURCES
USING HIGH INTENSITY ULTRASOUND**

Santo André – SP

2020

Asaph Armando Jacinto

**NANOCELLULOSE EXTRACTED FROM DIFFERENT CELLULOSE SOURCES
USING HIGH INTENSITY ULTRASOUND**

Dissertation submitted to the Nanoscience and Advanced Materials Graduate Program of Federal University of ABC in partial fulfillment of the requirements for the degree of Doctor of Philosophy in Nanoscience and Advanced Materials. Research line: Nanosciences and Nanotechnology

Advisor: Prof. Dr. Márcia Aparecida da Silva Spinacé

Santo André – SP

2020

Sistema de Bibliotecas da Universidade Federal do ABC
Elaborada pelo Sistema de Geração de Ficha Catalográfica da UFABC
com os dados fornecidos pelo(a) autor(a).

Jacinto, Asaph Armando

Nanocellulose extracted from different cellulose sources using high intensity ultrasound / Asaph Armando Jacinto. — 2020.

127 fls.

Orientadora: Márcia Aparecida da Silva Spinacé

Tese (Doutorado) — Universidade Federal do ABC, Programa de Pós-Graduação em Nanociências e Materiais Avançados, Santo André, 2020.

1. Nanocelulose. 2. Ultrassom de alta intensidade. 3. Celulose bacteriana. 4. Curauá e Bagaço de cana de açúcar. 5. Viscose. I. Spinacé, Márcia Aparecida da Silva. II. Programa de Pós-Graduação em Nanociências e Materiais Avançados, 2020. III. Título.

Este exemplar foi revisado e alterado em relação à versão original, de acordo com as observações levantadas pela banca no dia da defesa, sob responsabilidade única do(a) autor(a) e com a anuência do(a) orientador(a).

Santo André/SP



30

de

março

de

2020

Assinatura do(a) autor(a):

Asaph Armando Jacinto

Assinatura do(a) orientador(a):

Marcos J. Spinozi



MINISTÉRIO DA EDUCAÇÃO

Fundação Universidade Federal do ABC

Avenida dos Estados, 5001 – Bairro Santa Terezinha – Santo André – SP
CEP 09210-580 · Fone: (11) 4996-0017

FOLHA DE ASSINATURAS

Assinaturas dos membros da Banca Examinadora que avaliou e aprovou a Defesa de Tese de Doutorado do candidato, ASAPH ARMANDO JACINTO realizada em 20 de Fevereiro de 2020:

Prof.(a) EDILENE DE CASSIA DUTRA NUNES
ESCOLA SENAI MARIO AMATO

Prof.(a) JEAN JACQUES BONVENT
UNIVERSIDADE FEDERAL DO ABC

Prof.(a) JULIANA DA SILVA BERNARDES
LABORATÓRIO NACIONAL DE NANOTECNOLOGIA

Prof.(a) LIGIA PASSOS MAIA
UNIVERSIDADE FEDERAL DO ABC

Prof.(a) DANILO MARIN FERMINO
CENTRO ESTADUAL DE EDUCAÇÃO TECNOLÓGICA PAULA SOUZA

Prof.(a) MATHILDE JULIENNE GISELE CHAMPEAU FERREIRA
UNIVERSIDADE FEDERAL DO ABC

Prof.(a) MARCIA APARECIDA DA SILVA SPINACE
UNIVERSIDADE FEDERAL DO ABC - Presidente

* Por ausência do membro titular, foi substituído pelo membro suplente descrito acima: nome completo, instituição e assinatura



Universidade Federal do ABC

ACKNOWLEDGMENTS

I am thankful to my LORD and God, to my wife (Jessica), to my family (Helen, Gemima and all the others), to my friends, especially those from Grupo de Estudos Bíblicos da UFABC (Aliança Bíblica Universitária - ABU).

I also would like to express my gratitude to my advisor, Dr. Márcia Aparecida da Silva Spinacé. As well as to undergraduate and graduate students who are part of her research group and laboratory.

I am grateful to the students and professors from the Laboratório de Cristalografia e Caracterização Estrutural de Materiais (LCCEM), at the Federal University of ABC. Mainly to the professors Dr. Jean-Jacques Bonvent and Dr. Fernando Giacomelli together with their graduate students, by the support in DLS measurements. And also to the Multiuser Central Facilities (UFABC) as well as to the LNNano - Brazilian Nanotechnology National Laboratory (CNPEM/MCTIC) for their experimental support.

This study was financed in part by the Coordenação de Aperfeiçoamento de Pessoal de Nível Superior – Brasil (CAPES) – Finance Code 001 (proc. 23038.009634/2016-71).

I am also thankful to the São Paulo State Research Foundation (FAPESP, proc. 10/17804-7) for the support of prof. Spinacé's laboratory.

“The end of a matter is better than its beginning and patience is better than pride”

Ecclesiastes 7:8, Holy Bible

ABSTRACT

Cellulosic nanomaterials (nanocellulose) has gained much attention, especially for applications to reinforce polymeric nanocomposites. They can be extracted using several techniques, such as high intensity ultrasound (HIUS) using only water as solvent. HIUS was applied on different cellulose sources (residues of bacterial cellulose membrane, curaua, sugarcane bagasse and viscose residue) in distinct conditions, evaluating mass and time effects. The materials were characterized by XRD, optical microscopy, FT-IR, FT-Raman, SEM, TEM, DLS, AFM, AFM-IR and TGA. HIUS leaded to a higher crystallinity index, mainly to curaua samples (where crystallinity index increased from 89.7 to 93.8 5). It was possible to obtain nanocellulose from all sources in all conditions, but a mixture of particles of micro and nano scales were obtained for curaua, sugarcane bagasse and viscose residue. The energy consumption of the best sonication condition (140 MWh/ton), using 2 g of bacterial cellulose in 150 mL of water during 45 min, reported the lowest value among the literature of nanocellulose from HIUS until now. Thereby, the nanocellulose extracted by HIUS in this project shows the potential to be applied as reinforcement in nanocomposites.

Keywords: Nanocellulose; High intensity ultrasound; Bacterial cellulose; Curaua; Sugarcane Bagasse; Viscose.

RESUMO

O interesse pelos nanomateriais de celulose (nanocelulose) para reforço em nanocompósitos poliméricos tem crescido. Eles podem ser obtidos por diversas técnicas, como, por exemplo, o ultrassom de alta intensidade (HIUS), usando apenas água como solvente. A extração de nanocelulose a partir de diferentes fontes de celulose (resíduos de membrana de celulose bacteriana, curauá, bagaço de cana de açúcar e resíduo de viscose) foi estudada, avaliando os efeitos da massa e do tempo de sonificação nas propriedades do nanomaterial. As amostras foram caracterizadas por DRX, microscopia óptica, FT-IR, FT-Raman, MEV, MET, DLS, AFM, AFM-IR e TGA. O HIUS promoveu um aumento no índice de cristalinidade, especialmente para as amostras de curauá (onde o índice de cristalinidade aumentou de 89,7 para 93,8 %). Foi possível extrair nanomateriais de todas as fontes, em todas as condições testadas, porém foi observada uma mistura de partículas micro e nanométricas em amostras de curauá, bagaço de cana e resíduo de viscose. O consumo energético na melhor condição de extração (140 MWh/ton), que usou 2 g de celulose bacteriana em 150 mL de água durante 45 min, resultou no menor valor publicado na literatura de nanocelulose por HIUS. Portanto, a nanocelulose extraída pelo HIUS neste trabalho apresenta o potencial para ser aplicada como reforço em nanocompósitos poliméricos.

Palavras-chave: Nanocelulose; Ultrassom de alta intensidade; Celulose bacteriana; Curauá; Bagaço de cana de açúcar; Viscose.

LIST OF FIGURES

Figure 1 - Papers published between 1995 and 2017 about composite and cellulose on Web of Science.	1
Figure 2 - Unit repetition of cellulose.	2
Figure 3 - Structural organization of cellulose in plants, such as the pineapple leaf.	4
Figure 4 - Scheme of unit cells for cellulose I α (dashed line) and I β (solid line).	7
Figure 5 - Macromolecule of cellulose with grafted sulfate group due to hydrolysis with sulfuric acid.	10
Figure 6 - Scheme of HIUS system to extract nanocellulose.	12
Figure 7 - Most used methods to extract nanocellulose published in Brazilian papers available in the Web of Science database.	17
Figure 8 - Cellulose sources as received: bacterial cellulose, residues of viscose, curaua and sugarcane bagasse.	19
Figure 9 - Image HIUS system used for sonication of BC _{raw} , VR _{raw} , SCB _{raw} and C _{raw} samples.	20
Figure 10 - Sequence of steps followed in this Dissertation.	23
Figure 11 - FTIR spectra of bacterial cellulose before (BC _{raw}) and after sonication (BC1, BC2, BC3 and BC4) from: (A) 4000 - 650 cm ⁻¹ and (B) 2000 - 1250 cm ⁻¹	28
Figure 12 - FTIR spectra of viscose residues before (VR _{raw}) and after sonication (VR1, VR2, VR3 and VR4) from: (A) 4000 - 650 cm ⁻¹ and (B) 2000 - 1250 cm ⁻¹	30
Figure 13 - FTIR spectra of curaua before (C _{raw}) and after sonication (C1, C2, C3 and C4) from: (A) 4000 - 650 cm ⁻¹ and (B) 2000 - 1250 cm ⁻¹ ; and FTIR spectra of sugarcane bagasse before (SCB _{raw}) and after sonication (SCB1, SCB2, SCB3 and SCB4) from: (C) 4000 - 650 cm ⁻¹ and (D) 2000 - 1250 cm ⁻¹	33
Figure 14 - FTIR relative intensities of curaua (A) and sugarcane bagasse (B) before and after sonication.	34
Figure 15 - AFM-IR (contact mode) of C3: topography (A), IR spectra (B) and mapping at 1744 cm ⁻¹ (C).	35
Figure 16 - AFM-IR (contact mode) of SCB3: topography (A) and IR spectra (B).	37
Figure 17 - Representative diffractograms of bacterial cellulose before (BC _{raw} (A)) and after sonication: BC1 (B), BC2 (C) BC3 (D) and BC4 (E).	39
Figure 18 - Raman spectra of viscose before (VR _{raw}) and after sonication (VR1, VR2, VR3 and VR4).	41

Figure 19 - Representative diffractograms of viscose residues before (VR_{raw} (A)) and after sonication: VR1 (B), VR2 (C), VR3 (D) and VR4 (E).	43
Figure 20 - Representative diffractograms of curaua before (C_{raw} (A)) and after sonication: C1 (B), C2 (C) C3 (D) and C4 (E).	45
Figure 21 - Representative diffractograms of sugarcane bagasse before (SCB_{raw} (A)) and after sonication: SCB1 (B), SCB2 (C) SCB3 (D) and SCB4 (E).	46
Figure 22 - Average of crystallinity indexes as a function of raw materials and their sonicated samples with mass loading (0.1 or 0.2 g) and sonication time (45 or 70 min).	49
Figure 23 - SEM micrograph of bacterial cellulose before sonication (BC_{raw}) at x50 (A), x100 (B), x500 (C) and x1000 (D).	52
Figure 24 - AFM micrographs (contact mode) of bacterial cellulose before sonication (BC_{raw}): topography (A, B) and friction (C, D); distribution histogram of diameter measured by AFM (E).	53
Figure 25 - DLS intensity distribution of sonicated samples of bacterial cellulose.	54
Figure 26 - AFM micrographs (contact mode) of sonicated bacterial cellulose BC3: topography (A, B) and friction (C, D); distribution histogram of diameter measured by AFM (E).	55
Figure 27 - Distribution histograms of length (A) and diameter (B) for viscose residues before sonication (VR_{raw}).	56
Figure 28 - SEM example of viscose residues before sonication (VR_{raw}) at x50 (A), x100 (B), x500 (C) and x1000 (D).	57
Figure 29 - DLS intensity distribution of sonicated samples of viscose residues.	58
Figure 30 - SEM micrograph at x100 of sonicated viscose residue VR3.	58
Figure 31 - TEM micrographs of sonicated viscose residue VR3 (A, B) and distribution histograms of length (C) and diameter (D) measured using all TEM micrographs for VR3.	60
Figure 32 - Distribution histograms of length (A,C) and diameter (B,D) for curaua (C_{raw} (A,B)) and sugarcane bagasse (SCB_{raw} (C,D)) before sonication.	61
Figure 33 - SEM micrograph of curaua before sonication (C_{raw}) at x50 (A), x100 (B), x500 (C) and x1000 (D).	62
Figure 34 - SEM micrograph of sugarcane bagasse before sonication (SCB_{raw}) at x50 (A), x100 (B), x500 (C) and x1000 (D).	63
Figure 35 - DLS intensity distribution of sonicated samples of curaua (A) and sugarcane bagasse (B).	64

Figure 36 - SEM micrograph at x100 of sonicated: curaua C3 (A) and sugarcane bagasse SCB3 (B).....	65
Figure 37 - TEM micrographs of sonicated: curaua C3 (A, B) and sugarcane bagasse SCB3 (C, D).....	66
Figure 38 - Distribution histograms of length (A,C) and diameter (B,D) measured using all TEM micrographs for C3 (A,B) and SCB3 (C,D).....	67
Figure 39 - Average length (A), average diameter (B) and aspect ratio L/D (C) of raw materials: curaua (C_{raw}), sugarcane bagasse (SCB_{raw}) and viscose residue (VR_{raw}).....	69
Figure 40 - Average of main peaks of hydrodynamic radius observed in DLS measurements after sonication.....	70
Figure 41 - TGA (A) and DTG (B) of bacterial cellulose before (BC_{raw}) and after sonication (BC1, BC2, BC3 and BC4).	71
Figure 42 - TGA (A) and DTG (B) of viscose residues before (VR_{raw}) and after sonication (VR1, VR2, VR3 and VR4).	73
Figure 43 - TGA (A,C) and DTG (B,D) of: (A,B) curaua before (C_{raw}) and after sonication (C1, C2, C3 and C4); and (C,D) sugarcane bagasse before (SCB_{raw}) and after sonication (SCB1, SCB2, SCB3 and SCB4).....	74
Figure 44 - Values of T_{onset} as a function of raw and sonicated samples.	76
Figure 45 - Energy consumption for extracting nanocellulose as a function of cellulosic material and sonication condition.	78
Figure 46 - Sample of bacterial cellulose BC3-M before and after application of HIUS.....	79
Figure 47 - DLS intensity distribution (A) and TGA and DTG curves (B) of sonicated bacterial cellulose with the highest mass BC3-M (2 g / 45 min).	80
Figure 48 - Examples of micrographs of bacterial cellulose BCraw (A), curaua C _{raw} (B), sugarcane bagasse SCB _{raw} (C) and viscose residue VR _{raw} (D).....	105
Figure 49 - AFM micrographs of topography (contact mode) of sonicated bacterial cellulose BC3.	106
Figure 50 - TEM micrographs of sonicated viscose residue VR3.....	107
Figure 51 - TEM micrographs of sonicated viscose residue VR3.....	108
Figure 52 - TEM micrographs of sonicated curaua C3.....	109
Figure 53 - TEM micrographs of sonicated curaua C3.....	110
Figure 54 - TEM micrographs of sonicated sugarcane bagasse SCB3.	111
Figure 55 - TEM micrographs of sonicated sugarcane bagasse SCB3.	112

LIST OF TABLES

Table 1 - Abbreviation of raw cellulosic materials sonicated by HIUS process.....	20
Table 2 - HIUS conditions.....	21
Table 3 - Contents of lignin, ash and holocellulose (cellulose and hemicellulose) for curaua (C_{raw}) and sugarcane bagasse (SCB_{raw}).....	32
Table 4 - CI values of bacterial cellulose before (BC_{raw}) and after (BC1, BC2, BC3, BC4) sonication.....	40
Table 5 - CI values of viscose residue before (VR_{raw}) and after (VR1, VR2, VR3, VR4) sonication.....	44
Table 6 - CI of curaua (C_{raw}) and sugarcane bagasse (SCB_{raw}) before and after (C1, C2, C3, C4; SCB1, SCB2, SCB3, SCB4) sonication.	47
Table 7 - Main effects of time (t) and mass (m) and interaction effect of combined factors (tm) for crystallinity index of nanocellulose from bacterial cellulose, curaua, sugarcane bagasse and viscose residue.	50
Table 8 - Values of weight averages diameter and length and aspect ratio (L/D) for curaua (C_{raw}) and sugarcane bagasse (SCB_{raw}).....	62
Table 9 - TGA results of bacterial cellulose before (BC_{raw}) and after sonication (BC1, BC2, BC3 and BC4).	71
Table 10 - TGA results of viscose residues before (VR_{raw}) and after sonication (VR1, VR2, VR3 and VR4).	73
Table 11 - TGA results of curaua and before (C_{raw}) and after sonication (C1, C2, C3 and C4) and of sugarcane bagasse before (SCB_{raw}) and after sonication (SCB1, SCB2, SCB3 and SCB4).....	75

SUMMARY

1 INTRODUCTION	1
1.1 Cellulose sources	2
1.2 Cellulose crystallinity	5
1.3 Nanocellulose	8
1.3.1 High intensity ultrasonication (HIUS)	11
1.3.2 Nanocellulose suppliers	14
1.3.3 Nanocellulose applications.....	15
1.4 Motivation	16
2 OBJECTIVES	18
2.1 General objective.....	18
2.2 Specific objectives.....	18
3 EXPERIMENTAL	19
3.1 Materials	19
3.2 HIUS process	20
3.3 Characterization.....	23
3.3.1 Crystallinity	23
3.3.2 Size distribution and morphology.....	24
3.3.3 Chemical composition	25
3.3.4 Thermal properties.....	26
4 RESULTS AND DISCUSSION	28
4.1 Chemical structure of cellulose before and after sonication process	28
4.1.1 Chemical structure of bacterial cellulose	28
4.1.2 Chemical structure of viscose residue	29
4.1.3 Chemical structure of curaua and sugarcane bagasse	31
4.1.4 Comparison of chemical structure among cellulose sources	37
4.2 Crystallinity of cellulose before and after sonication process	38

4.2.1	Crystallinity of bacterial cellulose	38
4.2.2	Crystallinity of viscose residue	41
4.2.3	Crystallinity of curaua and sugarcane bagasse	45
4.2.4	Comparison of crystallinity degree among cellulose sources	49
4.3	Size distribution and morphology of cellulose before and after sonication process	51
4.3.1	Size distribution and morphology of bacterial cellulose.....	51
4.3.2	Size distribution and morphology of viscose Residue.....	56
4.3.3	Size distribution and morphology of curaua and sugarcane bagasse	61
4.3.4	Comparison of size distribution and morphology among cellulose sources.....	68
4.4	Thermal degradation of cellulose before and after sonication process	70
4.4.1	Thermal degradation of bacterial cellulose	70
4.4.2	Thermal degradation of viscose residue.....	72
4.4.3	Thermal degradation of curaua and sugarcane bagasse	74
4.4.4	Comparison of thermal degradation among cellulose sources	76
4.5	Yielding and energy demand of HIUS process to extract nanocellulose	77
5	CONCLUSION.....	82
6	REFERENCES	84
APPENDIX A	– Micrograph of optical microscopy of raw cellulose sources	105
APPENDIX B	– AFM micrograph of sonicated bacterial cellulose BC3.....	106
APPENDIX C	– TEM micrograph of sonicated viscose residue VR3	107
APPENDIX D	– TEM micrograph of sonicated curaua C3.....	109
APPENDIX E	– TEM micrograph of sonicated sugarcane bagasse SCB3	111

1 INTRODUCTION

Petroleum based polymers and polymeric composites are well established and present every day on our society. However, they show some disadvantages, as the uncertainty of long-term petroleum supply, the pollution generated by the wrong disposal of these materials and the increasing of landfills from these wastes (LUO and NETRAVALI, 1999; MOHANTY, MISRA and DRZAL, 2002; KOSHY *et al.*, 2015; MOHANTY *et al.*, 2018).

For these reasons, the replacement of traditional materials of fossil origin by environmentally friendly materials has increased over the last decades. There is a significant increase on research and applications using composites with materials from renewable sources like cellulose (MARSH, 2003; LA MANTIA and MORREALE, 2011; FARUK *et al.*, 2012; RAMESH, PALANIKUMAR and REDDY, 2017; MOHANTY *et al.*, 2018). This is verified also by the number of papers available on Web of Science between 1996 and 2019, searching for “composite” and “cellulose”, Figure 1. The search was carried out on 16 Dec. 2019.

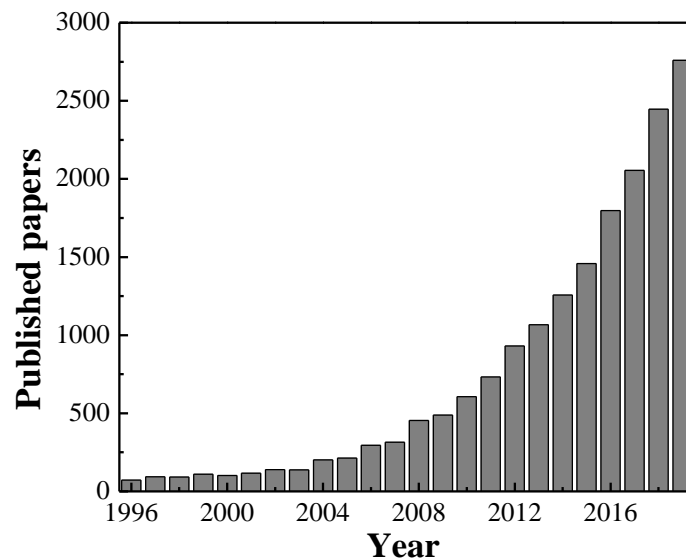


Figure 1 - Papers published between 1995 and 2017 about composite and cellulose on Web of Science.

Cellulose is one of the most available resources on Earth. It is a polysaccharide, with a mer of glucose, Figure 2, and a degree of polymerization usually above 10,000 (NECHYPORCHUK, BELGACEM & BRAS, 2016; SAMIEE *et al.*, 2019). Cellulose shows three hydroxyl groups (-OH) per glucose unit, resulting in its hydrophilic character (KHALIL *et al.*, 2016). It is applied, for example, in applications in the food, textile and biomedical industries, among others (MOON *et al.*, 2011; DURÁN, LEMES and SEABRA, 2012; SHAH *et al.*, 2013; KOUTSIANITIS *et al.*, 2015; MOHANTY *et al.*, 2018).

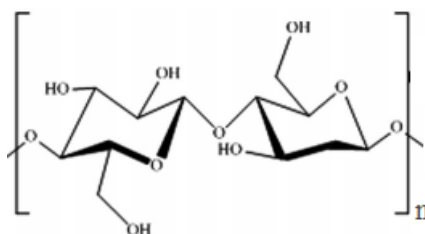


Figure 2 - Unit repetition of cellulose.

1.1 Cellulose sources

Cellulose can be produced by living beings, as animals, algae, bacteria or plants (O'SULLIVAN, 1997; KLEMM *et al.*, 2011; NECHYPORCHUK, BELGACEM & BRAS, 2016; SAMIEE *et al.*, 2019).

Animal cellulose is usually produced by sessile animals, known as tunicates. The diameter of these animals is between 5 and 10 cm and the thickness of the cellulose layer around their skeletal structure is ~1 cm. Its cellulose is present in micrometric aggregates, so a chemical treatment, such as acid hydrolysis, can be used to separate its nanoscale structure (FAVIER, CHANZY and CAVAILLÉ, 1995; KIMURA *et al.*, 2001; HABIBI, CHANZY and VIGNON, 2006; KLEMM *et al.*, 2011; KHANDELWAL and WINDLE, 2014; ZHAO *et al.*, 2015; ZHANG *et al.*, 2017; SAMIEE *et al.*, 2019).

On the other hand, in algae, the synthesis of cellulose microfibrils happens on cell walls. Each species (*e.g.*, *Valonia* or *Cladophora*, and *Micrasterias*) and conditions of cultivation (such as temperature, light availability, nutrients) will produce distinct morphologies and, thereafter, different properties of cellulose. Its aspect ratio can be higher than 40 (VANDERHART and ATALLA, 1984; BROWN JR, 1985; YAMAMOTO and HORII, 1993; KIM *et al.*, 1996; HANLEY *et al.*, 1997; IMAI and SUGIYAMA, 1998; MOON *et al.*, 2011; TERAUCHI *et al.*, 2016; SUCALDITO and CAMACHO, 2017; SAMIEE *et al.*, 2019). However, previous purification is necessary to extract cellulose, in order to remove pigments, pectin and chlorophyll (CHEN *et al.*, 2016; SAMIEE *et al.*, 2019).

Furthermore, there are several nonpathogenic bacteria which are able to produce cellulose. The most usual one is *Acetobacter* or *Gluconobacter*, but there are others, such as *Acanthamoeba* and *Achromobacter* (KLEMM *et al.*, 2005; KLEMM *et al.*, 2011; ESA, TASIRIN and RAHMAN, 2014; SAMIEE *et al.*, 2019). The production happens inside the bacterium and the cell membrane expels the cellulose (JONAS and FARAH, 1998;

REINIATI, HRYMAK and MARGARITIS, 2016). According to the medium culture, to its additives and to mechanical strains that the bacterium can suffer, it is possible to control molar mass, structure and mechanical properties of its cellulose (YAMAMOTO and HORII, 1994; KLEMM *et al.*, 2005; GOELZER *et al.*, 2009; REINIATI, HRYMAK and MARGARITIS, 2016).

The main advantage of cellulose obtained by bacteria is that its production takes some days, while by lignocellulosic fiber can take some years (REINIATI, HRYMAK and MARGARITIS, 2016; SAMIEE *et al.*, 2019). Although its degree of polymerization is lower than the lignocellulosic one (that can be up to 15,000), it isn't constituted by pigments, hemicellulose or lignin (KLEMM *et al.*, 2005; REINIATI, HRYMAK and MARGARITIS, 2016; BOGOLITSYN *et al.*, 2017; SAMIEE *et al.*, 2019). Based on these reasons, bacterial cellulose was one of the selected materials to be studied here.

Moreover, cellulose is found in lignocellulosic fibers, in seeds, stems and leaves of plants. The basic constituents of lignocellulosic fibers are cellulose, hemicellulose and lignin. The cellulose bundles are inside a hemicellulose and lignin matrix (BLEDZKI and GASSAN, 1999; KHALIL *et al.*, 2016; MONTEIRO *et al.*, 2012; RAJINIPRIYA *et al.*, 2018), as indicated in Figure 3. Among adjacent cell wall of plants there is a middle lamella with pectin and each cell itself is constituted by a sequence of concentric layers (KALIA *et al.*, 2011). The outermost layer is called primary wall (IOELOVICH, 2015), which is followed by three layers (S1, S2 and S3) with different angles of orientation of the cellulose microfibrils (KALIA *et al.*, 2011). The inner region is called lumen, which is a central vacuole during the growing of the fiber and it starts to degenerate after maturation of the plant (PRADO, JACINTO and SPINACÉ, 2020).

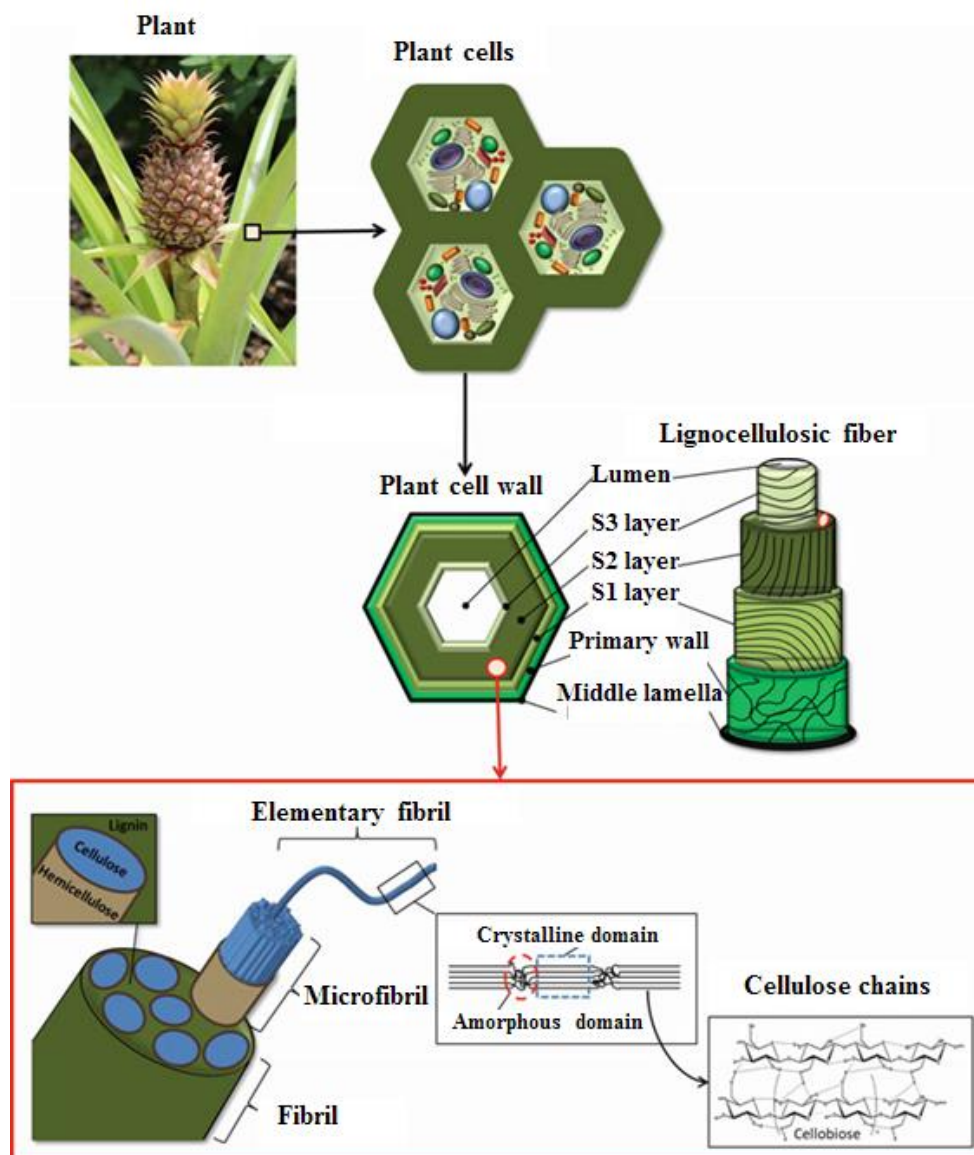


Figure 3 - Structural organization of cellulose in plants, such as the pineapple leaves.
(Adapted from PRADO, JACINTO and SPINACÉ, 2020)

Hemicellulose is an amorphous polymer bonded to cellulose mainly by hydrogen bonds (SPINACÉ *et al.*, 2009; CHANDRA, TAKEUCHI and HASEGAWA, 2012; MONTEIRO *et al.*, 2012). Lignin is also an amorphous macromolecule but with net configuration of random phenyl-propanoic units with different functional groups (CHANDRA, TAKEUCHI and HASEGAWA, 2012; BUSSEMAKER and ZHANG, 2013; SANTUCCI *et al.*, 2016). Their composition changes according to, *e.g.*, plant source, age or climate conditions during the cultivation (FARUK *et al.*, 2012; RAJINIPRIYA *et al.*, 2018).

There are many sources of lignocellulosic fibers, and among them it is possible to highlight curaua and sugarcane. Curaua is a typical plant from the Amazon region (CARASCHI and LEÃO, 2000; MARQUES, GUTIÉRREZ and DEL RÍO, 2007), and its

fiber is an interesting material to reinforce polymeric matrices and to extract nanocellulose because its cellulose content is higher than that of other fibers (CARASCHI and LEÃO, 2000; MARQUES, GUTIÉRREZ and DEL RÍO, 2007; SPINACÉ *et al.*, 2009; CAMPOS *et al.*, 2013). Meanwhile, Brazil is the main producer of sugarcane in the world and the process to obtain 1 ton of this plant generates around 280 kg of bagasse (CERQUEIRA, RODRIGUES FILHO and MEIRELES, 2007; HOFSETZ and SILVA, 2012). The concern about this bagasse disposal in the environment has been growing, because it can lead to microbial deposition, water pollution and even to spontaneous ignition (PURCHASE, ROSETTENSTEIN and BEZUIDENHOUDT, 2013; EGGLESTON and LIMA, 2015; BOONMEE and PONGSAMANA, 2017). In order to avoid these problems, some alternatives have been studied, such as the application of the bagasse to reinforce polymeric matrices (SANTOS *et al.*, 2018). Therefore, curaua and sugarcane bagasse (SCB) were also chosen to be studied in this Dissertation. They are key sources in the Brazilian scenario and they show different amounts of cellulose in their composition.

Finally, there is another cellulose source commercially available. It is known as regenerated cellulose, such as the traditional viscose fibers in the textile industry. This regeneration uses a pretreatment of cellulose from lignocellulosic pulp to reduce its degree of polymerization, followed by other chemical reactions and dissolution in alkali medium (STEPANIK, EWING and WHITEHOUSE, 2000; KRAFT *et al.*, 2013; RÖDER *et al.*, 2013). Then, this liquid passes by a spinning process in acid bath and the cellulose fiber is formed again (STEPANIK, EWING and WHITEHOUSE, 2000). That is the reason for this material to be called as regenerated cellulose. Its properties can be controlled by changing, e.g., the pulp, the reagents content (as CS₂ and NaOH) or the spin speed (RÖDER *et al.*, 2013). After spinning, the production of viscose fabrics generates residues, which are discarded. These residues show the same chemical structural than the raw viscose and they were also selected to be studied here.

As discussed before, each source of cellulose may show different chemical composition as well as different properties. Among the possible distinctions, cellulose crystallinity may be one of the most important ones, because it influences the mechanical property of the fiber and of the nanocellulose extracted from it (KARGARZADEH *et al.*, 2017).

1.2 Cellulose crystallinity

Solid state of cellulose shows areas that are highly ordered (crystalline) and others that are disordered (amorphous), as indicated in Figure 3 (p. 4). This happens due to its macromolecular structure (KLEMM *et al.*, 2005; MOON *et al.*, 2011). Furthermore, cellulose can show polymorphism, *i.e.*, several crystalline organizations, according to its chemical treatment or source. The variable unit-cell usually can be distinguishable by the analysis of results of experimental techniques, such as X-Ray Diffraction (XRD), solid state nuclear magnetic resonance (NMR), infrared (IR) spectroscopy or electron diffraction (GARDNER and BLACKWELL, 1974; ISOGAI *et al.*, 1989; O’SULLIVAN, 1997; HABIBI, LUCIA and ROJAS, 2010; MOON *et al.*, 2011).

The bacterial cellulose basically shows majorly the allomorph known as $I\alpha$, just like algae cellulose. Its unit cell is triclinic, Figure 4 (VANDERHART and ATALLA, 1984; SUGIYAMA *et al.*, 1990; YAMAMOTO and HORII, 1993; YAMAMOTO and HORII, 1994; HABIBI, LUCIA and ROJAS, 2010; SAMIEE *et al.*, 2019).

On the other hand, the celluloses from tunicate and lignocellulosic fibers usually show the allomorph $I\beta$. Its unit cell is monoclinic and is less reactive than $I\alpha$ (KIMURA *et al.*, 2001; HABIBI, LUCIA and ROJAS, 2010; ZHANG *et al.*, 2017; BOGOLITSYN *et al.*, 2017). In $I\beta$, the segments of cellulose chains are in a parallel orientation and there are two intra-molecular hydrogen bonds per unit cell (KLEMM *et al.*, 2005).

The celluloses of allomorphs $I\alpha$ and $I\beta$ are different basically by the displacement of cellulose chains in one crystalline plane, in the chain axis direction (HABIBI, LUCIA and ROJAS, 2010; MOON *et al.*, 2011; DRIEMEIER and FRANCISCO, 2014), as shown in Figure 4.

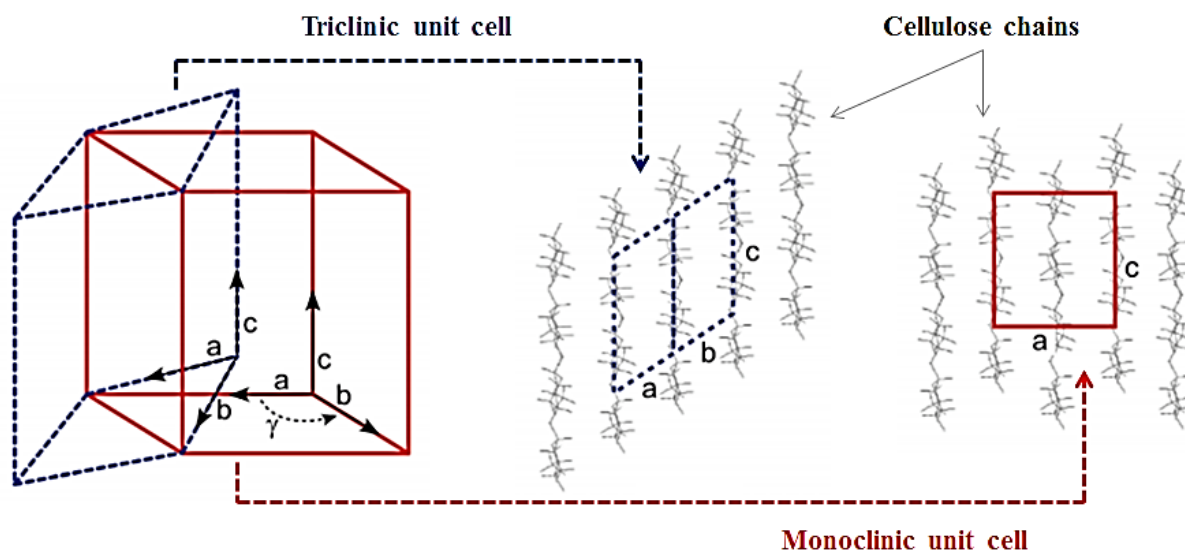


Figure 4 - Scheme of unit cells for cellulose I α (dashed line) and I β (solid line).
(Adapted from Moon *et al.*, 2011)

Thus, the hydrogen bonding in I α is distinct and is weaker than in I β . That is why I α is less stable and can thermally degrade at lower temperatures than I β (MOON *et al.*, 2011). It is also important to know that it is possible to convert cellulose I α to I β , by chemical treatments in high temperature (HABIBI, LUCIA and ROJAS, 2010; MOON *et al.*, 2011)

The literature shows that is possible the presence of both forms in plants, bacteria and algae (KLEMM *et al.*, 1998; BOGOLITSYN *et al.*, 2017). That is why native cellulose (or cellulose *in natura*) is commonly named only as cellulose I rather than only I α or I β (KLEMM *et al.*, 1998).

Meanwhile, the crystalline structure of regenerated celluloses, as viscose, usually is the allomorph II, which shows monoclinic unit cell. The segments of chains are antiparallel, and the unit cell dimensions are different from cellulose I in Figure 4 (KLEMM *et al.*, 1998; KLEMM *et al.*, 2005). This modification allows more hydrogen bonds than the allomorph I, leading to a more stable structure (KLEMM *et al.*, 2005; CIOLACU and POPA, 2006). The conversion mechanism of cellulose I to II is not yet understood (KLEMM *et al.*, 2005). However, it is known that cellulose II can also be obtained by the mercerization process of cellulose I in concentrated sodium hydroxide solutions (KLEMM *et al.*, 1998; HABIBI, LUCIA and ROJAS, 2010).

There are still more allomorphs of cellulose (III_i, III_{ii}, IV_i and IV_{ii}), obtained using chemical and thermal treatments (NISHINO, TAKANO and NAKAMAE, 1995; KLEMM *et al.*, 1998; KLEMM *et al.*, 2005; CIOLACU and POPA, 2006; HABIBI, LUCIA and ROJAS, 2010; KHALIL, BHAT and YUSRA, 2012).

The allomorph III is generated when cellulose I or II is treated with ammonia or other amines, and if the raw material is cellulose I or II, the results are cellulose III_i or cellulose III_{ii}, respectively (HABIBI, LUCIA and ROJAS, 2010). Cellulose III_i shows monoclinic unit cell, similar to cellulose I β , but the conformation of its hydroxymethyl groups is different, creating a hydrogen bond network comparable to cellulose II (HABIBI, LUCIA and ROJAS, 2010). The structure of allomorph III_{ii} is not clearly defined yet.

Finally, cellulose polymorphs IV_i and IV_{ii} are obtained heating (> 260 °C) cellulose III_i and III_{ii}, respectively, in glycerol (HABIBI, LUCIA and ROJAS, 2010).

It is important to keep in mind that the crystallinity of cellulose can influence its properties both in a micrometric fiber and in a nanomaterial isolated from it, also known as nanocellulose.

1.3 Nanocellulose

Cellulose in microscopic dimensions is largely used in the industry, but it can face drawbacks in some applications. For instance, fibers from lignocellulosic sources show low thermal stability (< 230 °C) due to hemicellulose and lignin content (PRADO and SPINACÉ, 2015). As a consequence, the possible thermoplastic matrices for composites are reduced, once the thermoplastic process temperature usually is higher than 230 °C (BLEDZKI and GASSAN, 1999). On the other hand, among the limitations of bacterial cellulose there are the lack of optical transparency of its membrane, and their dense network can hamper the infiltration of another polymer during the production of composites by extrusion, for example (ZABOROWSKA *et al.*, 2010; SHAH *et al.*, 2013).

One alternative for these drawbacks is isolating the nanostructures of cellulose. Their nomenclature is quite diverse (JACINTO and SPINACÉ, 2019). Cellulose nanofibers and cellulose nanocrystals are the most common ones, but there are other names, such as fibrils, nanofibrils, microfibrils, whiskers, nanorods, nanowires, etc. Their difference is basically related to their dimensions and their aspect ratio (DURÁN, LEMES and SEABRA, 2012). There are even standard procedures about the nomenclature of this nanomaterial, published by the International Organization for Standardization (ISO) and by Technical Association of the Pulp and Paper Industry (TAPPI): ISO/TS 20477:2017 and TAPPI WI 3021, respectively. Here, the term nanocellulose was chosen because it is the most generic one in the literature and embraces all possible morphologies (SEABRA *et al.*, 2018).

Nanocellulose show high surface area and can promote high interaction with the matrix (KHALIL *et al.*, 2016). Besides that, according to Zhao *et al.* (2015), they can be suspended in an aqueous solution, which improves its processability in the production of composites. The billionaire forest-products industry is also interested, looking for nanocellulose to improve paper properties and production (DURÁN, LEMES and SEABRA, 2012).

There are several methods to obtain these nanocelluloses, such as the chemical one, the enzymatic, by solvent fractionation or even the mechanical (ZHANG *et al.*, 2013; RAJINIPRIYA *et al.*, 2018).

The chemical route is the most common technique (HABIBI, LUCIA and ROJAS, 2010; DURÁN, LEMES and SEABRA, 2012; RAJINIPRIYA *et al.*, 2018; JACINTO and SPINACÉ, 2019). It is based on basic or acid hydrolysis (BRITO *et al.*, 2012; BETTAIEB *et al.*, 2015; MARIANO, CERCENÁ and SOLDI, 2016; LEITE *et al.*, 2017), but the acid one is the most important process (HABIBI, LUCIA and ROJAS, 2010). These studies often use sulfuric acid, at 40~60 °C, taking generally around 45 min, but there are process from 12 to 70 min (HABIBI, LUCIA and ROJAS, 2010; BRITO *et al.*, 2012; DURÁN, LEMES and SEABRA, 2012; BETTAIEB *et al.*, 2015; LEITE *et al.*, 2017; FERREIRA *et al.*, 2018; NADUPARAMBATH *et al.*, 2018). This approach happens because crystalline regions of cellulose are resistant to the acid attack while all the other regions and components are not, so they are hydrolyzed, allowing the production of isolated nanocellulose (HABIBI, LUCIA and ROJAS, 2010). Notwithstanding, there are some drawbacks in this method. Besides the energy consumption to maintain the high temperature during the hydrolysis, this hydrolysis inserts sulfate groups on nanocellulose chains decreasing its thermal stability and generates acid residues, Figure 5 (ROMAN and WINTER, 2004; KARGARZADEH *et al.*, 2012; PEREIRA *et al.*, 2014). Moreover, not only sulfuric acid but also other acids used to isolate nanocellulose (*e.g.*, phosphoric acid, hydrochloric acid and nitric acid) are toxic, corrosive and can lead to water pollution during the disposal of their process residues (LEE, HAMID and ZAIN, 2014). Two studies evaluated the environmental impact of nanocellulose from sugarcane bagasse using sulfuric acid and both of them concluded that the process should be optimized (ALBARELLI *et al.*, 2016; LEÃO *et al.*, 2017). For instance, Albarelli *et al.* (2016) determined that each kg of nanocellulose may require over 50 kg and almost 1300 L of sulfuric acid and water, respectively.

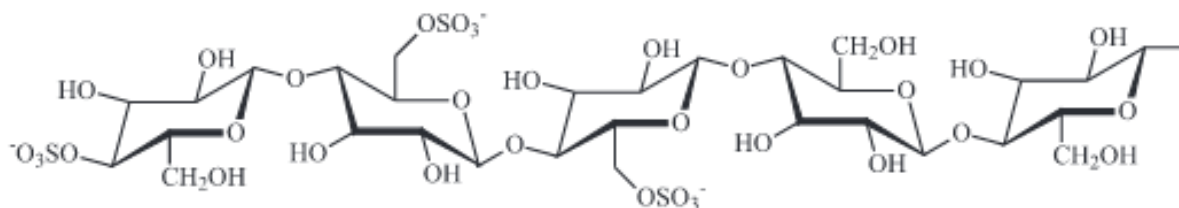


Figure 5 - Macromolecule of cellulose with grafted sulfate group due to hydrolysis with sulfuric acid. (PEREIRA *et al.*, 2014)

Considering the enzymatic method, instead of a chemical solvent, some enzymes are used to hydrolyze the fibers (KHALIL *et al.*, 2014; TIBOLLA *et al.*, 2017). They first promote the hydrolysis of the amorphous regions (as hemicellulose and lignin, in the case of lignocellulosic fibers) and then they may attack cellulose chains, producing nanocellulose (DURÁN, LEMES and SEABRA, 2012; SANTUCCI *et al.*, 2016; TIBOLLA *et al.*, 2017). Compared to conventional hydrolysis, enzymatic route doesn't have the problems with acid residues or lower thermal stability (SACUI *et al.*, 2014). However, sometimes it requires an alkaline pretreatment to eliminate lignin (from lignocellulosic fibers), the cellulose enzymes still are expensive, and the process takes too long, like 24 h (TIBOLLA *et al.*, 2017; TRACHE *et al.*, 2017; SAMIEE *et al.*, 2019).

Besides the enzymes, the solvent fractionation, such as by ionic liquids, is another possibility to the environmental problems of acid hydrolysis (ZHANG *et al.*, 2013). These ionic liquids are organic salts with melting point below 100 °C at 1 atm (MAN *et al.*, 2011; CASAS *et al.*, 2012). They show the ability to break hydrogen bonds of cellulose and dissolve it. Based on that, the raw cellulosic material is mixed with an ionic liquid in order to solubilize the cellulose. Later, it is possible to isolate the nanocellulose that is dissolved in the medium (CASAS *et al.*, 2012; TRACHE *et al.*, 2017). Even though this liquid can be reused (TRACHE *et al.*, 2017), the process can also lead to insertion of ionic groups in cellulose chains, decreasing its thermal stability (MAN *et al.*, 2011). Aside from that, according to Zhang *et al.* (2013), their high cost and toxicity limit their applications. For instance, effluents of this process can pollute water and they are dangerous for human health as well (ZHAO, LIAO & ZHANG, 2007).

A different approach is to use the mechanical techniques. They usually don't need any solvent besides water neither change the surface chemistry of nanocellulose (ZHANG *et al.*, 2013; SACUI *et al.*, 2014; TRACHE *et al.*, 2017). The aqueous medium is applied in order to loosen the interfibrillar hydrogen bonding, what can benefit the extraction of nanocellulose (NECHYPORCHUK, BELGACEM & BRAS, 2016). Among the possible methods there are,

e.g.: high pressure homogenization, grinding, ball milling, cryocrushing and high intensity ultrasonication (HIUS) (MOON *et al.*, 2011; DURÁN, LEMES and SEABRA, 2012; 2010; KHALIL *et al.*, 2014; TRACHE *et al.*, 2017; RAJINIPRIYA *et al.*, 2018). Usually they generate a high shearing force that causes the extraction of cellulose followed by its nanocrystals (WANG and CHENG, 2009; MOON *et al.*, 2011). Meanwhile, generally they are energy consuming and can lead to damages to nanocellulose crystalline structure (MOON *et al.*, 2011; KHALIL *et al.*, 2012; ZHANG *et al.*, 2013; TRACHE *et al.*, 2017).

On the other hand, HIUS can be applied in large scale and may allow a high crystallinity of nanocellulose (ZHAO, FENG and GAO, 2007; LEONELLI and MASON, 2010; AMIN *et al.*, 2015; SOYEKWO *et al.*, 2016).

1.3.1 High intensity ultrasonication (HIUS)

The usage of this approach in medicine led to its popularization in life and society, including in materials science (CINTAS and LUCHE, 1999). Among its applications, HIUS aims to extract micron sized fibers in water down to nano sized structures (ZHAO, FENG and GAO, 2007; PINJARI and PANDIT, 2010).

In this process, there is a piezoelectric material in a bath, in a plate system or in a horn as shown in Figure 6 (BUSSEMAKER and ZHANG, 2013). It receives an electric signal and produces a mechanical vibration in ultrasound frequency (BUSSEMAKER and ZHANG, 2013). These waves of 10 kHz until 10 MHz generate cavitation in the liquid and secondary processes, such as chemical decomposition of compounds (SUSLICK, 1990; WANG and CHENG, 2009; SUTKAR, GOGATE and CSÓKA, 2010; LUO, FANG and SMITH JR, 2014).

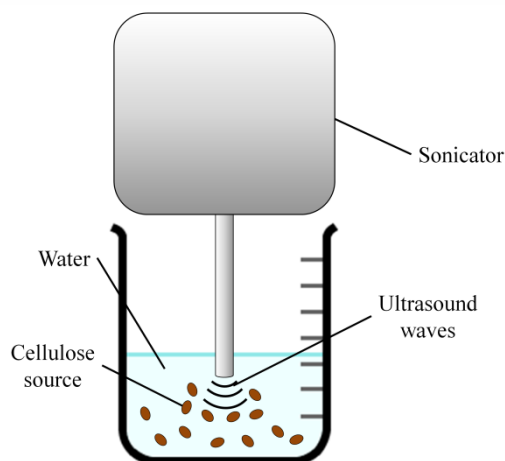


Figure 6 - Scheme of HIUS system to extract nanocellulose.

Cavitation happens because ultrasound waves are able to break the intermolecular forces of the liquid, leading to the formation of microbubbles (CINTAS and LUCHE, 1999; BUSSEMAKER and ZHANG, 2013). These microbubbles start to grow preferably close to heterogeneities, such as other bubbles or solid impurities (SUSLICK, 1990; CINTAS and LUCHE, 1999). They keep growing and when they reach a resonant size, their growth speed increases and absorb more and more energy (SUSLICK, 1990). Then, they destabilize and implode, creating liquid jets of high speed (greater than 100 m/s) and high pressures (more than 500 atm) or shock waves through the liquid (SUSLICK, 1990; CINTAS and LUCHE, 1999; WANG and CHENG, 2009; PINJARI and PANDIT, 2010; BUSSEMAKER and ZHANG, 2013; AMIN *et al.*, 2015). The cavitation ends, but the jets can hit the surface of a solid sample in the liquid, even leading to particle breakage (CINTAS and LUCHE, 1999), and the shock waves can cause attrition of the solid particles present (PINJARI and PANDIT, 2010).

Beyond the mechanical effects, there are the chemical ones too (LI, YUE and LIU, 2012). For instance, if water is the liquid during sonication, so the bubble collapses can produce radicals, such as $H\bullet$ and $OH\bullet$ (CINTAS and LUCHE, 1999; BUSSEMAKER and ZHANG, 2013). They may react with other substances to induce oxidation reactions, for example (CINTAS and LUCHE, 1999).

If the solid sample inside the liquid is a cellulose source (lignocellulosic, regenerated, bacterial or any other), this process can be used to extract nanocellulose (ZHAO, FENG and GAO, 2007; CHENG, WANG and HAN, 2010; CHEN *et al.*, 2011; LI, YUE and LIU, 2012; RAJINIPRIYA *et al.*, 2018). The jets created by cavitation lead to separation or fibrillation of the fibers of cellulose, bonded to each other by intermolecular forces (ZHAO, FENG and

GAO, 2007; CHENG, WANG and RIALS, 2009; WANG, LI and ZHANG, 2013; AMIN *et al.*, 2015; SANTUCCI *et al.*, 2016; NACAS *et al.*, 2017). Their impact on cellulose surface can cause erosion along the axial direction, disintegrating the micron-sized fibers into nanostructures (ZHAO, FENG and GAO, 2007; CHEN *et al.*, 2011; LI, YUE and LIU, 2012). This nanocellulose shows a wide distribution in width and may aggregate, due to the formation of hydrogen bonds (CHEN *et al.*, 2011; LI, YUE and LIU, 2012).

However, if the source is lignocellulosic, there are other components in the medium besides cellulose, i.e., hemicellulose and lignin, which may also be degraded by HIUS (BUSSEMAKER and ZHANG, 2013). The hydroxyl groups on hemicellulose are susceptible to oxidation by the oxidizing radicals produced by HIUS. It is possible to have dehydration and cleavage of hemicellulose chains (BUSSEMAKER and ZHANG, 2013). On the other hand, the ether, phenolic and aliphatic hydroxyl groups, for example, are the reactive sites in lignin (BUSSEMAKER and ZHANG, 2013). However, lignin degradation depends on the chemical environment during HIUS. Usually, there is depolymerization, possibly by hydroxyl attack on aromatic rings or side chains (BUSSEMAKER and ZHANG, 2013). But some solvents (such as phenol and potassium hydroxide solutions) may favor the accumulation of species at the bubble interface during cavitation that may promote repolymerization of lignin, increasing its molar mass (BUSSEMAKER and ZHANG, 2013). Moreover, HIUS can favor the cleavage of bonds between lignin and hemicellulose (BUSSEMAKER and ZHANG, 2013). Nevertheless, all these chemical effects by HIUS are more common in high frequencies than in low frequencies, as 20 kHz (BUSSEMAKER and ZHANG, 2013).

There are many other factors affecting cavitation and nanocellulose extraction during HIUS, such as:

- a) cellulose source (ZHAO, FENG and GAO, 2007; CAMPOS *et al.*, 2013; BUSSEMAKER and ZHANG, 2013; SOYEKWO *et al.*, 2016);
- b) mass of raw fiber (WANG and CHENG, 2009; CHENG, WANG and HAN, 2010);
- c) time of sonication (CHENG, WANG and HAN, 2010; LI, YUE and LIU, 2012; KETABCHI *et al.*, 2016; SANTOS *et al.*, 2016; MAHARDIKA *et al.*, 2018; CHOWDHURY *et al.*, 2019; WARDHONO, KANANI and ALFIRANO, 2019);
- d) solvent where the cellulose source is during HIUS (CINTAS and LUCHE, 1999; WARDHONO, KANANI and ALFIRANO, 2019);
- e) height of the solvent in the beaker (BUSSEMAKER and ZHANG, 2013);
- f) temperature during the process (CHENG, WANG and HAN, 2010; SANTOS *et al.*, 2016; CHOWDHURY *et al.*, 2019);

- g) intensity of equipment power (ZHAO, FENG and GAO, 2007; WANG and CHENG, 2009; CHENG, WANG and HAN, 2010; CHOWDHURY *et al.*, 2019; HUERTA and SALDAÑA, 2019);
- h) distance between the HIUS tip and the beaker bottom (WANG and CHENG, 2009; CHENG, WANG and HAN, 2010).

Because of that, some parameters were studied here, like source of cellulose, time and mass loading (as described in Section 3.2, p. 20), while the others were constant. All these parameters are important for large scale production, what is interesting especially for nanocellulose suppliers.

1.3.2 Nanocellulose suppliers

According to Klemm *et al.* (2018), nanocellulose is available mainly for research and development projects. The suppliers of this nanomaterial are mainly in Canada (CelluForce, Kruger, and Cellulose Lab), in United States (University of Maine), in Japan (Nippon Paper and Oji Paper), and in Norway (Borregaard).

CelluForce is focused on the production of cellulose nanocrystals from wood using acid hydrolysis (CELLUFORCE, 2019). The Brazilian company Suzano is among the stakeholders of CelluForce and it started studies to produce nanocellulose from Eucalyptus in a pilot plan at Limeira (SP) using high pressure homogenization, but its product is not yet commercially available.

Other companies, such as Kruger, University of Maine, Nippon Paper, Oji Paper and Borregaard supply only cellulose nanofiber from wood (EXILVA, 2019; KRUGER, 2019; NIPPON PAPER, 2019; OJI PAPER, 2019; UNIVERSITY OF MAINE, 2019).

The portfolio of Cellulose Lab is wider than the other ones, showing different sources of cellulose as wood, bacterial cellulose and tunicate, besides distinct morphologies: cellulose nanocrystals and cellulose nanofibers (CELLULOSE LAB, 2019).

The biggest challenge to popularize nanocellulose is its price. Commercial grades of cellulose fibers in microscale in São Paulo State cost ~0,7 U\$/kg (2,8 R\$/kg) and the average Brazilian export price of this material is around 0,4~0,6 U\$/kg (1,6~2,4 R\$/kg) (CEPEA 2019). Research grade of cellulose in microscale can be easily purchased online by 10 U\$/kg (~40 R\$/kg) (SYNTH, 2019). However, the market of nanocellulose is totally different. Products of CelluForce cost between 50 and 7,500 U\$/kg (~200 until 30,000 R\$/kg) while Cellulose Lab prices ranges from 1,750 until 55,000 U\$/kg (~7,000 until 220,000 R\$/kg),

and University of Maine charges from 110 until 1,520 U\$/kg (~450 until 6,200 R\$/kg). All these values did not considered costs with shipping and import taxes. Price changes according to morphology, to physical aspect (powder or aqueous suspension) and to chemical modifications on the nanocellulose surface.

Notwithstanding, the increasing demand of nanocellulose applications leads to large productions, which could drop the price below ~15 U\$/kg (~60 R\$/kg) (KLEMM *et al.*, 2018). In this manner, the production of nanocellulose must keep in mind its possible applications in order to facilitate the future availability of this nanomaterial.

1.3.3 Nanocellulose applications

Nanocellulose can be applied in the food sector, as a dessert (usually known as “nata” from bacterial cellulose), as stabilizer of oil-in-water emulsions, such as sauces and soups, or as rheological modifier, *e.g.*, in ice creams or tofu (SHI *et al.*, 2014; SERPA *et al.*, 2016; AZEREDO, 2018; KLEMM *et al.*, 2018).

Furthermore, the biomedical field shows many opportunities. It can be applied as scaffolds for tissue engineering or as membranes for wound dressings (THOMAS *et al.*, 2018). These membranes are already commercially available in Brazil, supplied, for example, by Vuelo Pharma. There are also studies about nanocellulose as drug carriers in drug delivery systems. Seabra *et al.* (2018) as well as Löbmann and Svagan (2017) recently published reviews highlighting the advantages of cellulose nanocrystals and cellulose nanofibers in drug delivery, respectively.

Besides all that, the main application is as reinforcement in nanocomposites. Trache *et al.* (2017) stated that 75% of the world literature about nanocellulose considers this approach, and the same trend was observed in Brazil, with 64% of papers (JACINTO and SPINACÉ, 2019). Usually, its content in the composition of the nanocomposite is low ($\leq 5\%$ wt), but it ensures increasing the mechanical, thermal or barrier properties better than cellulose in the micro scale (SIRÓ and PLACKETT, 2010). This enhancement happens based on the strong interactions among the own nanocellulose particles, which can lead to a particular aggregation among them, forming a continuous network through the nanocomposite. The elastic modulus of this network is higher than one of an individual particle of nanocellulose (MARIANO, EL KISSI and DUFRESNE, 2014).

It is possible to associate nanocellulose with different polymer matrices, which can be hydrophilic or hydrophobic, biodegradable or not (SIRÓ and PLACKETT, 2010). For

instance, it is reported that nanocellulose can improve the properties of polyethylene (CASTRO *et al.*, 2015), polyvinyl alcohol (LAM *et al.*, 2017), starch (EL MIRI *et al.*, 2015; RANI *et al.*, 2018), polyurethane (AUAD *et al.*, 2008; HARAGUCHI *et al.*, 2013), etc. However, it should be mentioned that some matrices (especially those hydrophobic) may require a compatibilizer that can be grafted in nanocellulose surface or added to the formulation of the nanocomposite (KARGARZADEH *et al.*, 2017).

In this context, the crystallinity of the nanocellulose is highlighted as the property with the highest impact in its mechanical reinforcement capacity due to its relation with the Young modulus of the nanomaterial (MARIANO, EL KISSI and DUFRESNE, 2014; KARGARZADEH *et al.*, 2017). Therefore, it is interesting that the method for extraction of nanocellulose maintains or increases the crystallinity index in relation to the raw material. Another property that is relevant to nanocomposites is the aspect ratio of nanocellulose, i.e., the ratio between the length and the diameter of the cellulosic nanomaterial. Kargarzadeh *et al.* (2017) verified that higher aspect ratio of nanocellulose can result in a better reinforcement of nanocomposites (KARGARZADEH *et al.*, 2017).

1.4 Motivation

As discussed before, cellulose is a great alternative to materials of non-renewable sources in order to reinforce composites. Brazilian resources and research of microscale cellulose are recognized worldwide (GUIMARÃES *et al.*, 2009; RAMAMOORTHY, SKRIFVARS and PERSSON, 2015). However, nanocellulose can show even more advantages, such as the higher specific surface area, which is interesting for nanocomposite applications.

Recently, many studies have been published about the extraction of nanocellulose and this number is increasing yearly (MILANEZ *et al.*, 2013; GARCÍA *et al.*, 2016; JACINTO and SPINACÉ, 2019). Brazil is among the most important countries worldwide in this scenario and Figure 7 shows the most common techniques to isolate nanocellulose reported in Brazilian publications (JACINTO and SPINACÉ, 2019).

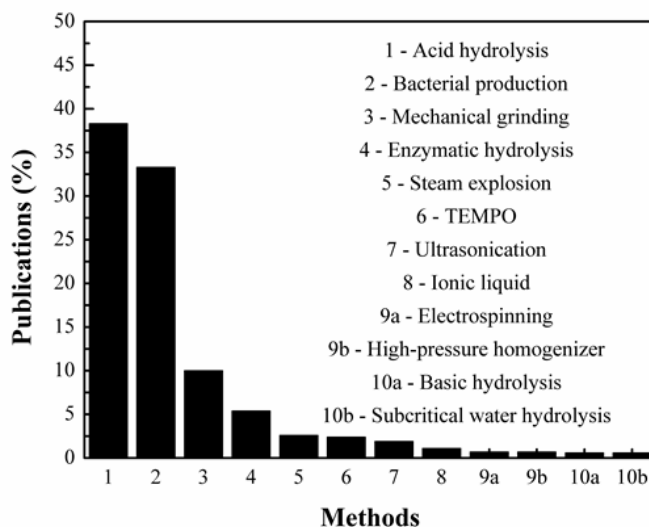


Figure 7 - Most used methods to extract nanocellulose published in Brazilian papers available in the Web of Science database.
(JACINTO and SPINACÉ, 2019)

In Figure 7 it is possible to verify that HIUS is already among the most common methods in Brazil. However, most papers using HIUS, from Brazil or not, usually considered only two approaches. In the first one, authors sonicated pure or pretreated celluloses, in order words, fibers without hemicellulose and/or lignin (for example: WONG, KASAPIS and TAN, 2009; AMIN *et al.*, 2015; YANG *et al.*, 2017). The second alternative combined HIUS with other methods, such as enzymatic or other mechanical ones (such as: TONOLI *et al.*, 2012; DURÁN, LEMES and SEABRA, 2012; SANTUCCI *et al.*, 2016; ABRAL *et al.*, 2018).

Moreover, there are few suppliers of nanocellulose worldwide, none of them are in Brazil, as discussed in Section 1.3.2. Therefore, researches about this topic can help to develop the Brazilian industry.

To the best of my knowledge, there is nothing in the literature comparing the HIUS effect on different types of cellulose with different sonication conditions and without previous chemical treatment. It is interesting to avoid additional pretreatment steps in the process to reduce costs and its environmental impact (SANTUCCI *et al.*, 2016).

In this manner, I present here a comparison among:

- a) bacterial cellulose, which is a pure cellulose, with crystalline allomorph I;
- b) viscose, which is also pure cellulose, but with allomorph II;
- c) two lignocellulosic sources: curaua and sugarcane bagasse, which have distinct content of cellulose, hemicellulose and lignin in their structures.

2 OBJECTIVES

2.1 General objective

This Dissertation aimed to study the conditions to obtain nanocellulose of curaua, sugarcane bagasse, viscose residue and bacterial cellulose without chemical pretreatment and using only HIUS.

2.2 Specific objectives

To evaluate HIUS influence on the crystallinity of nanocellulose, using 2^k planning.

To characterize nanocellulose using techniques of XRD (X-Ray Diffraction), FTIR (Fourier Transform Infrared), TGA (Thermogravimetric Analysis), DLS (Dynamic Light Scattering) and AFM (Atomic Force Microscopy).

To identify the best condition to produce nanocellulose that may be applicable as reinforcement in polymeric nanocomposites.

3 EXPERIMENTAL

3.1 Materials

Residues of dry membranes of bacterial cellulose (Figure 8) used to healthcare applications were kindly supplied by Vuelo Pharma (Curitiba, Brazil). Residues of weaving process of viscose fibers were supplied by local industries (Itupeva, Brazil). Sugarcane bagasse (*Costus spiralis Roscoe*) was supplied by local markets (São Paulo, Brazil) and was immersed in deionized water at 23 °C, washed in running water, then dried in oven (8 h, 100 °C) (MI1512, Nova Instruments) to remove soluble sugars and impurities. Curaua fibers (*Ananus erectifilius*) were kindly supplied, already washed, dried and milled, by the Brazilian Agricultural Research Corporation (Embrapa) Eastern Amazon Unit (Belém, Brazil). All raw materials are shown as received in Figure 8. At last, the solvent utilized during sonication was deionized water.

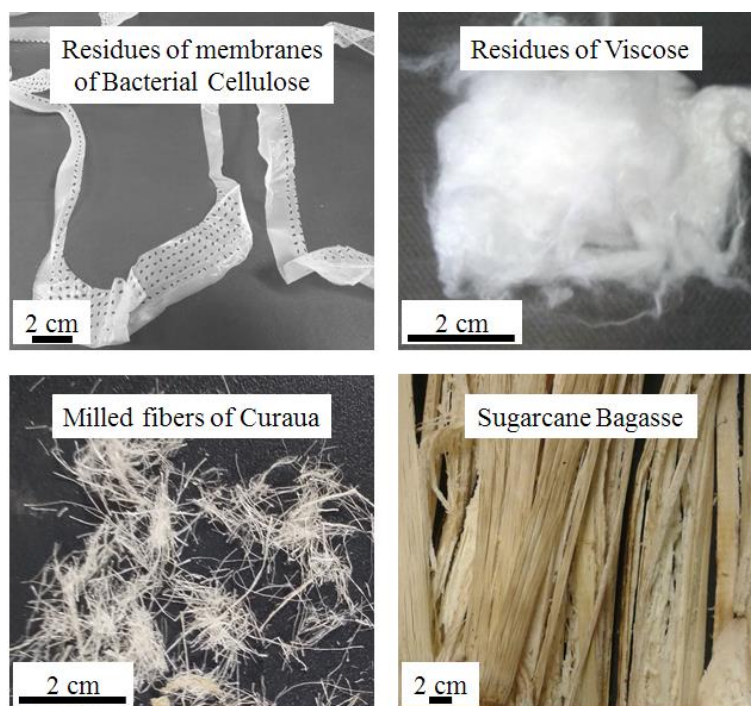


Figure 8 - Cellulose sources as received: bacterial cellulose, residues of viscose, curaua and sugarcane bagasse.

All samples were ground in a knife mill (Marconi, M048) and sifted (Contenco) in sieves of 28 mesh (0.59 mm) (bacterial cellulose) and 100 mesh (0.15 mm) (viscose residue named as VR_{raw}, sugarcane bagasse and curaua). Bacterial cellulose (BC_{raw}) was sieved differently

because the yielding using knife mill to 100 mesh was too low. Table 1 summarizes the abbreviations of all raw materials used in this Dissertation.

Table 1 - Abbreviation of raw cellulosic materials sonicated by HIUS process.	
Material	Abbreviation
Raw bacterial cellulose	BC _{raw}
Raw curaua	C _{raw}
Raw sugarcane bagasse	SCB _{raw}
Raw viscose residue	VR _{raw}

3.2 HIUS process

Before sonication, sugarcane bagasse and curaua were immersed in hot deionized water (3 g of fiber / 300 mL of deionized water), at 75 °C for 4 h to remove soluble components, then vacuum filtered and dried in oven (4 h, 100 °C) (MI1512, Nova Instruments).

All samples (BC_{raw}, VR_{raw}, SCB_{raw} and C_{raw}) were sonicated with high intensity ultrasound (CPX750 – 750 W, Cole Parmer), using a probe of 13 mm and deionized water as solvent. The system was immersed in ice bath to control temperature, Figure 9. The temperature during sonication ranged from 19 until 25 °C. The distance between the HIUS tip and the beaker bottom was 15 mm. This parameter affects the path length of the ultrasonic wave, influencing the HIUS efficiency (WANG and CHENG, 2009).

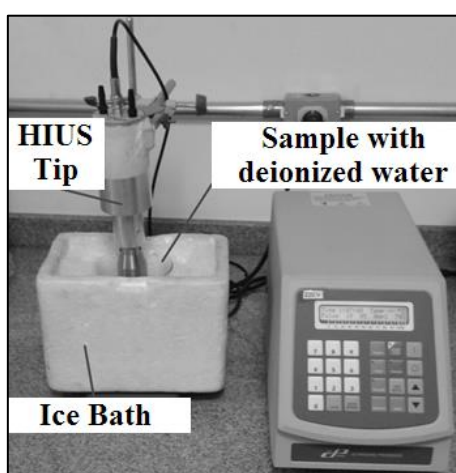


Figure 9 - Image HIUS system used for sonication of BC_{raw}, VR_{raw}, SCB_{raw} and C_{raw} samples.

The HIUS conditions, following 2^k planning (BARROS NETO, SCARMINIO and BRUNS, 1995; HENDERSON-SELLERS and HENDERSON-SELLERS, 1996; ZHOU *et al.*, 1995; BRUNS, BARROS NETO and SCARMINIO, 2006), are described in the Table 2.

Table 2 - HIUS conditions.

Condition	Time (min)	Mass (g)
X1	45	0.1
X2	70	0.1
X3	45	0.2
X4	70	0.2

These conditions are based on previous studies in the research group of Prof. Spinacé (JACINTO, 2016; NACAS *et al.*, 2017). The volume of deionized water used in all conditions was 150 mL. The power of HIUS was 70 %, which was the maximum possible for this equipment. This value is important because as the power increases, the efficiency of HIUS to extract nanostructures from micrometric cellulose also enhances (WANG and CHENG, 2009; BUSSEMAKER and ZHANG, 2013). After sonication, all samples were maintained at 5 °C for 24 h. Then they were centrifuged at 8,000 rpm for 7 min (NI1803, Nova Instruments) and the obtained nanocelluloses were characterized.

In the Table 2, the symbol X represents the samples from different sources (C for curaua, SCB for sugarcane bagasse, VR for viscose residue and BC for bacterial cellulose). The total times which are indicated in Table 2 include the sum of sonication time (10 s/pulse) and rest time of equipment (5 s/pulse). Consequently, the times of 45 and 70 min correspond respectively to 30 and ~ 47 min of pure sonication.

The effects of two factors were studied: mass (m) and sonication time (t) among all samples (X₁ to X₄). The 2² factorial planning was used, on two levels (BRUNS, BARROS NETO and SCARMINIO, 2006), naming m₁ to 0.1 g, m₂ to 0.2 g, t₁ to 45 min and t₂ to 70 min. Main effects on crystallinity index (CI) were calculated according to Eq. 1 and 2.

$$t = \frac{[(t_2 m_1 - t_1 m_1) + (t_2 m_2 - t_1 m_2)]}{2} \quad (1)$$

$$m = \frac{[(t_1 m_2 - t_1 m_1) + (t_2 m_2 - t_2 m_1)]}{2} \quad (2)$$

The symbol t_im_i represents the CI of a sample sonicated with mass m_i (g) for time t_i (min). The interaction effect (tm) was calculated according to Eq. 3.

$$tm = \frac{[(t_2m_2 - t_2m_1) - (t_1m_2 - t_1m_1)]}{2} \quad (3)$$

The experimental variance is the arithmetic average of the observed variance in each individual test because the number of repetitions is the same for all samples (BARROS NETO, SCARMINIO and BRUNS, 1995; BRUNS, BARROS NETO and SCARMINIO, 2006). So, the standard error to each sample was estimated according to Eq. 4.

$$standard\ error = \sqrt{\frac{experimental\ variance}{number\ of\ repetitions}} \quad (4)$$

If the standard error is higher than an effect, so this effect is not significant and should be inconsiderate (BARROS NETO, SCARMINIO and BRUNS, 1995; BRUNS, BARROS NETO and SCARMINIO, 2006).

Moreover, Eq. 5 allowed determining the energy consumption for extraction of nanocellulose. This equation was based on the methods reported for calculation of energy consumption of nanocellulose production (ERIKSEN, SYVERUD and GREGERSEN, 2008; FRONE *et al.*, 2011; NECHYPORCHUK, BELGACEM & BRAS, 2016; LU *et al.*, 2018; EWULONU *et al.*, 2019).

$$energy\ consumption\ (\frac{MWh}{ton}) = \sum \left(\frac{Power\ consumption}{(yielding)(mass\ of\ raw\ material)} \right) \quad (5)$$

In Eq. 5 it is necessary to sum the energy consumption due to each equipment used in the process, as the ice machine (20 W), the hot bath (1000 W) and HIUS (525 W). The yielding was determined first measuring the mass of particles with 0,5 µm or more after sonication (separated by filtration). Then, it was subtracted of the total mass before sonication. The yielding was the ratio between the mass of particles smaller than 0,5 µm and the total mass before sonication.

Figure 10 summarizes the sequence of steps followed in this research.

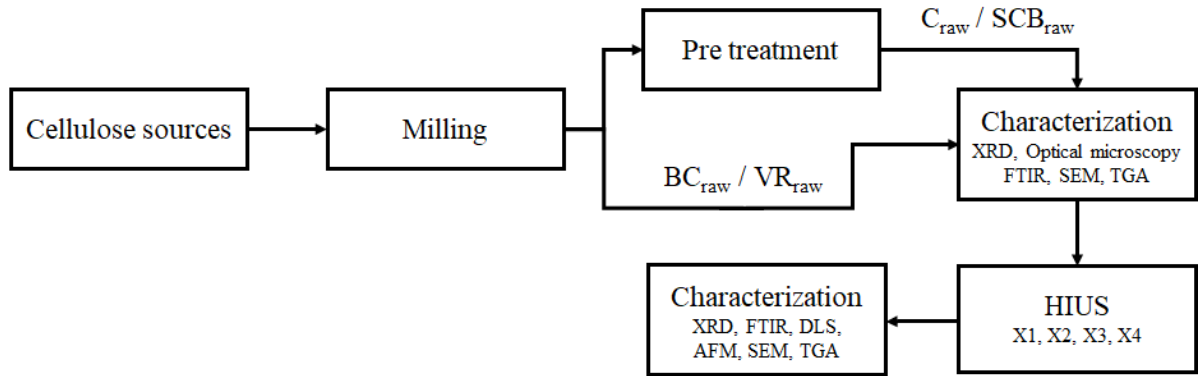


Figure 10 - Sequence of steps followed in this Dissertation.

After all characterizations, the 2^k planning analysis of crystallinity index (CI) allowed to determine the best condition among them all, which could enable a better reinforcement in a nanocomposite with a polymeric matrix. This sample was chosen to evaluate a different HIUS condition to reduce the energy consumption of the process. For this purpose, there was an increment in mass loading to 2 g of the chosen raw cellulosic material. This new sample was characterized as well.

3.3 Characterization

3.3.1 Crystallinity

Diffraction patterns of samples before and after HIUS were measured in duplicate on X-Ray diffractometer (Miniflex II, Rigaku), with $\text{CuK}\alpha$ radiation ($\lambda = 0.1541 \text{ nm}$), at 40 mA and 40 kV, with 2Θ varying from 5 to 70 ° (2 °/min), with subtraction of equipment background. This subtraction was carried out in order to confirm that the amorphous contribution in the diffractograms was related exclusively to the presence of amorphous regions in the analyzed sample. The equipment of X-Ray Diffraction (XRD) is at the Multiuser Central Facilities, at Federal University of ABC (Santo André, Brazil).

The crystallinity index (CI) was determined by Eq. 6, through deconvolution method (OH *et al.*, 2005; CORRÊA *et al.*, 2014; OLIVEIRA *et al.*, 2015; ARAÚJO JR *et al.*, 2016), using Origin® software, considering Pseudo-Voigt 2 shaped peaks. The original diffraction pattern was deconvoluted separating the characteristic crystalline peaks of the sample and its amorphous region. Where A_a is the area of amorphous halo and A_T is the total area, including the crystalline peaks.

$$CI (\%) = 100 \left(1 - \frac{A_a}{A_T} \right) \quad (6)$$

For viscose samples, FT-Raman spectroscopy was carried out (MultiRaAM, Bruker), from 1600 to 200 cm^{-1} , with 32 scans, using 350 mW. The FT-Raman instrument is at the Multiuser Central Facilities, at Federal University of ABC (Santo André, Brazil). The region between 1600~200 cm^{-1} is the most sensitive to polymorphic changes (ATALLA, 1975).

3.3.2 Size distribution and morphology

The size distribution of raw materials (BC_{raw} , SCB_{raw} and C_{raw} and VR_{raw}) before HIUS was analyzed using optical microscopy (Scope A.1, Zeiss). The equipment is at the Materials Engineering Laboratory, at Federal University of ABC (Santo André, Brazil). ImageJ® software was used to measure the diameter (D) and the length (L) of more than 200 particles for each material. Weighted average (\bar{X}) was calculated according to Eq. 7.

$$\bar{X} = \frac{\sum_{i=0}^n n_i (X_i)^2}{\sum_{i=0}^n n_i X_i} \quad (7)$$

In Eq. 7, \bar{X} represents weighted average diameter (\bar{D}) or length (\bar{L}) and n_i is the number of occurrences of each dimension X_i . With these results, it was possible to calculate the aspect ratio (L/D), following Eq. 8.

$$L/D = \frac{\bar{L}}{\bar{D}} \quad (8)$$

This value is important because the particle size can influence the efficiency of nanocellulose extraction using HIUS (KOUTSIANITIS *et al.*, 2015).

The morphology of samples before and after HIUS was characterized by Scanning Electron Microscopy (SEM) (JSM-6010LA, JEOL), after coating with 10 nm of gold (EM ACE600, Leica). The SEM and sputtering instrument are at the Multiuser Central Facilities, at Federal University of ABC (Santo André and São Bernardo do Campo, Brazil), respectively.

Because of limited resolution of conventional SEM, Dynamic Light Scattering (DLS, LSE-5004, ALV) was carried out to confirm the presence of nanocellulose extracted by HIUS

and also to estimate their size distribution. DLS was made at 25 °C, with a detection angle of 90 °, 20 s/scan, 3 scan/sample. The equipment is at the Laboratory for Crystallography and Structural Characterization of Materials, at Federal University of ABC (Santo André, Brazil). Each sample was 1 mL of suspension of nanocellulose with deionized water, obtained after 24 h of sonication.

The morphology of nanocelluloses extracted from bacterial cellulose was determined using atomic force microscopy (AFM - 5500 AFM, Agilent) in contact mode, with a tip (CCSR-10, ASPIRE) with a resonant frequency of 28 kHz and a force constant of 0.1 N/m. The equipment is at the Multiuser Central Facilities, at Federal University of ABC (Santo André, Brazil). Droplets of 20 µL of suspensions with nanocellulose were placed onto a silica substrate and dried at 25 °C, before AFM experiment. The data were analyzed with Gwyddion[®] software. On the other hand, nanocellulose from curaua, sugarcane bagasse and viscose residue were characterized by transmission electron microscopy (TEM – TALOS F200C, Thermo Fischer Scientific), with images acquired by a camera of 4000 x 4000 pixels (CMOS Ceta 16M, Thermo Fischer Scientific). Droplets of nanocellulose suspension were dropped onto copper grids with ultrathin carbon (Lacey Carbon Type A 400 mesh, TedPella) and negatively stained with uranyl acetate (aqueous solution, 2 %wt, during 30 s). Before contact with nanocellulose samples, the copper grids were submitted to glow discharge (easiGlow, Pelco) using 15 mA, negative charge, during 25 s. The equipment is at the Electron Microscopy Laboratory, at Brazilian Nanotechnology National Laboratory (LNNano - Campinas, Brazil). ImageJ[®] software was used to measure the diameter and the length of more than 50 particles for each sample analyzed by AFM and TEM. Weighted averages of diameter and length were calculated using Eq. 7.

3.3.3 Chemical composition

The quantification of lignin and ash for SCB_{raw} and C_{raw} was performed in solid samples (GOUVEIA *et al.*, 2009; REZENDE *et al.*, 2011; NASCIMENTO and REZENDE, 2018). All the component contents are expressed on a dry fiber basis.

Each sample (2 g) was treated with 10 mL of a H₂SO₄ solution (72 % v/v), at 45 °C, under vigorous stirring, for 7 min. Deionized water was added until reaching a 275 mL final volume. Then, the materials were kept at 120 °C, 1 atm, for 30 min (CS vertical autoclave, Primatec). After cooling to room temperature, they were vacuum filtered using qualitative paper, until the solid fraction reached a neutral pH.

These solid fractions were dried in oven at 100 °C (MI1512, Nova Instruments) to a constant mass, which means the sum of insoluble lignin and ash. These solids were calcinated inside porcelain crucibles in a muffle furnace (2 h, 800 °C). Ash mass was determined after cooling to room temperature. With these results it was possible to calculate the insoluble lignin amount.

In order to study the chemical composition of each sample before and after HIUS, Fourier-Transform Infrared (FTIR) measures were performed (Frontier 100 FT-IR, Perkin-Elmer) in duplicate, using attenuated total reflectance (ATR) mode, from 4000 to 650 cm^{-1} , with 32 scans and resolution of 4 cm^{-1} . The FTIR instrument is at the Laboratory for Spectroscopy, Electronics and Optics, at Federal University of ABC (Santo André, Brazil). Before FTIR test, each sample was dried in oven for 2 h, at 100 °C (MI1512, Nova Instruments) with a mass around 5 mg.

The relative quantification of different chemical groups attributed to hemicellulose and lignin in curaua and sugarcane bagasse samples (before and after HIUS) was determined. The peak heights were measured and normalized using cellulose peak at $\sim 897 \text{ cm}^{-1}$, due to C-H deformation of glucose ring (ÅKERHOLM, HINTERSTOISSER and SALMÉN, 2004; ROSA *et al.*, 2010). This peak is presented in all cellulosic samples and do not change with decreasing of its crystallinity (HULLEMAN, VAN HAZENDONK and VAN DAM, 1994). The relative intensity was named as $I_{X/897}$, where “X” is the wavenumber of interest.

It was used also AFM coupled with infrared spectroscopy, known as AFMIR, (nanoIR2-S, Anasys Instruments) in contact mode, with a gold coated tip (ContGB, Budget Sensor), with a resonant frequency of 13 kHz and a force constant of 0.2 N/m. The equipment is at the Laboratory for Surface Science, at Brazilian Nanotechnology National Laboratory (LNNano - Campinas, Brazil). For AFMIR, the droplets were placed on a gold coated silicon substrate and dried at 25 °C. The data were analyzed with Gwyddion® software.

3.3.4 Thermal properties

The thermal stability of all samples, before and after HIUS, was determined using a thermogravimetric analyzer (Q500, TA Instruments), from 30 to 600 °C, at a heating rate of 10 °C/min, under nitrogen atmosphere. The equipment of thermogravimetric analysis (TGA) is at the Multiuser Central Facilities, at Federal University of ABC (Santo André, Brazil). Each sample mass was around 10 mg.

4 RESULTS AND DISCUSSION

4.1 Chemical structure of cellulose before and after sonication process

4.1.1 Chemical structure of bacterial cellulose

FTIR was carried out in order to evaluate the chemical composition of all samples before and after HIUS process. Figure 11 shows FTIR curves. Just to remind the reader, BC1 was sonicated during 45 min with 0.1 g of BC_{raw}, BC2 used 0.1 g during 70 min, BC3 used 0.2 g during 45 min while BC4 used 0.2 g during 70 min, as presented in Table 2 (p. 21).

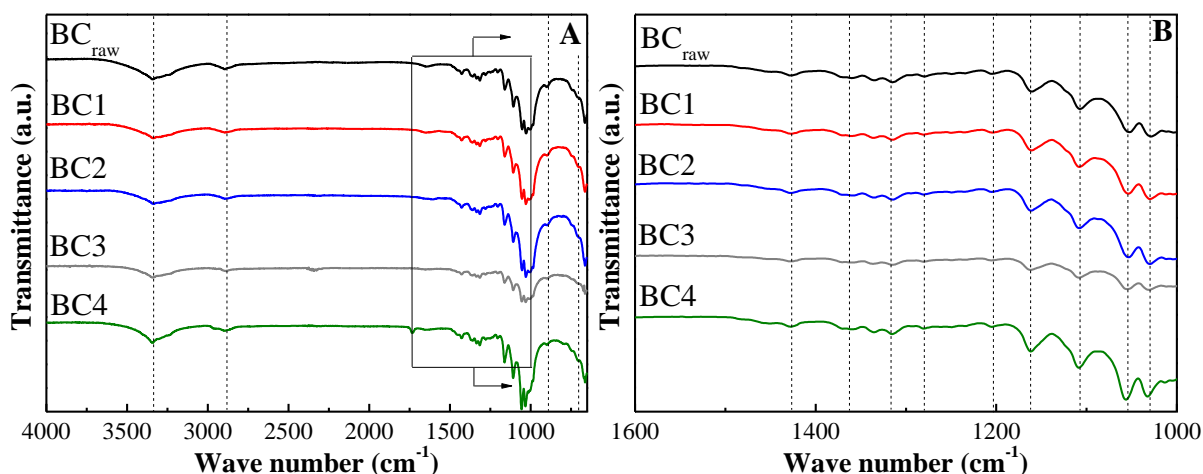


Figure 11 - FTIR spectra of bacterial cellulose before (BC_{raw}) and after sonication (BC1, BC2, BC3 and BC4) from: (A) 4000 - 650 cm⁻¹ and (B) 2000 - 1250 cm⁻¹.

All samples showed bands around 3340, 2920, 1630, 1420, 1370, 1320, 1270, 1240, 1200, 1160, 1100, 1050, 1030, 985, 897 and 660 cm⁻¹, Figure 11.

The band at ~3340 cm⁻¹ is characteristic of -OH stretching of cellulose (SPINACÉ *et al.*, 2009; LU *et al.*, 2014; PRADO and SPINACÉ, 2015; LEITE, ZANON and MENEGALLI, 2017; AZRINA *et al.*, 2017; TIBOLLA *et al.*, 2017; MAHARDIKA *et al.*, 2018). While the region at ~2920 cm⁻¹ is usually attributed to -C-H bond stretching of cellulose (LU *et al.*, 2014; PRADO and SPINACÉ, 2015; SINGH *et al.*, 2017; LEITE, ZANON and MENEGALLI, 2017; MAHARDIKA *et al.*, 2018; SANTOS *et al.*, 2018).

However, the peak at ~1630 cm⁻¹ is due to the bending of absorbed water molecules (CHEN, YU and LIU, 2011; PENG *et al.*, 2013; LU *et al.*, 2014; SINGH *et al.*, 2017; ÖZGENÇ *et al.*, 2017; BALAKRISHNAN *et al.*, 2017; MAHARDIKA *et al.*, 2018).

Around 1430 cm^{-1} there is a $-\text{CH}_2$ bending of cellulose, related to its crystalline structure of allomorph I (YILDIZ and GÜMÜSKAYA, 2007; ROSA *et al.*, 2010; MAHESWARI *et al.*, 2012; PRADO and SPINACÉ, 2015; MANZATO *et al.*, 2017).

The band at $\sim 1370\text{ cm}^{-1}$ reflects the $-\text{C-H}$ deformation in cellulose (ROSA *et al.*, 2010; MAHESWARI *et al.*, 2012; PRADO and SPINACÉ, 2015; TIBOLLA *et al.*, 2017). Moreover, the region at $\sim 1320\text{ cm}^{-1}$ is characteristic of deformation of $-\text{O-H}$ groups in cellulose (SPINACÉ *et al.*, 2009; PRADO and SPINACÉ, 2015) and, based on Oh *et al.*, 2005, the peak at $\sim 1270\text{ cm}^{-1}$ corresponds to $-\text{C-O-H}$ bending in cellulose. Between 1230 and 1250 cm^{-1} possibly there is an angular deformation of $-\text{C-H}$ in cellulose (SPINACÉ *et al.*, 2009) and the band at $\sim 1160\text{ cm}^{-1}$ is assigned to asymmetric bridge stretching of $-\text{C-O-C}$ group in cellulose (LIANG and MARCHESSAULT, 1959; PRADO and SPINACÉ, 2015; SINGH *et al.*, 2017; MANZATO *et al.*, 2017; ÖZGENÇ *et al.*, 2017). The region at $\sim 1200\text{ cm}^{-1}$ reflects the bending of $-\text{OH}$ group of cellulose (OH *et al.*, 2005; ÖZGENÇ *et al.*, 2017).

Around 1100 cm^{-1} possibly there is a stretching of a cellulose ring (LIANG and MARCHESSAULT, 1959; SCHWANNINGER *et al.*, 2004; SPINACÉ *et al.*, 2009). The band at $\sim 1050\text{ cm}^{-1}$ is attributed to $-\text{C-O-C}$ ring skeletal vibration in cellulose (LU *et al.*, 2014; SINGH *et al.*, 2017).

The region at $\sim 1030\text{ cm}^{-1}$ possibly is due to deformation of $-\text{C-O-}$ group in cellulose (ÖZGENÇ *et al.*, 2017) as well as the peak at $\sim 985\text{ cm}^{-1}$ could be related to $-\text{C-O-}$ stretching also in cellulose (PASTAROVA *et al.*, 1994; GWON *et al.*, 2010). These two attributions are characteristic of cellulose I (OH *et al.*, 2005).

The band around 897 cm^{-1} reflects $-\text{C-H}$ deformation of cellulose I (NELSON and O'CONNOR, 1964; TOMAK *et al.*, 2013; PRADO and SPINACÉ, 2015; AZRINA *et al.*, 2017; MANZATO *et al.*, 2017). The last common region in all samples was $\sim 660\text{ cm}^{-1}$ that possibly corresponds to $-\text{C-OH}$ out-of-plane bending in cellulose (MULINARI *et al.*, 2009).

Therefore, as expected, it was confirmed the presence of only cellulose in all samples, and there was no change in the main chemical structure of sonicated samples of bacterial cellulose.

4.1.2 Chemical structure of viscose residue

FTIR spectra of viscose samples before (VR_{raw}) and after HIUS (VR1, VR2, VR3 and VR4) are shown in Figure 12.

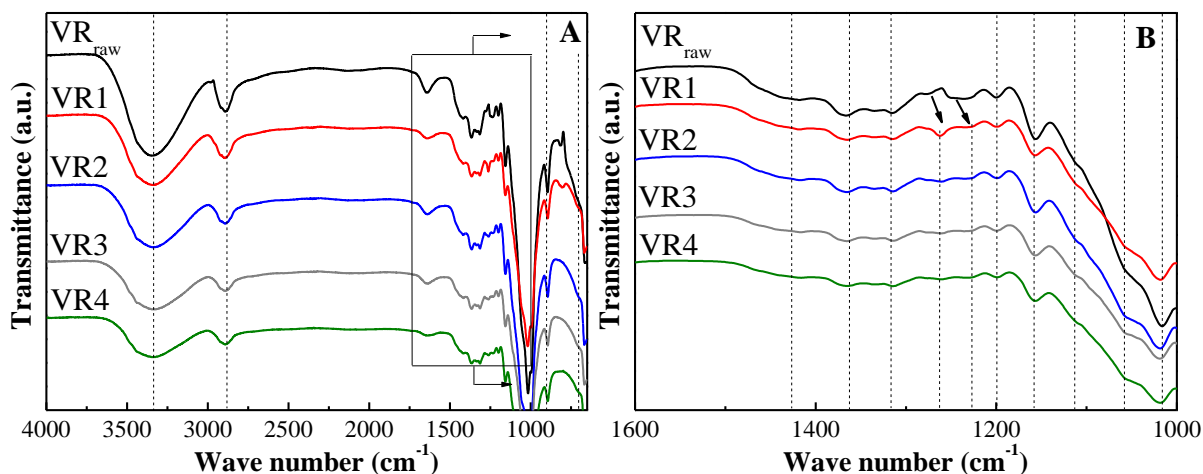


Figure 12 - FTIR spectra of viscose residues before (VR_{raw}) and after sonication (VR1, VR2, VR3 and VR4) from: (A) 4000 - 650 cm⁻¹ and (B) 2000 - 1250 cm⁻¹.

All samples showed peaks at ~3340, 2920, 1630, 1418, 1370, 1320, 1265, 1233, 1200, 1110, 1050, 1015, 985, 895 and 660 cm⁻¹, Figure 12. The region around 1630 cm⁻¹ is due to moisture. All other bands correspond to cellulose, as discussed for bacterial cellulose (Figure 11, p. 28). However, some differences must be explained.

For example, between 1420 and 1430 cm⁻¹ there was a -CH₂ bending of cellulose, related to its crystalline structure (YILDIZ and GÜMÜSKAYA, 2007; ROSA *et al.*, 2010; MAHESWARI *et al.*, 2012; PRADO and SPINACÉ, 2015; MANZATO *et al.*, 2017). It is interesting to note that bacterial cellulose showed a band at ~1430 cm⁻¹ (Figure 11, p. 28) while in viscose samples (Figure 12) it was shifted to 1418 cm⁻¹. According to Nelson and O'Connor (1964), this shift implies the presence of cellulose II, which corroborates the XRD data (Figure 19, p. 43). It is important to observe that even the sonicated samples showed this shift to 1420 cm⁻¹ what indicates there is still cellulose II in sonicated viscose samples (NELSON and O'CONNOR, 1964; OH *et al.*, 2005).

Other difference between cellulose allomorphs I and II was detected at ~1160 cm⁻¹. This region is attributed to the asymmetric bridge stretching of -C-O-C- cellulose group (LIANG and MARCHESSAULT, 1959; PRADO and SPINACÉ, 2015; SINGH *et al.*, 2017; MANZATO *et al.*, 2017; ÖZGENÇ *et al.*, 2017). In bacterial cellulose (Figure 11, p. 28) it was at ~1160 cm⁻¹, which is common in cellulose I, and in viscose samples (Figure 12) it was at ~1155 cm⁻¹, which is typical only of cellulose II (NELSON and O'CONNOR, 1964).

A small detail can be seen around 1100 cm⁻¹, which happened due to a stretching of a cellulose ring (LIANG and MARCHESSAULT, 1959; SCHWANNINGER *et al.*, 2004; SPINACÉ *et al.*, 2009). It was strong in bacterial cellulose (Figure 11, p. 28), indicating

cellulose I, while it was only a shoulder in viscose (Figure 12) indicating cellulose II (NELSON and O'CONNOR, 1964).

Further distinctions in the FTIR spectra happened in the regions between 1015~1030 cm^{-1} and at ~990 cm^{-1} . The first appeared because the deformation of -C-O- group (ÖZGENÇ *et al.*, 2017) and the -C-O- stretching (PASTAROVA *et al.*, 1994; GWON *et al.*, 2010) in cellulose, respectively. In bacterial cellulose the peaks were at ~1030 and 985 cm^{-1} (Figure 11, p. 28), characteristic of cellulose I (OH *et al.*, 2005), while in viscose (Figure 12) the peaks were at 1016 and 995 cm^{-1} , characteristic of cellulose II (OH *et al.*, 2005).

The band at 890~900 cm^{-1} can also be mentioned. It was present due to -C-H deformation of cellulose (TOMAK *et al.*, 2013; PRADO and SPINACÉ, 2015; AZRINA *et al.*, 2017; MANZATO *et al.*, 2017). In bacterial cellulose it was at ~897 cm^{-1} (Figure 11, p. 28), which is characteristic of cellulose I, while in viscose it was at ~895 cm^{-1} (Figure 12), common in cellulose II (NELSON and O'CONNOR, 1964).

In addition, there were differences among the viscose samples. Curiously, the original bands at ~1275 and 1240 cm^{-1} in VR_{raw} (Figure 12) were shifted to ~1265 and 1235 cm^{-1} , respectively. Abiral *et al.* (2018) reported the shift in FTIR peaks caused by the HIUS application on bacterial cellulose. However, the other materials analyzed here (bacterial cellulose, curaua and sugarcane bagasse) did not show this behavior after HIUS.

At last, VR_{raw} (Figure 12) showed a band at ~815 cm^{-1} . This can be related to a -C-H group linked to aromatic rings (BARKER, *et al.*, 1959; CASAS *et al.*, 2012) or even to esters, as -CH₃-CO-O- or -C=C-O-C- (EL-HENDAWY, 2006). The problem is that this band could correspond to the presence of hemicellulose or lignin, but there is no other peak in FTIR spectra that corroborate this fact. So, this region possibly is due to an organic impurity that cannot be determined using only FTIR. It is worth to mention that the band at ~815 cm^{-1} was no longer present in FTIR spectra of sonicated samples in Figure 12.

4.1.3 Chemical structure of curaua and sugarcane bagasse

Curaua and sugarcane bagasse are lignocellulosic sources (CARASCHI and LEÃO, 2000; MARQUES, GUTIÉRREZ and DEL RÍO, 2007; SANTOS *et al.*, 2018). Thus, they have not only cellulose as bacterial cellulose and viscose, but also other components, such as hemicellulose and lignin. The lignin, ash and holocellulose contents for samples before sonication (C_{raw} and SCB_{raw}) are presented in Table 3. Holocellulose content is the sum of

amounts of cellulose and hemicellulose, and it can be estimated subtracting the contents of lignin and ashes of the fiber.

Table 3 - Contents of lignin, ash and holocellulose (cellulose and hemicellulose) for curaua (C_{raw}) and sugarcane bagasse (SCB_{raw}).

Fiber	Lignin (%)	Ash (%)	Holocellulose (%)
C_{raw}	16.28	0.01	83.71
SCB_{raw}	29.87	0.32	69.81

The lignin contents for C_{raw} and SCB_{raw} (Table 3) were higher than those reported in literature. Curaua usually shows values from 7.00 to 11.00 % and sugarcane bagasse from 20.00 to 25.00 % of lignin, considering the sum of soluble and insoluble lignin (SATYANARAYANA, ARIZAGA and WYPYCH, 2009; FARUK *et al.*, 2012). On the other hand, the ashes of lignocellulosic fibers are the solid residue produced by combustion in air (MCKENDRY, 2002). Ash content in curaua is usually lower than 1.86 % (CARASCHI and LEÃO, 2000; HOAREAU *et al.*, 2004; MARQUES, GUTIÉRREZ and DEL RÍO, 2007; LEAL NETA *et al.*, 2015) while in sugarcane bagasse is lower than 2.75 % (PANDEY *et al.*, 2000; HOAREAU *et al.*, 2004; GUIMARÃES *et al.*, 2009). The ash content shown in Table 3 is lower than the reported in literature for both samples. This was interesting for sonication because the major components during the HIUS process would be the lignocellulosic ones without other solid residues. Besides that, these low levels are interesting to other applications, as in bioconversion process, *e.g.*, to produce ethanol (PANDEY *et al.*, 2000). These differences among the contents of SCB_{raw} and C_{raw} compared to the literature may be explained because the chemical composition of a lignocellulosic fiber changes according to its species, climate conditions during its cultivation or even how old was the plant (FARUK *et al.*, 2012).

In addition, FTIR was carried out to analyze the chemical groups of curaua and sugarcane bagasse before and after HIUS, Figure 13 A,B and C,D, respectively.

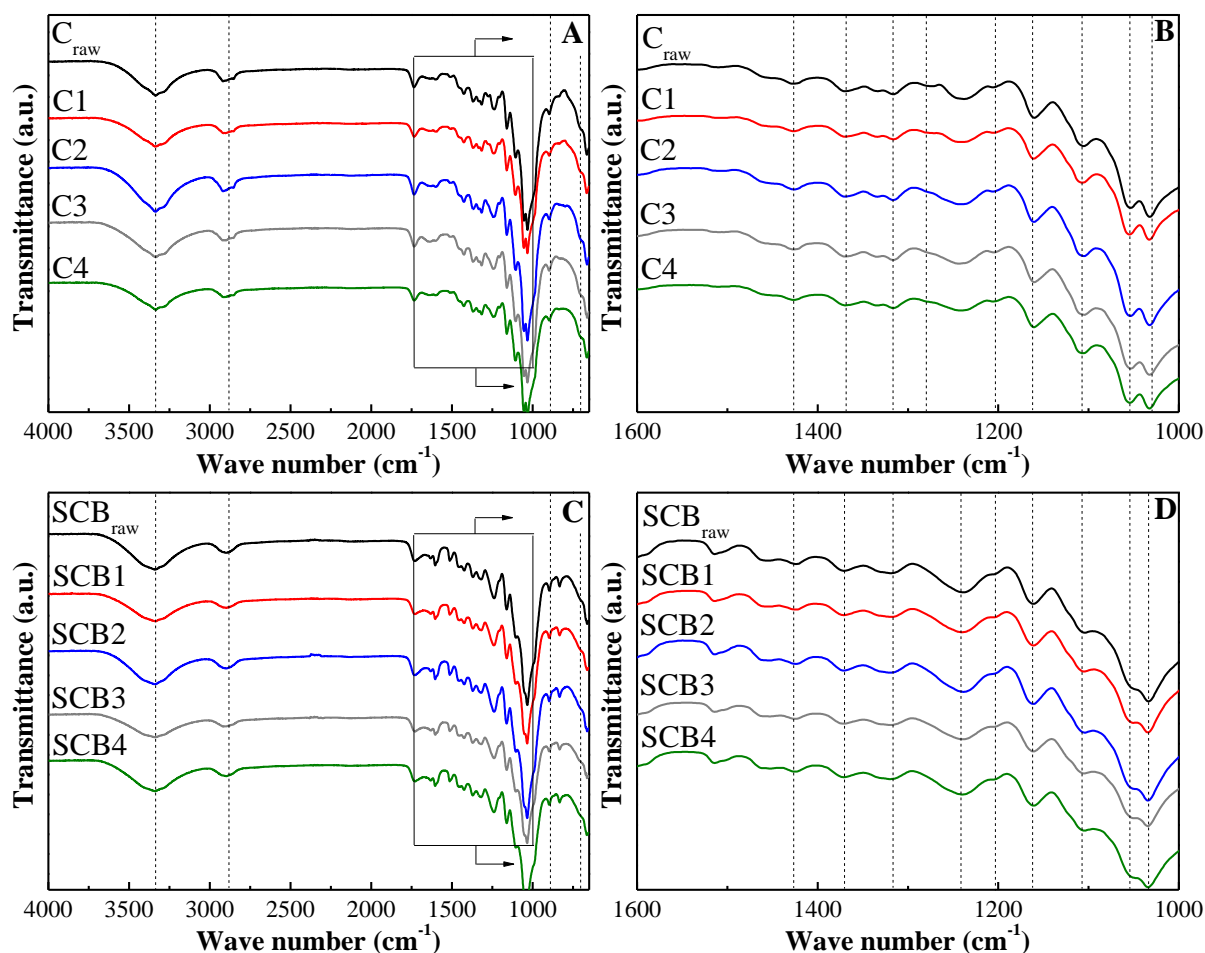


Figure 13 - FTIR spectra of curaua before (C_{raw}) and after sonication (C1, C2, C3 and C4) from: (A) 4000 - 650 cm^{-1} and (B) 2000 - 1250 cm^{-1} ; and FTIR spectra of sugarcane bagasse before (SCB_{raw}) and after sonication (SCB1, SCB2, SCB3 and SCB4) from: (C) 4000 - 650 cm^{-1} and (D) 2000 - 1250 cm^{-1} .

Samples from both sources presented peaks at ~ 3340 , 2920 , 1630 , 1418 , 1365 , 1320 , 1265 , 1233 , 1200 , 1110 , 1050 , 1015 , 985 , 897 and 660 cm^{-1} , Figure 13. Around 1630 cm^{-1} it can be seen the characteristic region assigned to moisture. Meanwhile, all other bands correspond to cellulosic groups, as explained for bacterial cellulose (Figure 11, p. 28). Notwithstanding, some regions must be highlighted. For example, curaua (Figure 13) and sugarcane bagasse (Figure 13) showed bands at ~ 1730 , 1600 , 1510 , 1455 and 835 cm^{-1} .

The peak at $\sim 1730 \text{ cm}^{-1}$ is assigned to stretching of unconjugated -C=O group in hemicellulose (MULINARI *et al.*, 2009; TOMAK *et al.*, 2013; PRADO and SPINACÉ, 2015; AZRINA *et al.*, 2017; TIBOLLA *et al.*, 2017; SANTOS *et al.*, 2018). While between 1600 and 1610 cm^{-1} there is an aromatic ring stretching of lignin (ROSA *et al.*, 2010; ÖZGENÇ *et al.*, 2017; TIBOLLA *et al.*, 2017) as well as at $\sim 1510 \text{ cm}^{-1}$ (MAHESWARI *et al.*, 2012; TOMAK *et al.*, 2013; AZRINA *et al.*, 2017; SANTOS *et al.*, 2018). The band $\sim 1455 \text{ cm}^{-1}$ is also attributed to lignin because of -CH_3 deformation (MAHESWARI *et al.*, 2012; TOMAK

et al., 2013; MANZATO *et al.*, 2017; ÖZGENÇ *et al.*, 2017). Finally, the region at $\sim 835\text{ cm}^{-1}$ is due to aromatic ring vibration of lignin too (TOMAK *et al.*, 2013; TIBOLLA *et al.*, 2017).

As in bacterial cellulose samples (Section 4.3.1, p. 28), no obvious difference could be found in the FTIR spectra comparing samples before and after HIUS. However, it is interesting that the peaks due to hemicellulose ($\sim 1730\text{ cm}^{-1}$) and lignin (~ 1600 , 1510 , 1455 and 835 cm^{-1}) were still present in both materials (Figure 13). It is possible to compare the lignin and hemicellulose content looking at the ratio of intensity of a band in relation to that at 897 cm^{-1} band (ÅKERHOLM, HINTERSTOISSER and SALMÉN, 2004). Based on that, Figure 14 shows the relative intensity of these regions before and after HIUS for curaua and sugarcane bagasse.

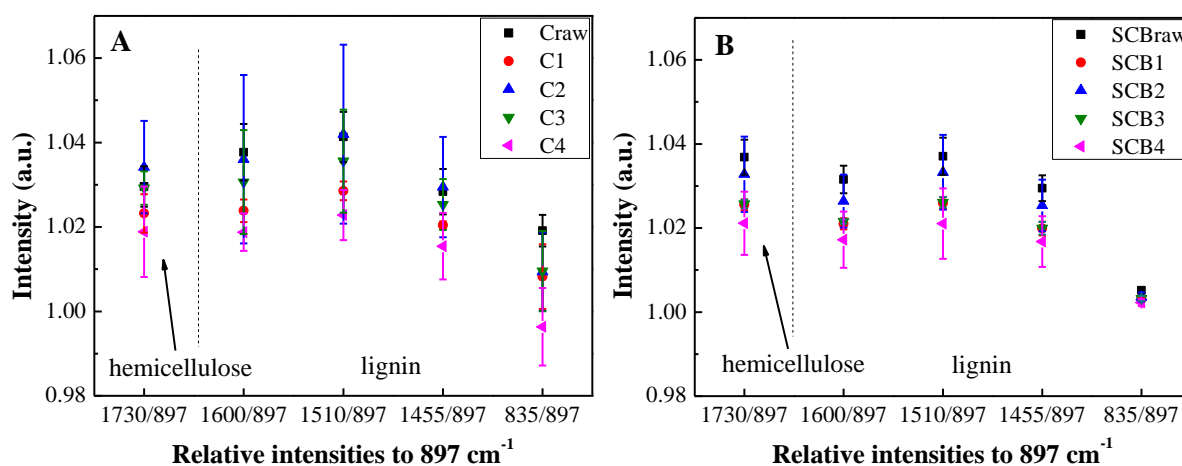


Figure 14 - FTIR relative intensities of curaua (A) and sugarcane bagasse (B) before and after sonication.

The data in Figure 14 allows suggesting that HIUS did not lead to a decreasing of the hemicellulose content, because $I_{1730/897}$ of raw materials was similar to that of the sonicated ones. The same happened to the intensities of regions attributed to lignin, once all samples showed comparable relative intensities to raw curaua (C_{raw} - Figure 14A) and raw sugarcane bagasse (SCB_{raw} - Figure 14B). Nacas *et al.* (2017) stated that HIUS would promote a decreasing on lignin content in curaua, but it was not verified here. There is nothing in the literature about changes in the chemical composition of sugarcane bagasse caused by HIUS.

Possibly, the lignocellulosic components were not removed because the chemical effects produced by HIUS that would degrade them are not common on sonication at 20 kHz (BUSSEMAKER and ZHANG, 2013), which is the frequency of the equipment used in this research. In addition, according to Yang *et al.* (2017), the mechanical effects of HIUS are not sufficient to extract lignin effectively from a lignocellulosic source.

Moreover, it is worth to mention that these residues of hemicellulose and lignin in sonicated samples are not totally undesirable. Several studies reported that these components may inhibit the coalescence of nanocellulose and even improve their dispersion in nonpolar media, such as hydrophobic polymer matrices (MOON *et al.*, 2011; SANTUCCI *et al.*, 2016; KARGARZADEH *et al.*, 2017). This would be interesting for nanocomposite production with matrices of polyethylene, polypropylene, polystyrene, etc. It would not be necessary to add a compatible agent to interact with nanoreinforcement (nanocellulose) and the hydrophobic matrix.

In this context, there was a doubt about where this hemicellulose would be in the sample. Was it dissolved in the aqueous medium or was it present in the nanocellulose structure? In order to confirm the presence of residual hemicellulose in the sonicated samples, AFM-IR was performed for C3 sample (0.2 g / 45 min) extracted from curaua, Figure 15. This sample was chosen because it showed the highest crystallinity index (Table 6, p. 47) as well as the lowest energy demand (Figure 45, p. 78) among all curaua samples.

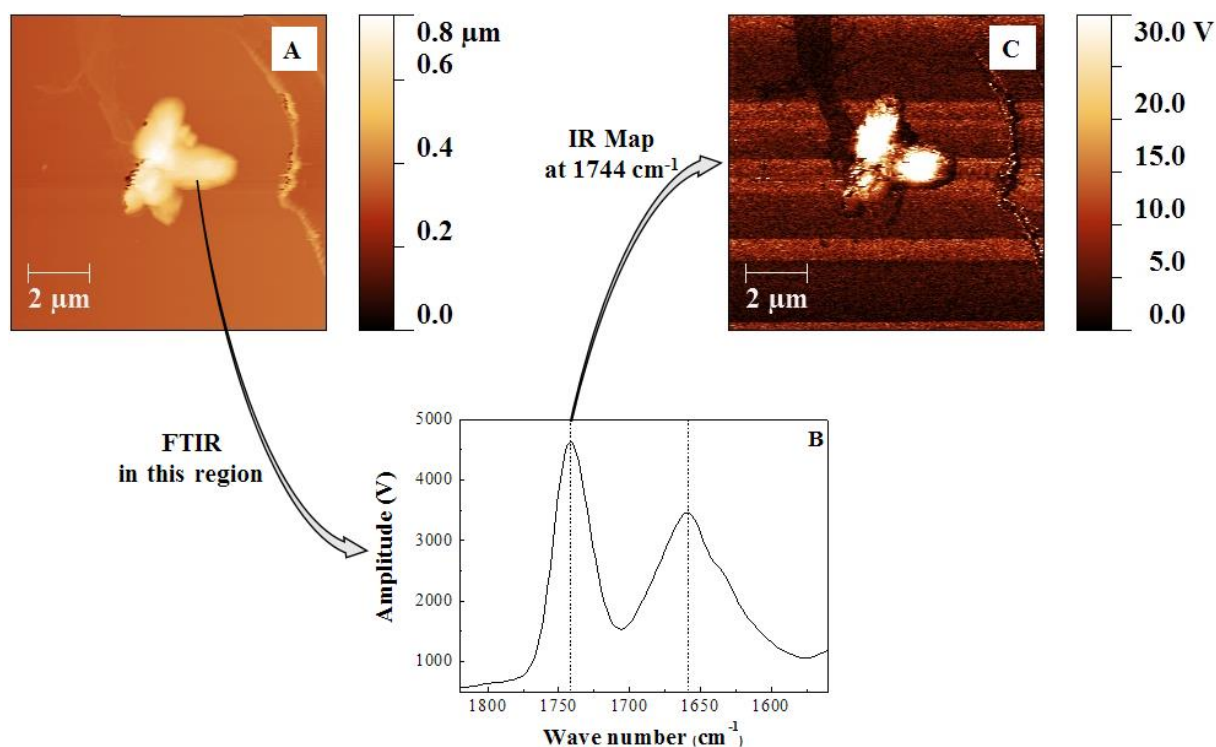


Figure 15 - AFM-IR (contact mode) of C3: topography (A), IR spectra (B) and mapping at 1744 cm^{-1} (C).

In AFM-IR, first it is performed a conventional AFM, characterizing the topography of the sample (Figure 15A). Then, it is possible to apply an infrared beam to this region, obtaining an FTIR spectrum of the nanomaterial (Figure 15B). At last, the operator can

perform a new surface mapping but with the application of the infrared beam in a specific wavenumber (Figure 15C).

It can be seen in Figure 15A that there are no individual particles as those observed in TEM (Figure 37A and B, p. 66), but here there are agglomerates. The IR spectrum (Figure 15B) revealed that the region analyzed in Figure 15A showed bands at ~ 1744 and ~ 1630 cm^{-1} . The signal around 1530 cm^{-1} should be disregarded by equipment limitations. As discussed earlier in this section, the band between 1760 and 1715 cm^{-1} reflects the stretching of --C=O group, which is characteristic of hemicellulose (PRADO and SPINACÉ, 2015; TIBOLLA *et al.*, 2017; SANTOS *et al.*, 2018). Meanwhile, ~ 1630 cm^{-1} is related to water molecules (CHEN, YU and LIU, 2011; PENG *et al.*, 2013; ÖZGENÇ *et al.*, 2017). Curiously, in Figure 15B there were no peaks attributed to lignin, like ~ 1600 cm^{-1} due to aromatic ring stretching according to Rosa *et al.* (2010), Özgenç *et al.* (2017) and Tibolla *et al.* (2017). This indicates lignin is not present or its content in these specific agglomerates is too low to be detected by the AFM-IR sensor.

As 1744 cm^{-1} was the band of interest, this wavenumber was selected and a map was made (Figure 15C) to identify where this --C=O group was. Only the C3 agglomerates showed interaction with this wavenumber, which is shown by their different color (white). This demonstrates nanocellulose agglomerates actually had residual hemicellulose. It is worth to mention that there is nothing in the literature about this topic concerning nanocellulose extracted by HIUS.

Likewise, AFM-IR was carried out to sonicated sugarcane bagasse SCB3 (0.2 g / 45 min), Figure 16.

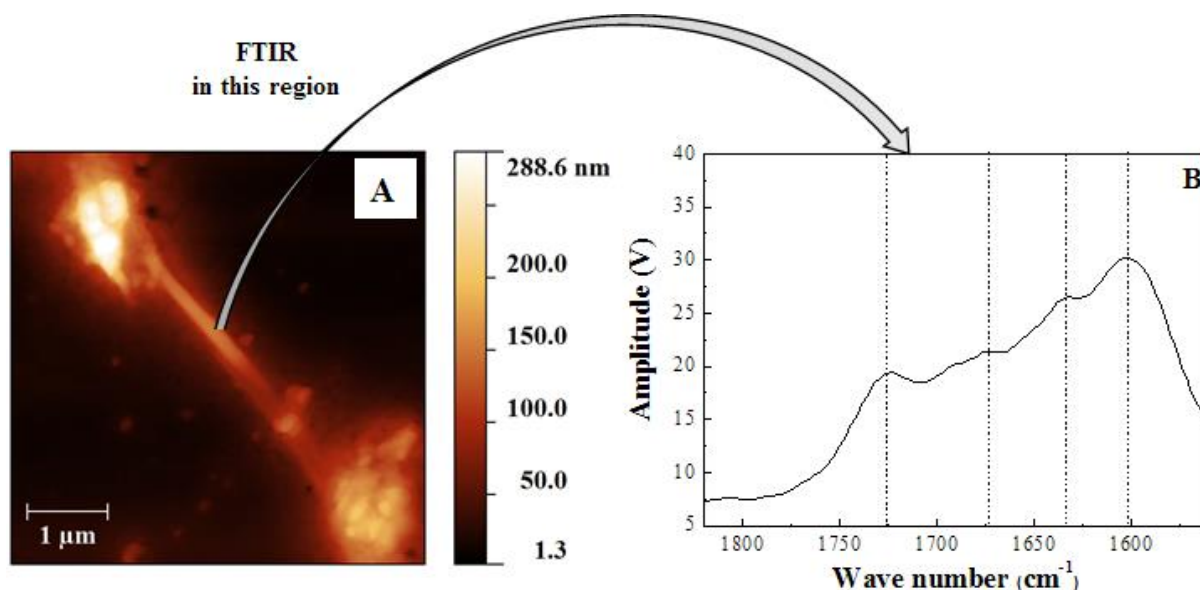


Figure 16 - AFM-IR (contact mode) of SCB3: topography (A) and IR spectra (B).

AFM from SCB3 (Figure 16A) revealed the presence of micrometric agglomerates and nanofibers, similar to TEM results of this sample (Figure 37, p. 66). Moreover, its FTIR spectrum (Figure 16B) showed bands at 1725, 1675, 1630 and 1600 cm^{-1} . The first peak (1725 cm^{-1}) shown in Figure 16B is present due to the -C=O group in hemicellulose (MULINARI *et al.*, 2009; TOMAK *et al.*, 2013; PRADO and SPINACÉ, 2015; AZRINA *et al.*, 2017; TIBOLLA *et al.*, 2017; SANTOS *et al.*, 2018) while 1630 cm^{-1} is assigned to absorbed water molecules (CHEN, YU and LIU, 2011; PENG *et al.*, 2013; LU *et al.*, 2014; BALAKRISHNAN *et al.*, 2017). Both bands were observed in C3 too (Figure 15B), but 1675 and 1600 cm^{-1} were not. These peaks (1675 and 1600 cm^{-1} in Figure 16B) are both attributed to the stretching of aromatic groups in lignin (DASH *et al.*, 2014; SINGH *et al.*, 2015; ÖZGENÇ *et al.*, 2017; TIBOLLA *et al.*, 2017). Thus, this result indicates that nanocellulose SCB3 presented residual hemicellulose and lignin, different of C3 sample which had only hemicellulose. It was not possible to carry out an IR map in these bands due to equipment limitations.

4.1.4 Comparison of chemical structure among cellulose sources

The results of characterizations indicated that raw bacterial cellulose (BC_{raw} , Figure 11, p. 28) and raw viscose residue (VR_{raw} , Figure 12, p. 30) showed exclusively cellulose in their chemical composition. It was possible to check characteristic peaks correspondent to cellulose II in viscose, corroborating the results about crystallinity analysis (Section 4.1.2, p. 41). On

the other hand, in raw curaua and sugarcane bagasse (C_{raw} and SCB_{raw} , respectively, in Figure 13, p. 33) there were cellulose, hemicellulose and lignin.

After the HIUS process, all samples maintained its chemical composition. Only sonicated viscose presented shift in FTIR bands. It is important to note that samples from curaua and sugarcane bagasse still showed the presence of hemicellulose and lignin, both in agglomerates and nanostructures. The residual hemicellulose and lignin are interesting for applications where is necessary to compatibilize the nanocellulose with hydrophobic matrices, such as polyethylene or polypropylene.

4.2 Crystallinity of cellulose before and after sonication process

4.2.1 Crystallinity of bacterial cellulose

Kargarzadeh *et al.* (2017) reported that the crystallinity of nanocellulose is a key property to ensure a better mechanical reinforcement in nanocomposites. Thereby, XRD patterns of bacterial cellulose before (BC_{raw}) and after HIUS (BC1, BC2, BC3 and BC4) were analyzed, Figure 17. BC1 was sonicated during 45 min using 0.1 g, BC2 used 0.1 g during 70 min, BC3 used 0.2 g during 45 min while BC4 used 0.2 g during 70 min, as presented in Table 2 (p. 21).

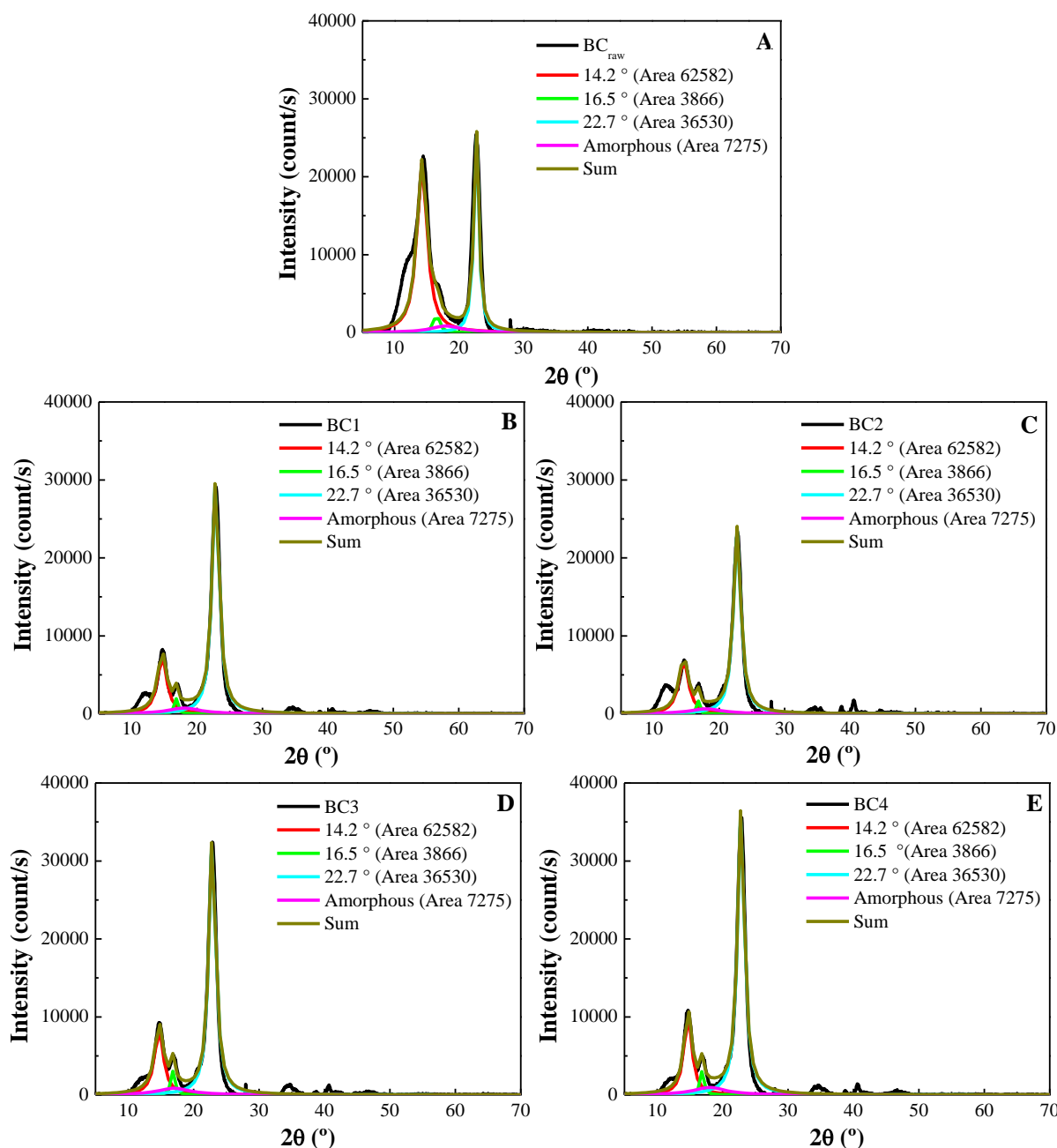


Figure 17 - Representative diffractograms of bacterial cellulose before (BC_{raw} (A)) and after sonication: BC1 (B), BC2 (C) BC3 (D) and BC4 (E).

BC_{raw} (Figure 17A) exhibited diffraction peaks at 14.2°, 16.5°, 22.7°, characteristic of cellulose I (AMIN *et al.*, 2015; GONG *et al.*, 2017). This was also verified by Vanderhart and Atalla (1984) and Tischer *et al.* (2010). Samples BC1, BC2, BC3 and BC4 presented diffraction peaks similar to BC_{raw} (Figure 17). The HIUS process didn't change the crystalline structure, the allomorph I, as expected to bacterial cellulose (TISCHER *et al.*, 2010). The crystallinity indexes (CI) of BC_{raw}, BC1, BC2, BC3, and BC4 were calculated following Eq. 6 (p. 23). CI of each sample is shown in Table 4.

Table 4 - CI values of bacterial cellulose before (BC_{raw}) and after (BC1, BC2, BC3, BC4) sonication.

Material	HIUS time (min)	Mass (g)	CI (%)
BC _{raw}	-	-	92.9 (\pm 0.7)
BC1	45	0.1	92.5 (\pm 0.4)
BC2	70	0.1	93.0 (\pm 0.3)
BC3	45	0.2	91.8 (\pm 1.0)
BC4	70	0.2	93.3 (\pm 1.3)

The CI value of BC_{raw} is not 100 % because its nanofibers are highly ordered, but also show less ordered regions in the network, which are amorphous (TISCHER *et al.*, 2010; SAMIEE *et al.*, 2019). The degree of crystallinity of BC_{raw} (92.9 (\pm 0.7) %) calculated by the deconvolution method, was comparable to the range of values described in the literature (~55 to 88 %) (WONG, KASAPIS and TAN, 2009; PARK *et al.*, 2010; MARTÍNEZ-SANZ *et al.*, 2015; OLIVEIRA *et al.*, 2015).

Average CI value after sonication among all samples in Table 4 was 92.7 (\pm 0.6) %. Although CI value is similar for all samples before and after HIUS, some differences can be verified when applying these values to the equations of 2² factorial planning in order to evaluate the effects of time and mass loading (Eq. 1-4, p. 20). The main effects of time (t) and mass (m) were 1.0 (\pm 0.6) % and -0.2 (\pm 0.6) %, respectively. This means that increase the sonication time increases the crystallinity degree. This corroborates the results presented by Wong, Kasapis and Tan (2009), where bacterial cellulose CI value enhanced gradually with longer sonication times (from 5 to 30 min). On other hand, Abral *et al.* (2018) showed that CI decreased with a longer time (from 30 to 90 min). This reduction in CI values was not observed for the BC samples studied in this Dissertation (Table 4) possibly due to the fact that BC_{raw} was not submitted to previous treatment while Abral *et al.* (2018) applied an electric blender before HIUS.

The interaction effect of time and mass was 0.5 ± 0.6 %. Both mass effect and interaction effect should be disregarded because the standard error is higher than their values (BARROS NETO, SCARMINIO and BRUNS, 1995; BRUNS, BARROS NETO and SCARMINIO, 2006).

At last, CI values of BC samples extracted by HIUS (Table 4) were similar to values of nanocellulose extracted from bacterial cellulose using sulfuric acid and hydrochloric acid (90 and 83 %, respectively) (VASCONCELOS *et al.*, 2017).

4.2.2 Crystallinity of viscose residue

Viscose may contain cellulose I and II, which are difficult to discern using XRD alone (ATALLA and NAGEL, 1974; ATALLA, 1975; HABIBI, LUCIA and ROJAS, 2010; KRUEGER, THOMMES and KLEINEBUDDE, 2010; ADAK and MUKHOPADHYAY, 2016). Because of that, an initial characterization using Raman spectroscopy was carried out for those samples (ATALLA, 1975), Figure 18.

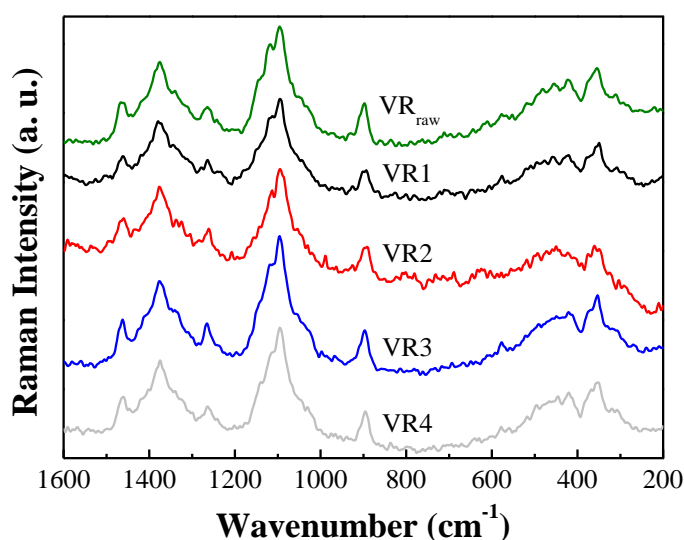


Figure 18 - Raman spectra of viscose before (VR_{raw}) and after sonication (VR1, VR2, VR3 and VR4).

In Figure 18, it was possible to identify peaks at 1461, 1380, 1340, 1265, 1115, 1090, 897, 370 and 354 cm^{-1} . Around 1461 cm^{-1} there is the $-\text{CH}_2$ bending of cellulose (ATALLA, 1975; SEKKAL et al. 1995; SCHENZEL and FISCHER, 2001; WAS-GUBALA and MACHNOWSKI, 2014). It is characteristic of cellulose II because in cellulose I it happens at 1475 cm^{-1} (SCHENZEL and FISCHER, 2001). Furthermore, the bands at 1380 and 1340 cm^{-1} are usually attributed to $-\text{CH}_2$ rocking and wagging of cellulose, respectively (ATALLA, 1975; WAS-GUBALA and MACHNOWSKI, 2014). The peak at 1265 cm^{-1} is also assigned to vibrations of $-\text{CH}_2$ of cellulose II (SEKKAL et al. 1995; SCHENZEL and FISCHER, 2001). Moreover, the regions at 1115 and 1090 cm^{-1} are characteristic of asymmetric and symmetric stretching of $-\text{C}-\text{O}-\text{C}-$ in the cellulose ring, respectively (ATALLA, 1975; WAS-GUBALA and MACHNOWSKI, 2014). It is worth to mention that band at 1115 cm^{-1} in Figure 18 is a small shoulder, close to that at 1090 cm^{-1} . It demonstrates the presence of cellulose II because they would be two distinct bands if the allomorph was cellulose I (ATALLA, 1975; SCHENZEL and FISCHER, 2001; SCHENZEL, ALMLÖF and GERMGÅRD, 2009). The well-defined peak at 897 cm^{-1} in Figure 18 reflects the presence of

-C-H bending (WAS-GUBALA and MACHNOWSKI, 2014) and its high intensity is typical of cellulose II (ATALLA, 1975). Meanwhile, around 370 cm^{-1} there is the deformation of -C-O-C- in the cellulose ring (ATALLA, 1975; WAS-GUBALA and MACHNOWSKI, 2014). At last, the band at 354 cm^{-1} is characteristic of -C-C-C- bending in cellulose chains, assigned to cellulose II (SCHENZEL and FISCHER, 2001; WAS-GUBALA and MACHNOWSKI, 2014). Therefore, viscose samples before and after HIUS showed the presence allomorph II.

XRD patterns of viscose residues before (VR_{raw}) and after HIUS (VR1, VR2, VR3 and VR4) are shown in Figure 19.

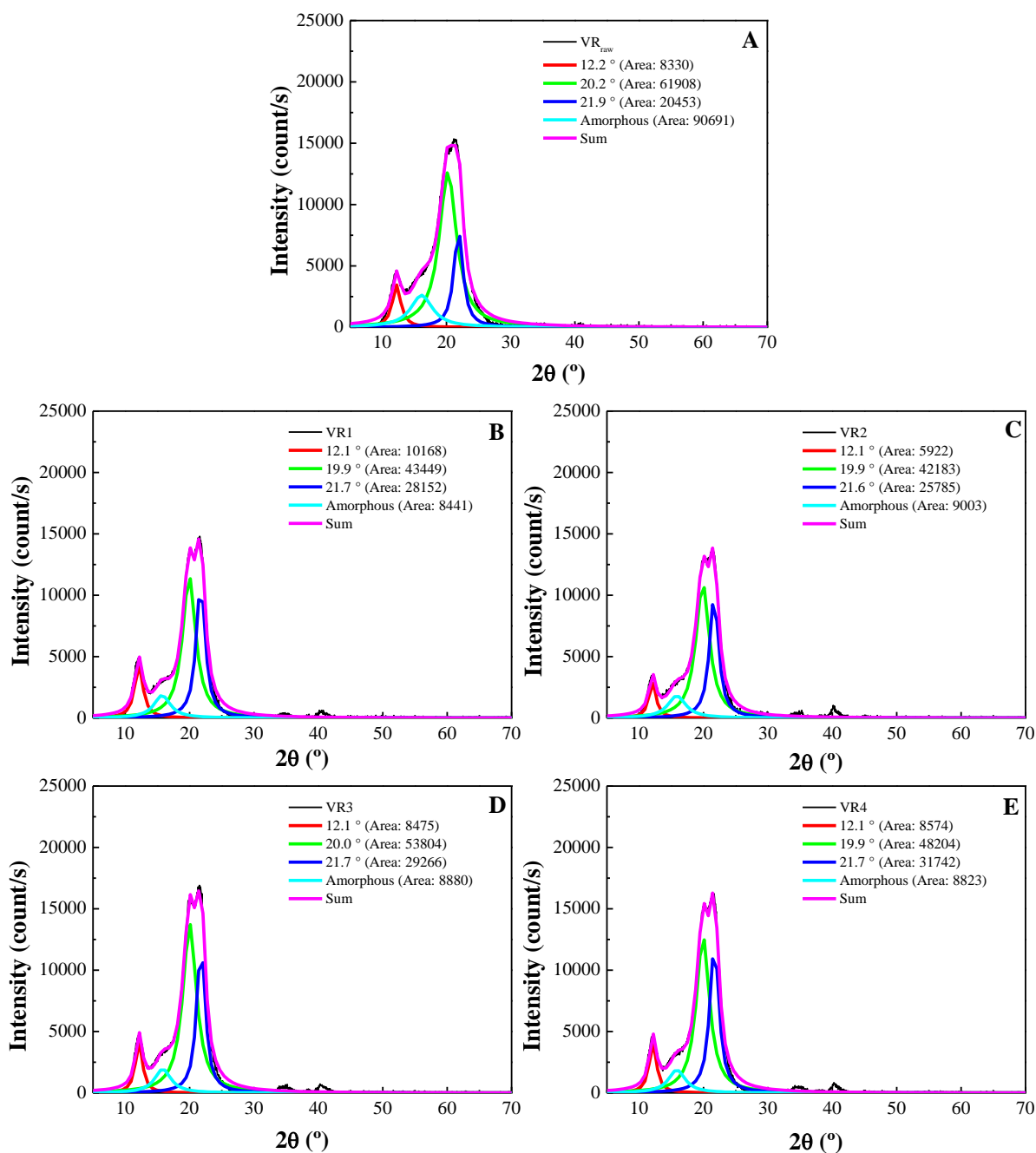


Figure 19 - Representative diffractograms of viscose residues before (VR_{raw} (A)) and after sonication: VR1 (B), VR2 (C), VR3 (D) and VR4 (E).

In all samples of viscose in Figure 19 there were peaks of cellulose II (12.2°, 19.8°, 21.5°) (OH *et al.*, 2005; GONG *et al.*, 2017). The crystallinity indexes (CI) of raw materials were calculated following Eq. 6 (p. 23) and they are shown in Table 5.

Table 5 - CI values of viscose residue before (VR_{raw}) and after (VR1, VR2, VR3, VR4) sonication.

Material	HIUS time (min)	Mass (g)	CI (%)
VR _{raw}	-	-	84.2 (\pm 2.7)
VR1	45	0.1	89.6 (\pm 1.5)
VR2	70	0.1	87.9 (\pm 1.7)
VR3	45	0.2	91.9 (\pm 1.1)
VR4	70	0.2	91.5 (\pm 0.9)

Theoretically, there are no hemicellulose and lignin in VR_{raw} due to the several chemical treatments applied to it during its production (STEPANIK, EWING and WHITEHOUSE, 2000; KRAFT *et al.*, 2013; RÖDER *et al.*, 2013). However, its CI value is not the highest among the raw samples (BC_{raw} - 92.9 (\pm 0.7) %, Table 4, p. 40; C_{raw} - 89.7 (\pm 0.7) %, Table 6, p. 47). This can be explained because during its production, the cellulose chains are dissolved and, thus, they are totally disordered. During the formation of the fibers, the macromolecules are oriented, but it is possible to have some residual amorphous cellulose in it (COLOM and CARRILLO, 2002). Reported value of viscose CI is low (\sim 45 %) (OHSHIMA *et al.*, 2003; ARAÚJO JR *et al.*, 2016) and VR_{raw} showed a higher CI value (84.2 \pm 2.7 %). The comparison with the literature is difficult to this material because is not usual to obtain nanocellulose from viscose.

Based on data presented in Table 5, HIUS seemed to increase the crystallinity index of viscose samples. Average value of CI after sonication among all samples in Table 5 was 90.2 (\pm 1.9) %. In order to quantify influence of HIUS, equations of 2² factorial planning were applied (Eq. 1-4, p. 20). The main effects of time (t) and mass (m) were -1.0 \pm (0.8) % and 3.0 (\pm 0.8) %, respectively. In other words, these values indicate that enhancing of the sonication time and of the mass loading result, respectively in decreasing and increasing of crystallinity degree. This result corroborates the hypothesis of Wang and Cheng (2009) that changing concentration of suspension during HIUS would affect the nanocellulose properties, but they did not evaluate the impact on crystallinity.

At last, the interaction effect between mass and time was 0.6 (\pm 0.8) %, which means that it is not significant (BARROS NETO, SCARMINIO and BRUNS, 1995; BRUNS, BARROS NETO and SCARMINIO, 2006).

4.2.3 Crystallinity of curaua and sugarcane bagasse

The effect of HIUS on the crystalline structure of curaua and sugarcane bagasse was analyzed as well. Figure 20A-E shows the diffractograms of curaua before (C_{raw}) and after HIUS (C1, C2, C3 and C4), and Figure 21A-E presents the results for sugarcane before (SCB_{raw}) and after HIUS (SCB1, SCB2, SCB3 and SCB4).

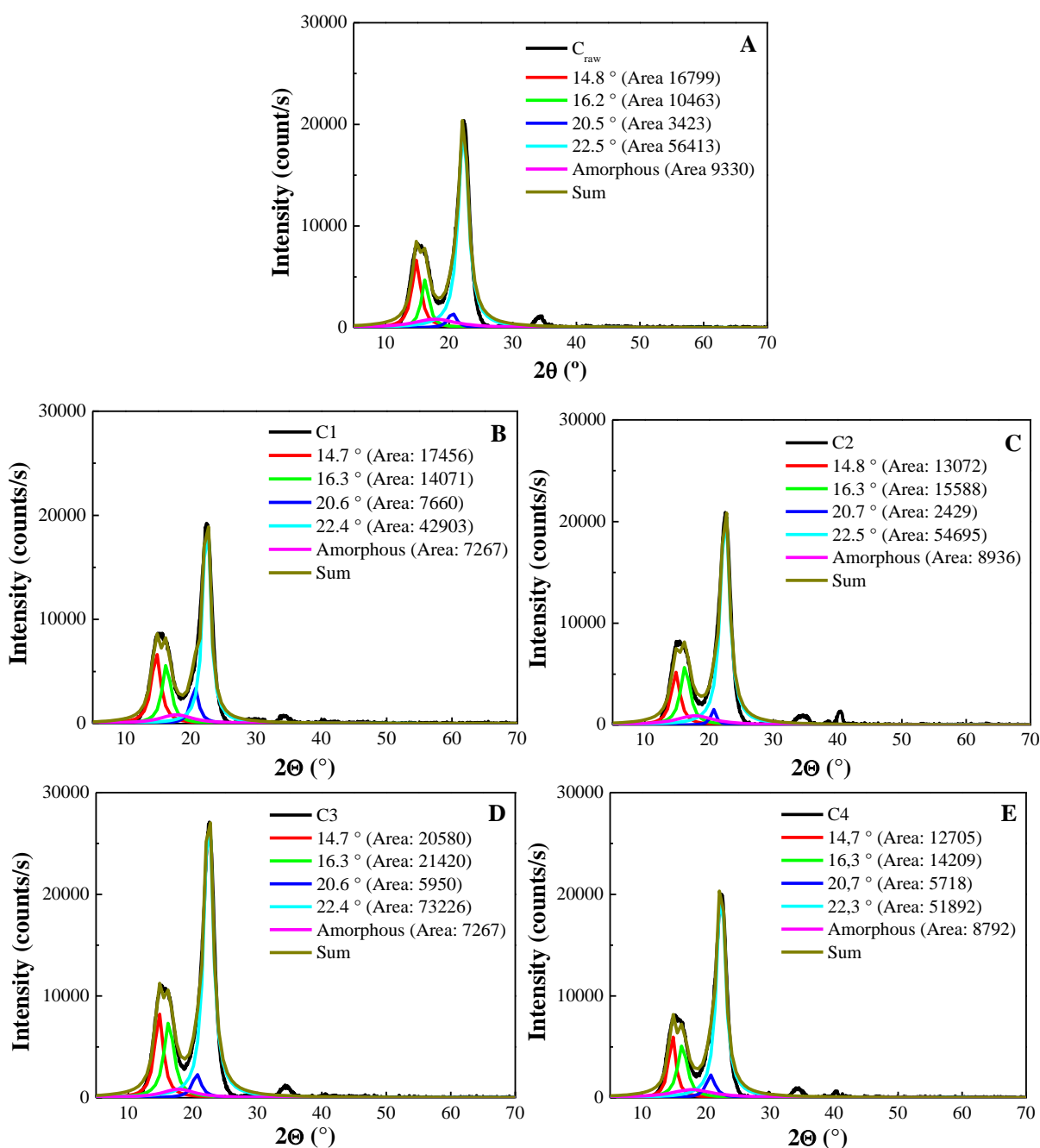


Figure 20 - Representative diffractograms of curaua before (C_{raw} (A)) and after sonication: C1 (B), C2 (C) C3 (D) and C4 (E).

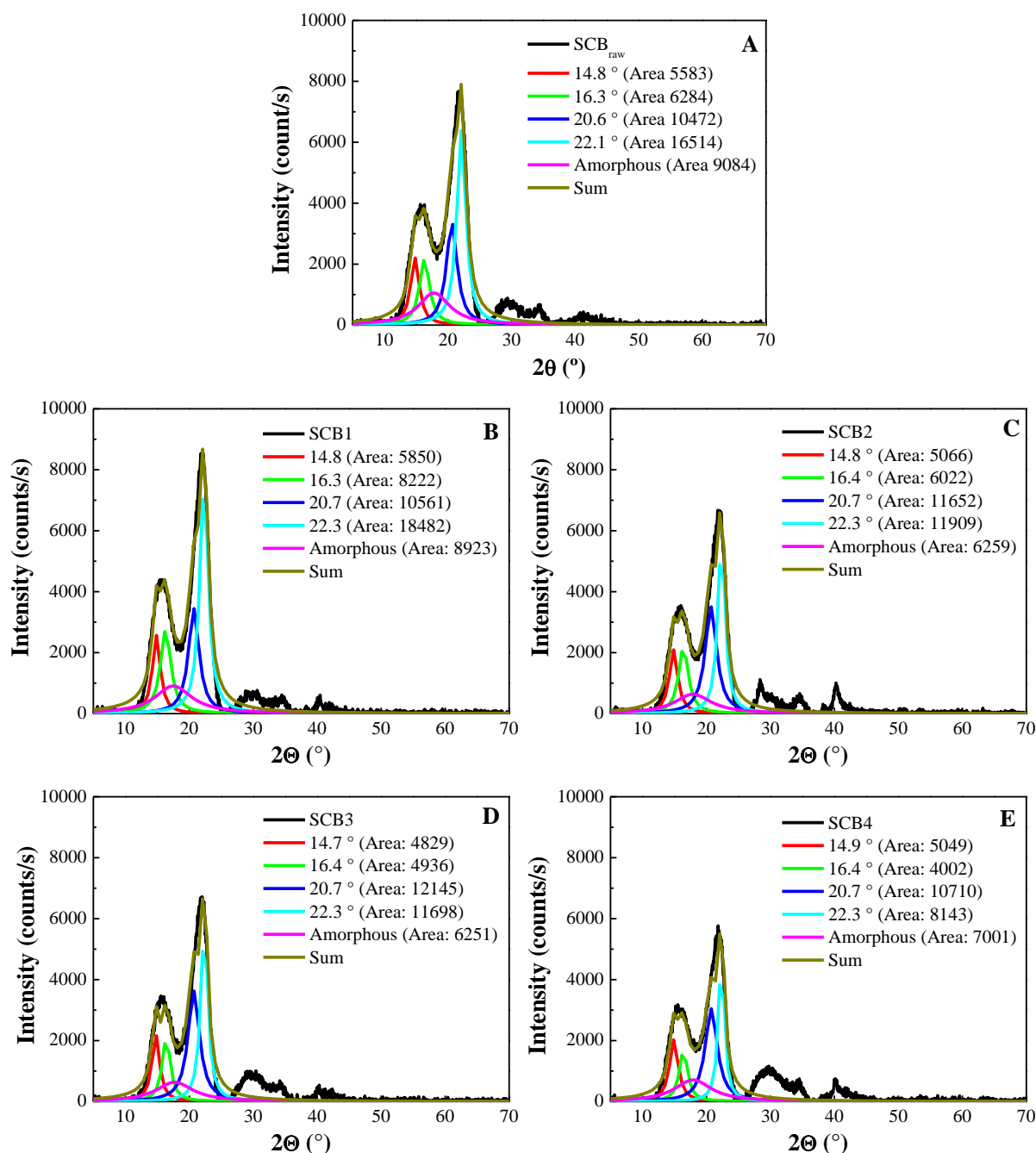


Figure 21 - Representative diffractograms of sugarcane bagasse before (SCB_{raw} (A)) and after sonication: SCB1 (B), SCB2 (C) SCB3 (D) and SCB4 (E).

C_{raw} and SCB_{raw} (Figure 20A and Figure 21A, respectively) showed peaks at 14.8°, 16.3°, ~20.6° and ~22.1°, which are also characteristic of crystalline polymorph I (AMIN *et al.*, 2015; GONG *et al.*, 2017). Similar reports were published by Spinacé *et al.* (2009) and Corrêa *et al.* (2010) for curaua and by Santos *et al.* (2018) for sugarcane bagasse. As happened to bacterial cellulose, the sonicated samples in Figure 20 and Figure 21 showed the same crystalline peaks of their raw materials (C_{raw} and SCB_{raw}): ~14.8, ~16.4, 20.7 and 22.3°.

retaining the cellulose I structure. Nacas *et al.* (2017) also noticed that HIUS process preserved the crystalline structure of curaua.

CI values of samples of curaua and sugarcane bagasse were calculated using Eq. 6 (p. 23), Table 6.

Table 6 - CI of curaua (C_{raw}) and sugarcane bagasse (SCB_{raw}) before and after (C1, C2, C3, C4; SCB1, SCB2, SCB3, SCB4) sonication.

Material	HIUS time (min)	Mass (g)	CI (%)
C_{raw}	-	-	89.7 (± 0.7)
C1	45	0.1	91.7 (± 1.0)
C2	70	0.1	91.0 (± 0.8)
C3	45	0.2	93.8 (± 0.8)
C4	70	0.2	90.4 (± 1.1)
SCB_{raw}	-	-	79.2 (± 0.6)
SCB1	45	0.1	82.8 (± 0.2)
SCB2	70	0.1	84.7 (± 1.2)
SCB3	45	0.2	84.1 (± 0.5)
SCB4	70	0.2	80.0 (± 0.5)

C_{raw} and SCB_{raw} are lignocellulosic sources, in other words, there are cellulose together with amorphous hemicellulose and lignin in their structure (SPINACÉ *et al.*, 2009; KHALIL *et al.*, 2016; SANTOS *et al.*, 2018). As CI value of SCB_{raw} is the lower than CI value of C_{raw} , possibly this fiber shows a higher content of lignin than C_{raw} . This was evaluated on Section 4.3.3 (Chemical composition, p. 31). Campos *et al.* (2013) observed that curaua showed a higher CI value than sugarcane bagasse. Comparing to the literature data, the CI calculated by the deconvolution method of curaua was between 60 and 76 % (CORRÊA *et al.*, 2010; LUNZ *et al.*, 2012; POLETTTO, ORNAGHI JR and ZATTERA, 2014) and of sugarcane bagasse was 60~66 % (MOTAUNG and MOKHOTHU, 2016; MOHOMANE *et al.*, 2017). These differences occurred to curaua possibly because Corrêa *et al.* (2010) and Poletto, Ornaghi Jr and Zattera (2014) deconvoluted the diffractograms using Gaussian peak functions. Lunz *et al.* (2012), Motaung and Mokhothu (2016) and Mohomane *et al.* (2017) didn't specify the profile of functions.

The CI value of C_{raw} was 89.7 (± 0.7) % (Table 6) while the average CI after sonication among all samples in Table 6 was 91.7 (± 1.5) %. C1 and C2 showed a little increment in CI while C4 continued basically with the same degree of crystallinity. C3 was the most remarkable sample, with the highest CI among all samples of curaua, bacterial cellulose (Table 4) and sugarcane bagasse (Table 6).

Meanwhile, the average CI of SCB_{raw} was $79.2 \pm (0.6) \%$ (Table 6) and the average CI after sonication among all samples in Table 6 was $82.9 (\pm 2.1) \%$. Excepting SCB4, the sonicated samples showed a higher degree of crystallinity than SCB_{raw} (especially BC2 and BC3, with increment of 5.5 and 4.9 % respectively), Table 6. This similarity between SCB_{raw} and SCB4 happened possibly because the cavitation effects are non-selective, *i.e.* the crystalline regions can be as affected as the amorphous ones (LI, YUE and LIU, 2012; NACAS *et al.*, 2017). However, the enhancement of CI in most samples extracted from curaua and sugarcane bagasse suggests their amorphous regions (hemicellulose and lignin) were partially degraded. Further results about characterization of hemicellulose and lignin are shown in Section 4.3.3 (p. 31).

The main and interaction effects, with their standard errors, were calculated (Eq. 1-4, p. 20) in order to quantify the influence of mass and time during HIUS.

For curaua samples, the main effects of time (t) and of mass (m) were $-2.1 (\pm 0.5) \%$ and $0.8 (\pm 0.5) \%$, respectively. So, longer times of sonication promote a reduction of crystallinity degree while higher mass loading promotes an increasing of the CI. Comparing the values of t and m, it was possible to check that the time of process had more influence on HIUS than the mass of raw material, which was also observed by Bussemaker and Zhang (2013). Finally, the interaction effect was $-1.4 (\pm 0.5) \%$, indicating that to join mass and time are not interesting to enhance CI of curaua samples.

For sugarcane bagasse (SCB) samples, the main effect of time was $-1.1 (\pm 0.4) \%$, pointing out that change from level 1 (45 min) to level 2 (70 min) may reduce the value of CI. This result is remarkable because it is new in the literature about nanocellulose extracted from SCB using HIUS. All studies so far applied a fixed time (10~40 min) and they did not consider the influence of this factor on the nanocellulose properties (CAMPOS *et al.*, 2013; SANTUCCI *et al.*, 2016; URIBE, CARVALHO and TARPANI 2016; ZHANG *et al.*, 2016; URIBE *et al.*, 2017; BAHRAMI *et al.*, 2018; FENG *et al.*, 2018; GRANDE *et al.*, 2018). Concurrently, the main effect of mass was $-1.7 (\pm 0.4) \%$. *I.e.*, increasing the mass loading from 0.1 to 0.2 g could drop CI too. Velmurugan and Muthukumar (2012) also suggested that the sonication of a lower mass would be the most important effect for delignification of SCB, which could increase its CI. However, it is important to considerate that Velmurugan and Muthukumar (2012) evaluated the influence of ultrasound combined with chemical treatment using NaOH. Wang and Cheng (2009) sonicated regenerated and pure cellulose fibers and observed that a high mass led to low fibrillation. They explained this because the microbubbles, before collapse, would not be able to stir the suspension substantially. So, the

raw materials had a lower chance of pass the probe tip and fully suffer the HIUS. At last, the interaction factor was $-2.9 (\pm 0.4) \%$, indicating that to join mass and time is the worst condition, leading to the lowest CI, similar to what happen for curaua.

4.2.4 Comparison of crystallinity degree among cellulose sources

Figure 22 shows values of the average crystallinity indexes (CI) as a function of raw materials and their sonicated samples with mass loading of 0.1 or 0.2 g and sonication time of 45 or 70 min. Data of viscose samples are separated (Figure 22B) because they show crystalline structure of cellulose II, while samples of other sources are cellulose I (Figure 22A).

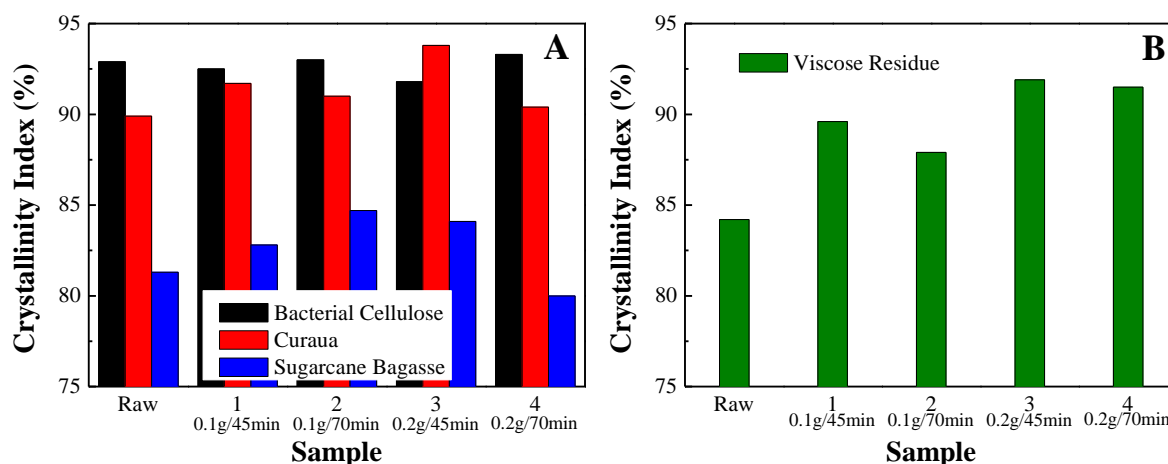


Figure 22 - Average of crystallinity indexes as a function of raw materials and their sonicated samples with mass loading (0.1 or 0.2 g) and sonication time (45 or 70 min).

The source of cellulose with the highest crystallinity index was bacterial cellulose, Figure 22. It was expected because it is pure cellulose without other components as hemicellulose, lignin, extractives or pigments. The other source which has only cellulose in its composition is viscose, but its CI was not as high as of the raw bacterial cellulose one. This difference happened possibly due to the chemical process of regeneration of viscose fibers, which would result in residual amorphous cellulose.

Sugarcane bagasse was the source of nanocellulose that resulted in material with the lowest CI value among all raw samples in Figure 22. This could be related to the presence of high amount of amorphous components in its structure, such as hemicellulose and lignin.

Analyzing the data in Figure 22 it is possible to check that HIUS allowed an increasing in CI of: 3 % in the sugarcane bagasse samples (comparing SCB₂ to SCB_{raw}), 4 % in the curaua

samples (comparing C3 to C_{raw}), and 8 % in viscose residue samples (comparing VR3 to VR_{raw}). For bacterial cellulose, it was not observed remarkable effects of HIUS on crystallinity compared to the other sources (C_{raw}, SCB_{raw} and VR_{raw}). In this manner, it is possible to affirm that HIUS can be used to produce a nanomaterial that can provide a better mechanical reinforcement in a composite than a raw cellulosic fiber.

Table 7 summarizes the main effects and interaction effect of all materials, in order to compare the HIUS effect on these different sources of cellulose. Disregarded effects due to their high standard errors were not considered.

Table 7 - Main effects of time (t) and mass (m) and interaction effect of combined factors (tm) for crystallinity index of nanocellulose from bacterial cellulose, curaua, sugarcane bagasse and viscose residue.

Source	t (%)	m (%)	tm (%)
Bacterial Cellulose	1.0 ± 0.6	-	-
Curaua	-2.1 ± 0.5	0.8 ± 0.5	-1.4 ± 0.5
Sugarcane Bagasse	-1.1 ± 0.4	-1.7 ± 0.4	-2.9 ± 0.4
Viscose Residue	-1.0 ± 0.8	3.0 ± 0.8	-

Only the bacterial cellulose samples presented a significant value for time effect (Table 7). It seems that if there is only cellulose in the medium, especially cellulose I, so longer sonications can increase the crystallinity index. Moreover, its morphology of the raw material is different from the others (p. 51), what can also influence here.

Negative effect of “t” for curaua and sugarcane bagasse indicates that to increase time may reduce CI values (Table 7). This is consistent with reports of HIUS application on curaua (NACAS *et al.*, 2017), on eucalyptus (TONOLI *et al.*, 2012) and even on pure cellulose fibers (PINJARI and PANDIT, 2010; LI, YUE and LIU, 2012). There are two possible justifications. First, theoretically, during cavitation in HIUS, hot spots (> 5000 K) are generated when the bubbles collapse and because this process happens in a few microseconds, high cooling rates (> 10¹⁰ K/s) may be observed. Thereby, this cooling rate could inhibit the nanocellulose organization and thus its crystallization too, decreasing its CI (PINJARI and PANDIT, 2010; NACAS *et al.*, 2017). On the other hand, the bubble collapse also results in high pressures (> 500 atm) or shock waves through the liquid. These would promote the separation of cellulose chains inside nanocellulose, lowering their organization and, consequently, the CI too (LI, YUE and LIU, 2012; TONOLI *et al.*, 2012; CAMPOS *et al.*, 2013).

The lignocellulosic sources exhibited distinct main effects of mass (Table 7). Since the morphology and size distribution of their raw fibers were similar (p. 61), possibly this

divergent behavior happened due to the different chemical composition of the sources. Sugarcane bagasse showed a higher level of non-cellulosic components and a negative effect “m” (p. 31). Thereby, increasing mass loading leads to more presence of these non-cellulosic components which can be partially degraded by HIUS, but not removed from specimen, lowering the crystallinity index of the sample. Section 4.3.3 (p. 31) indicates the results about the chemical composition of curaua and sugarcane bagasse, together with their sonicated nanocellulose samples.

Still about the mass effect “m”, it was not significant or it was positive for sonicated bacterial cellulose and sonicated viscose, respectively (Table 7). These results reveal that enhancing mass loading would not damage the crystalline structure of sonicated samples. This is interesting because, as mentioned in Section 4.5 (p. 77), it may allow a process optimization in future studies using HIUS, in order to reduce the energy requirement.

Only lignocellulosic sources (curaua and sugarcane bagasse) showed a significant value for the interaction effect, which was negative (Table 7). It seems if there is only cellulose in the medium (as in bacterial cellulose and viscose residue), the combination of mass and time isn't a strong influential parameter in the HIUS conditions used in this Dissertation.

The behavior of sonicated samples of viscose residue was similar to those of curaua, where the time effect was negative and the mass effect was positive (Table 7), *i.e.*, in order to achieve the highest crystallinity of nanocellulose from VR_{raw}, the best condition should show shortest sonication time and highest mass loading.

For all samples studied in this section it is important to remember that the subtraction of equipment background before the deconvolution could lead to a reduction of the contribution in the XRD patterns of hemicellulose and lignin (curaua and sugarcane bagasse) as well as of amorphous cellulose (viscose and bacterial cellulose).

4.3 Size distribution and morphology of cellulose before and after sonication process

4.3.1 Size distribution and morphology of bacterial cellulose

SEM analysis of bacterial cellulose before sonication (BC_{raw}) was performed to verify its size and morphology, Figure 23.

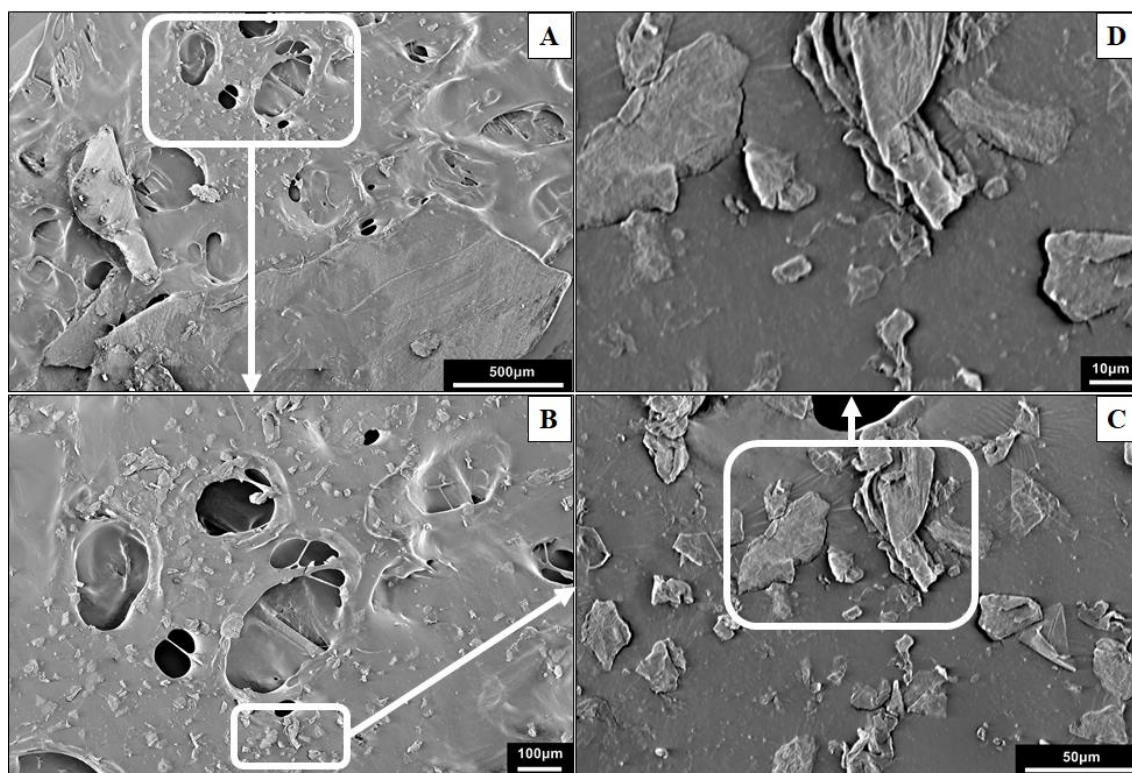


Figure 23 - SEM micrograph of bacterial cellulose before sonication (BC_{raw}) at x50 (A), x100 (B), x500 (C) and x1000 (D).

Looking at Figure 23A it was possible to verify the presence of particles wider than 1 mm. Nevertheless, there are many smaller particles too ($< 50 \mu m$, Figure 23C). Possibly, these would suffer a more intense effect by HIUS than the larger ones. All particles showed a thin thickness, while their shape was irregular. This thin structure may hamper the milling step, explaining why it was so hard to mill and sieve to 100 mesh (0.15 mm), making necessary to use a mesh of 28 mesh (0.59 mm) before sonicating this material.

In addition, it is known that bacterial cellulose shows a network with nanofibers of cellulose (KLEMM *et al.*, 2005; KLEMM *et al.*, 2011). In order to check the BC_{raw} nanostructure, AFM (contact mode) was carried out, Figure 24.

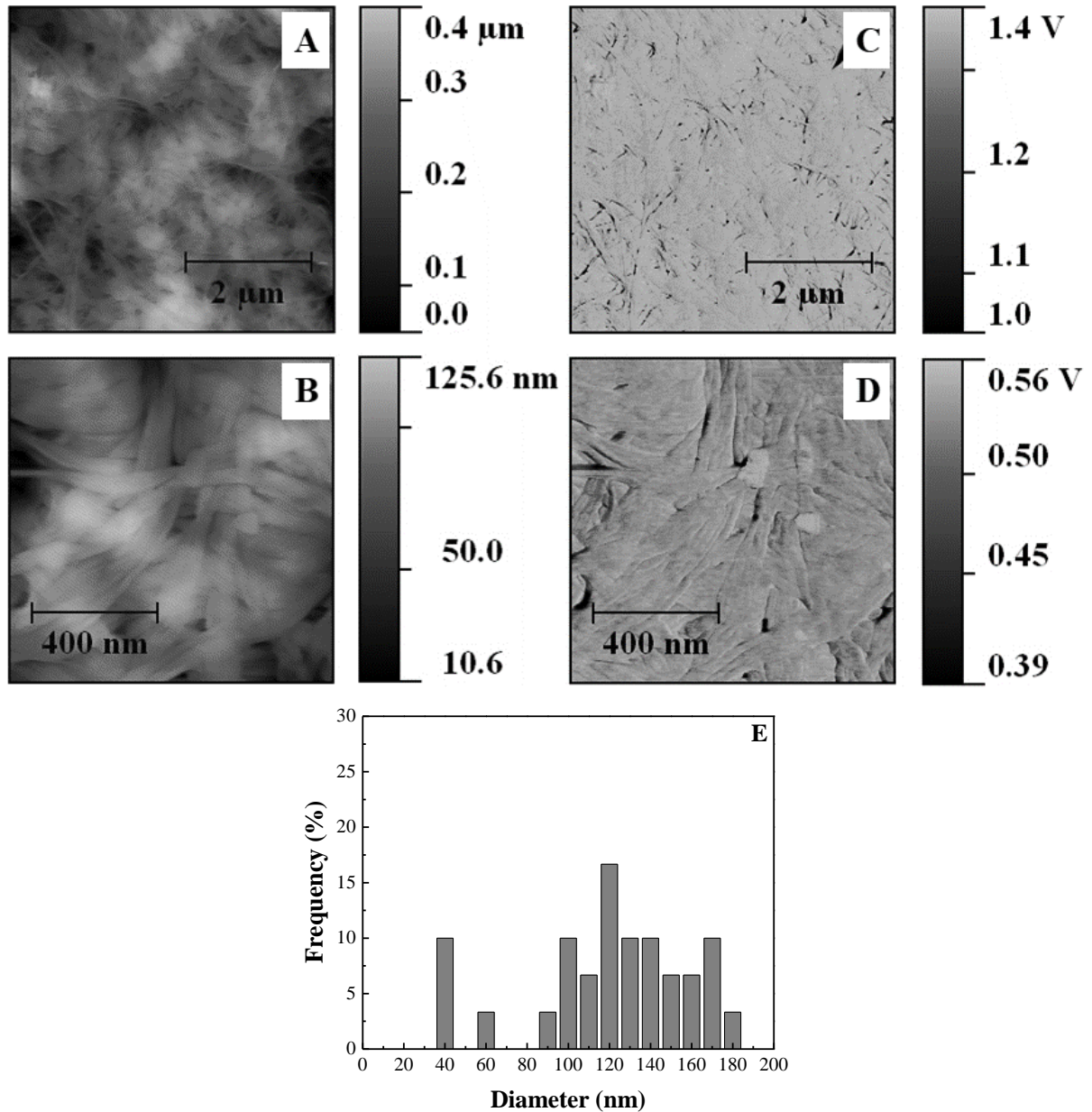


Figure 24 - AFM micrographs (contact mode) of bacterial cellulose before sonication (BC_{raw}): topography (A, B) and friction (C, D); distribution histogram of diameter measured by AFM (E).

BC_{raw} showed a network structure, with random orientation and basically without empty spaces. According to Eq. 7 (p. 24), the weight average diameter of BC_{raw} fibers was 139 nm, with a length higher than 1 μm. The roughness average determined by Gwyddion® was 36 nm. Because of the extension of BC_{raw} fibers, it was not possible to determine their individual length based on AFM imaging (SANTUCCI *et al.*, 2016). Native bacterial cellulose fiber diameter reported in the literature is 10~140 nm (GOELZER *et al.*, 2009; TISCHER *et al.*, 2010).

Besides crystallinity, literature points out that dimensions of the nanocellulose can influence its capacity of increasing properties of a nanocomposite (MARIANO, EL KISSI and

DUFRESNE, 2014). Thus, samples of bacterial cellulose after applying HIUS were characterized first by DLS, Figure 25.

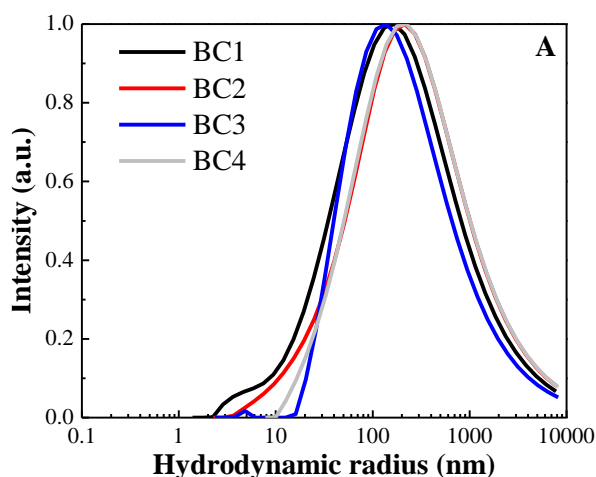


Figure 25 - DLS intensity distribution of sonicated samples of bacterial cellulose.

There were particles in the nano scale range in all sonicated samples, Figure 25. This indicates it was possible to dismantle the membrane structure (Figure 23, p. 52) and isolate the nanostructures using HIUS. All BC samples showed a monomodal distribution. The main peaks of BC1, BC2, BC3 and BC4 were 165, 215, 135 and 210 nm, respectively. Average peak among all samples was 181 (± 38) nm. It is important to note that BC1 exhibited a small shoulder at ~5 nm. All samples (BC1, BC2, BC3 and BC4) presented DLS peaks (Figure 25) smaller than the nanocellulose extracted from bacterial cellulose using acid hydrolysis (WU *et al.*, 2018), whose DLS peaks were 365, 440 and 455 nm. These results indicate that HIUS process would be more effective than the chemical route.

Increasing of sonication time from 45 to 70 min possibly lead to formation of bigger particles, since BC2 and BC4 are bigger than BC1 and BC3 as can be seen in the DLS peaks of Figure 25. Furthermore, the comparison between BC1 (0.1 g) and BC3 (0.2 g) may suggest that a higher mass loading would result in smaller particles.

Even though DLS is a useful technique to analyze nanoparticle sizes, it shows some limitations. The hydrodynamic radius determined by DLS (Figure 25) must not be directly related to length or width of nanocellulose, but it is only an apparent size of the nanomaterial (EL ACHABY *et al.*, 2017; YANG *et al.*, 2017; JAKUBEK *et al.*, 2018). Thereby, AFM was carried out for BC3 sample (0.2 g / 45 min) because it showed the lowest energy consumption among all samples studied in this Dissertation (Figure 45, p. 78). Figure 26 presents the AFM

(contact mode) of BC3 sample. More micrographs of this sample are shown in Figure 49 in the Appendix B (p. 106).

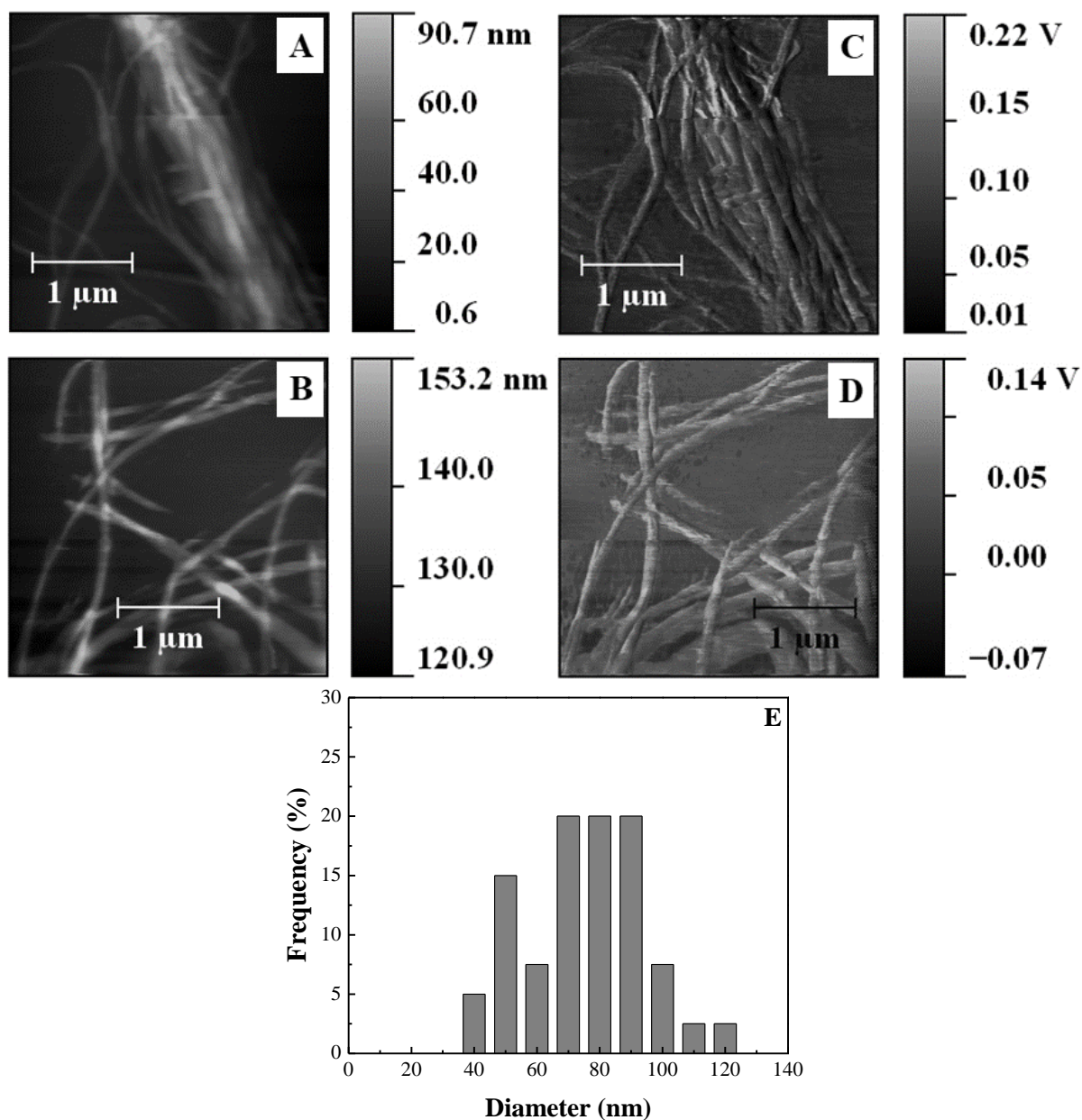


Figure 26 - AFM micrographs (contact mode) of sonicated bacterial cellulose BC3: topography (A, B) and friction (C, D); distribution histogram of diameter measured by AFM (E).

BC3 (Figure 26) showed no longer a network structure as in BC_{raw} (Figure 24, p. 53), but the fibers were separated. It is possible to check, especially at Figure 26A and C, that HIUS promoted the fibrillation of BC_{raw}. The cavitation created by HIUS provides energy of 10 to 100 kJ/mol, which is within the hydrogen bond energy scale (HEATH and THIELEMANS, 2010; CHEN *et al.*, 2011). Thereby, it is possible that this released energy due to cavitation process breaks the hydrogen bond among cellulose chains, allowing the separation of

nanocellulose. This HIUS effect on network structure of bacterial cellulose was also observed by Abrial *et al.* (2018). The value of weight average diameter of BC3 nanofiber, calculated using Eq. 7 (p. 24), was 80 nm and average roughness measured using Gwyddion® was 22 nm. Consequently, BC3 nanofiber was narrower and with smaller roughness compared to BC_{raw} (diameter ~139 nm and roughness ~36 nm).

Tischer *et al.* (2010) used AFM to analyze sonicated BC for 15, 30, 60 and 75 min. They observed roughness decreased after HIUS for all samples. But they stated that with 30 min of HIUS there was no significant distinction in the morphology of BC, mainly in diameter. This result is different of what was observed for BC3 sample possibly because Tischer *et al.* (2010) used a lower HIUS power (200 W).

BC3 length was higher than 1 μm , as BC_{raw}. This would explain why DLS size distribution showed particles above 1 μm (Figure 25).

4.3.2 Size distribution and morphology of viscose Residue

Size distribution of raw viscose residues was determined by optical microscopy. Figure 27 shows the distribution of length (L) and diameter (D) using ImageJ®. Micrographs of this sample are shown in Figure 48 in the Appendix A (p. 105).

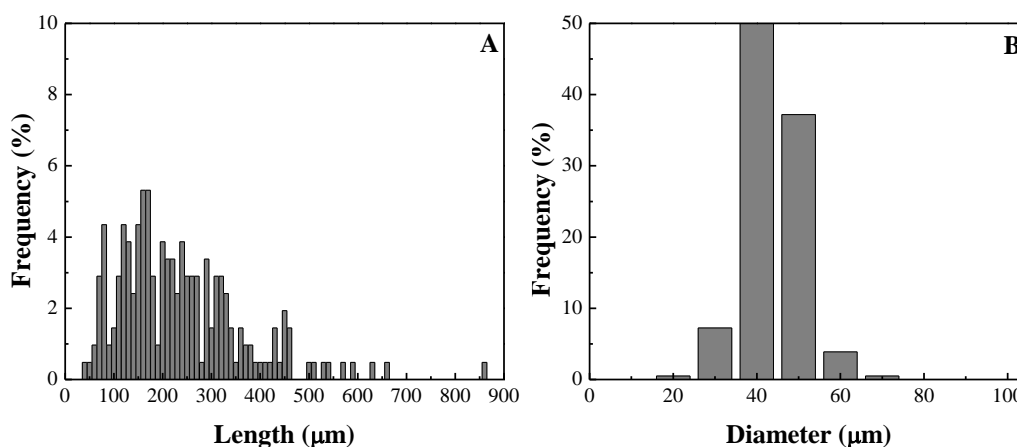


Figure 27 - Distribution histograms of length (A) and diameter (B) for viscose residues before sonication (VR_{raw}).

In Figure 27, the average length and diameter were 305 and 45 μm , respectively. Thus, its aspect ratio (L/D) was 6.48. In addition, morphology of fibers from viscose residue was analyzed using SEM, Figure 28.

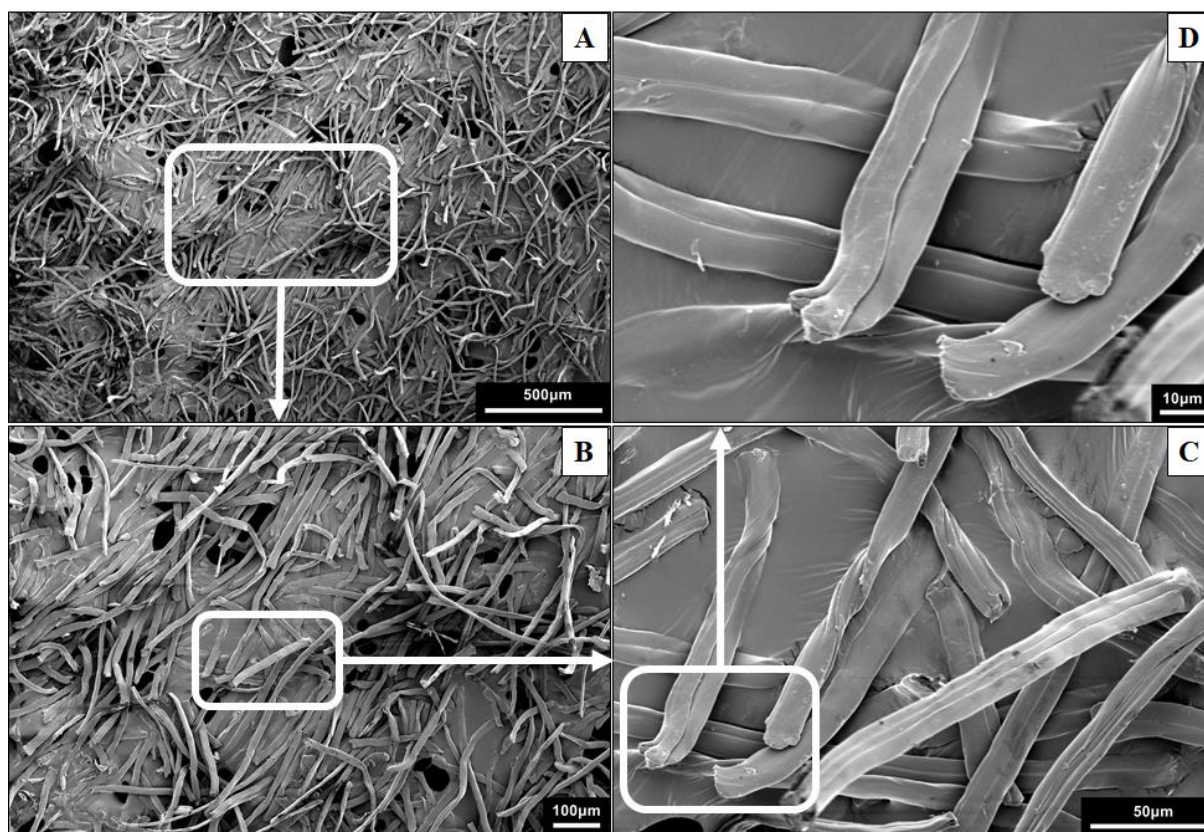


Figure 28 - SEM example of viscose residues before sonication (VRraw) at x50 (A), x100 (B), x500 (C) and x1000 (D).

For VR_{raw} sample it is possible to observe in Figure 28 the presence of bundles with some connected fibers and their surfaces were smooth as expected (HUANG *et al.*, 2008; SINGH and MURTHY, 2017). VR_{raw} dimensions were consistent with those observed by optical microscopy, where the length was 40 to 860 µm and the diameter was 20 to 70 µm (Figure 32).

In order to confirm the nanocellulose presence in sonicated samples, their suspensions were examined by DLS (Figure 29).

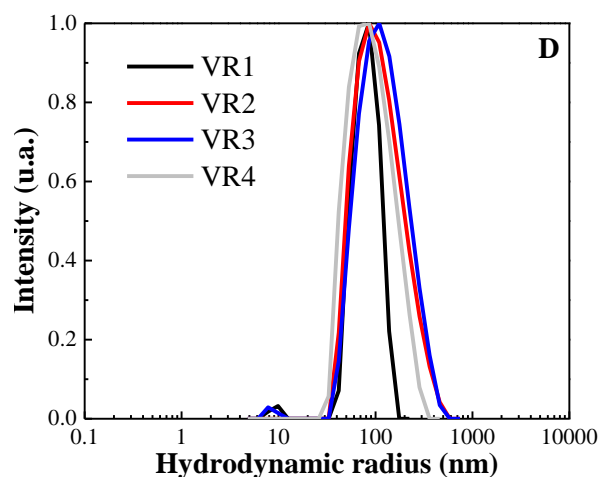


Figure 29 - DLS intensity distribution of sonicated samples of viscose residues.

All sonicated samples from viscose presented particles in the nano scale range and basically a monomodal distribution, Figure 29, indicating it was possible to extract nanocellulose using HIUS. The main peaks of VR1, VR2, VR3 and VR4 were 85, 85, 110 and 80 nm, respectively. Average peak among all samples was $90 (\pm 14)$ nm. It is interesting to note that these peaks were lower than the peaks observed for nanocellulose from bacterial cellulose (Figure 25, p. 54), from curaua and from sugarcane bagasse (Figure 35, p. 64). Although no data are available in literature about DLS measurements for nanocellulose extracted from viscose, there are data about nanocellulose from other regenerated cellulose sources. Cheng *et al.* (2014) reported DLS peaks for nanocellulose from lyocell extracted by acid hydrolysis of around 30, 50 and 95 nm. Thus, HIUS also let the extraction of nanocellulose with comparable dimensions to nanocellulose extracted by chemical route.

Despite of all VR samples had shown particles in the nano scale region (Figure 29), SEM was carried out to check if there would be microscopic residues. VR3 sample was analyzed (Figure 30) due to its high crystallinity index (Table 5, p. 44).

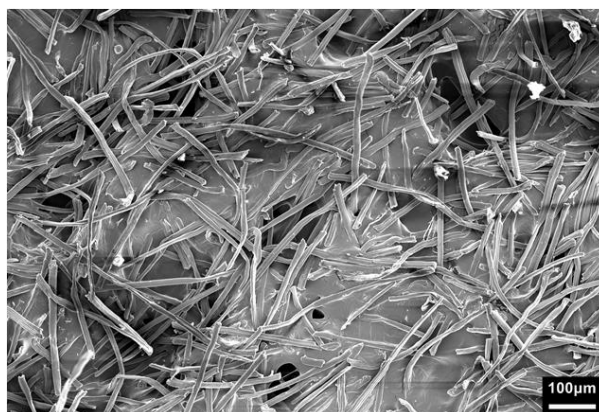


Figure 30 - SEM micrograph at x100 of sonicated viscose residue VR3.

SEM of VR3 sample (Figure 30) showed micrometric fibers, comparable to those observed in the raw material VR_{raw} (Figure 28, p. 57) Based on that, it is possible to state that results from DLS (Figure 29, p. 58) and SEM (Figure 30) indicated the presence of a mixture of particles in micro and nano scales. Cheng, Wang and Han (2010) also verified that application of HIUS on regenerated cellulose (lyocell) during 30 min would create a mixture of micrometric fibers and nanometric ones. Lyocell and viscose are distinct because the solvent used during the process of depolymerization of cellulose is different. Production of lyocell uses the organic solvent N-methyl-morpholine-N-oxide while in the production of viscose the solvent is aqueous solution of sodium hydroxide. However, the general properties of both fibers are similar (COLOM and CARRILLO, 2002). In this manner, it is possible to compare their microscopic fibers and the nanocelluloses extracted from them. The yielding of HIUS process on viscose was evaluated in Section 4.5 (p. 77).

However, it is necessary to keep in mind that DLS analysis suggested the existence of nanometric particles, but its hydrodynamic radius (Figure 29) cannot be related to dimensions of nanocellulose, such as length or width (EL ACHABY *et al.*, 2017; YANG *et al.*, 2017; JAKUBEK *et al.*, 2018). Thereby, TEM was carried out for VR3 sample (0.2 g / 45 min) because this condition showed the highest crystallinity index (Table 5, p. 44) and the lowest energy consumption among those from viscose residue (Figure 45, p. 78). Figure 31 shows some representative TEM micrographs of VR3 as well as the size distribution (length and diameter) considering all measurements. More micrographs of this sample are shown in Figure 50 (p. 107) and Figure 51 (p.108) in the Appendix C.

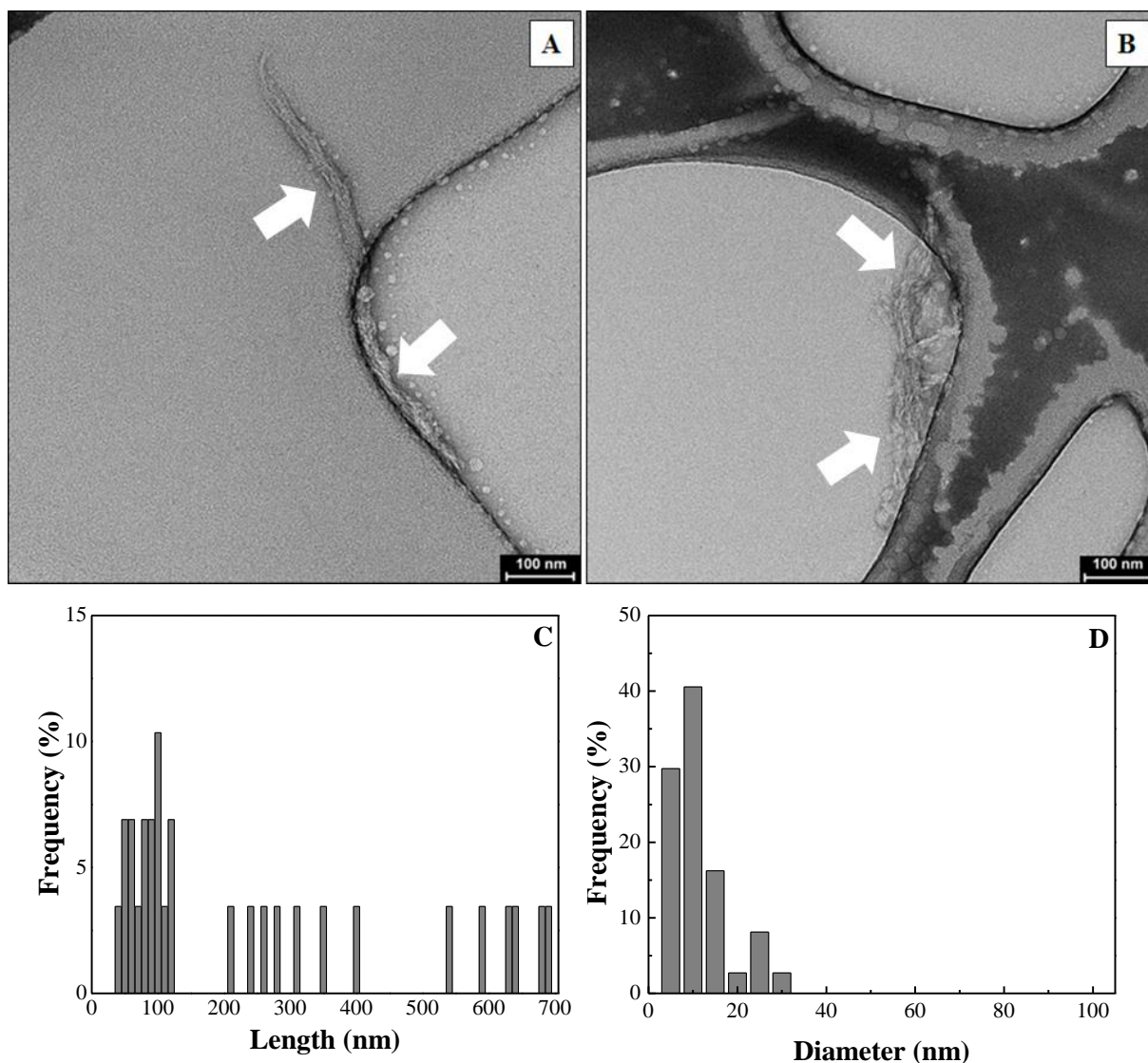


Figure 31 - TEM micrographs of sonicated viscose residue VR3 (A, B) and distribution histograms of length (C) and diameter (D) measured using all TEM micrographs for VR3.

Figure 31A shows cellulose nanofibers while Figure 31B shows the possible presence of cellulose nanocrystals as well. In this manner, HIUS was able to extract nanocellulose from viscose residues with different morphologies. The length of VR3 ranged between 40 and 690 nm and its diameter was around 5 and 30 nm. The weight averages of length and diameter (Eq. 7, p. 24) of VR3 were 438 and 15 nm, respectively, resulting in an aspect ratio of 29.

Cheng, Wang and Han (2010) extracted nanofiber from regenerated cellulose Lyocell, with diameter of 20~30 nm. Ye *et al.* (2018) obtained spherical nanocellulose (diameters of 25~60 nm) from viscose using hydrolysis with ammonium persulfate. Nanofibers extracted from viscose using hydrolysis with sulfuric acid showed average length and diameter of 81 and 37, respectively, with aspect ratio of 2.2 (PRADO, GONZALES and SPINACÉ, 2019). Thus, HIUS allowed the production of nanocellulose with higher aspect ratio than acid

hydrolysis. This is interesting for nanocomposites applications, since higher aspect ratio usually lead to better reinforcement of polymer matrices (KARGARZADEH *et al.*, 2017).

4.3.3 Size distribution and morphology of curaua and sugarcane bagasse

Optical microscopy was used to estimate the size distribution of fibers of curaua and sugarcane bagasse before HIUS. Using ImageJ[®], it was possible to measure the length (L) and the diameter (D) of each fiber (Figure 32). Micrographs of these samples are shown in Figure 48 in the Appendix A (p. 105).

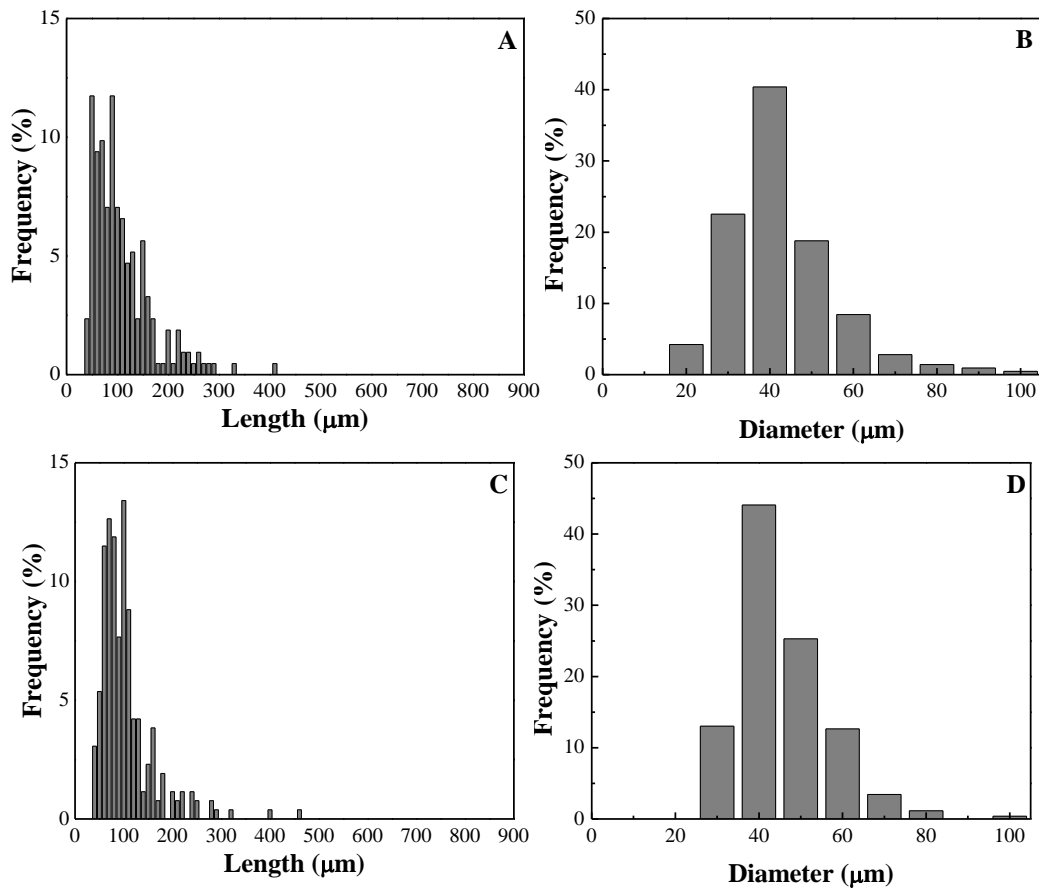


Figure 32 - Distribution histograms of length (A,C) and diameter (B,D) for curaua (C_{raw} (A,B)) and sugarcane bagasse (SCB_{raw} (C,D)) before sonication.

Weight average of each dimension and the aspect ratio (L/D) were calculated (Table 8), according to Eq. 7-8 (p. 24).

Table 8 - Values of weight averages diameter and length and aspect ratio (L/D) for curaua (C_{raw}) and sugarcane bagasse (SCB_{raw}).

Material	L_{average} (μm)	D_{average} (μm)	L/D
C_{raw}	141	47	3.00
SCB_{raw}	135	48	2.81

The values of aspect ratio of samples C_{raw} and SCB_{raw} were similar, both of them were lower than VR_{raw} (L/D of 6.48, p. 56). This difference may be justified for their distinct morphologies. Thus, SEM was carried out for raw curaua and sugarcane. Figure 33 and Figure 34 show SEM micrographs of C_{raw} and SCB_{raw} , respectively.

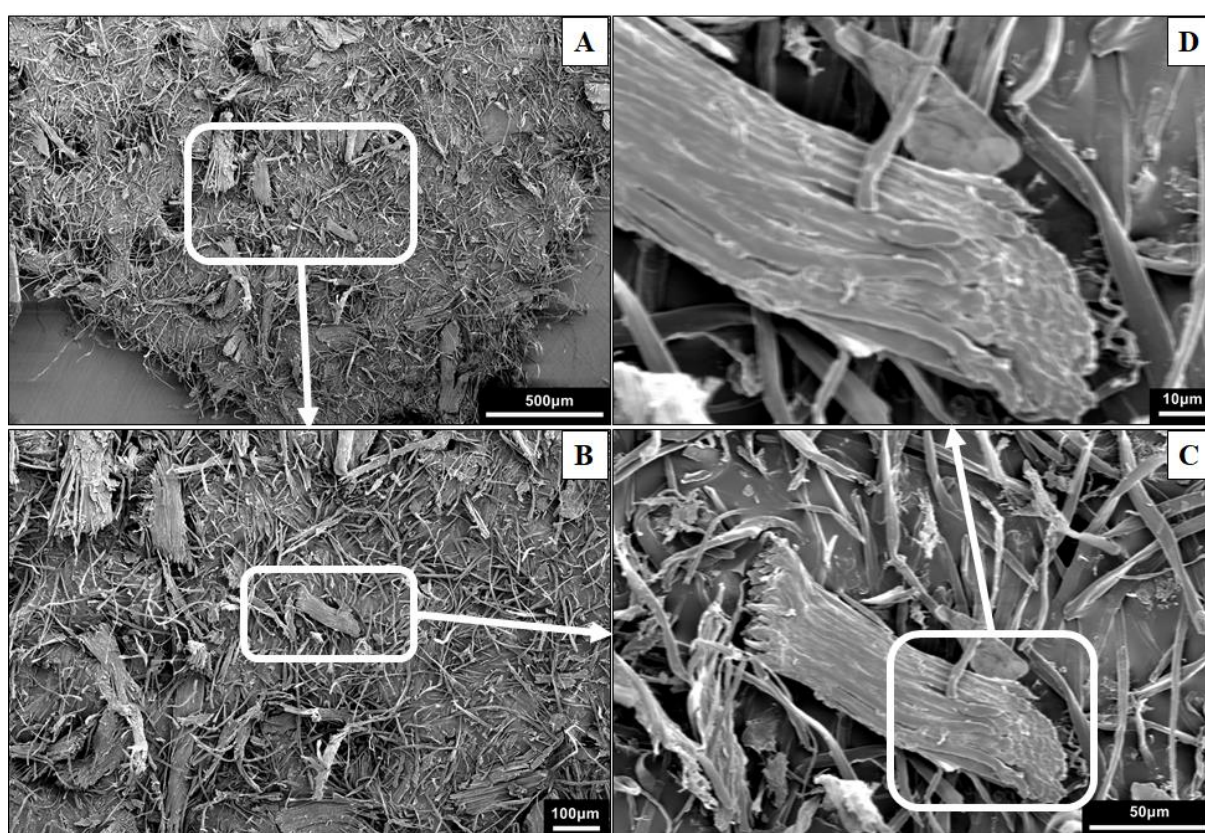


Figure 33 - SEM micrograph of curaua before sonication (C_{raw}) at x50 (A), x100 (B), x500 (C) and x1000 (D).

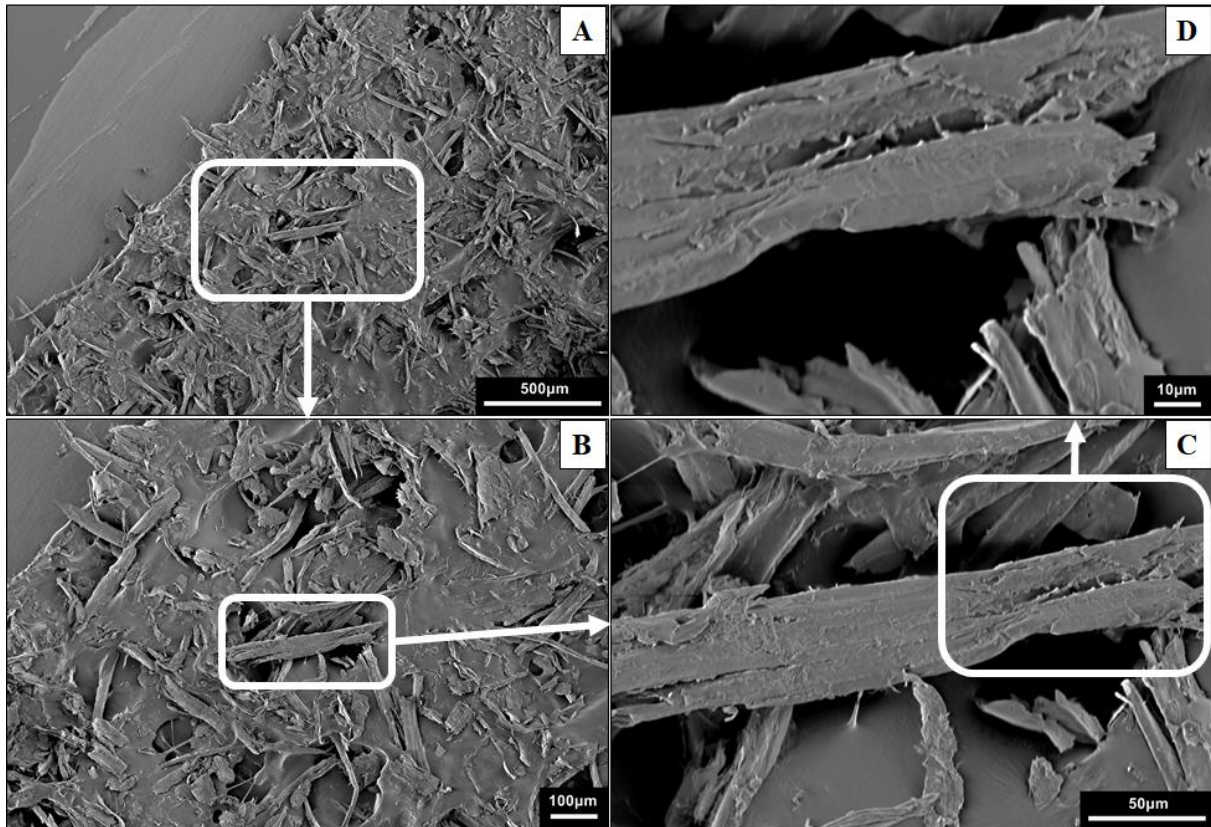


Figure 34 - SEM micrograph of sugarcane bagasse before sonication (SCB_{raw}) at x50 (A), x100 (B), x500 (C) and x1000 (D).

C_{raw} sample showed many individual fibers (Figure 33A and B) as well as bundles of connected fibers (Figure 33C and D). Their surface was smooth, and no fibrillation was detected, as expected (SPINACÉ *et al.*, 2009; MANO *et al.*, 2010). The observed dimensions by SEM were compatible to those obtained by optical microscopy, where the length was from ~30 to 330 μm (Figure 32A, p. 61) and the diameter was from ~20 to 110 μm (Figure 32B, p. 61).

As observed in C_{raw} (Figure 33), sugarcane bagasse SCB_{raw} (Figure 34) exhibited individual fibers and bundles. However, it was not possible to distinguish each fiber in the SCB_{raw} bundles (Figure 34C and D). This could be related to the higher content of lignin in SCB_{raw} , which will be discussed in Section 4.3.3 (p. 31). The dimensions of SCB_{raw} were also comparable to those analyzed by optical microscopy, where the length was from ~40 to 330 μm (Figure 32C, p. 61) and the diameter was around 30 to 100 μm (Figure 32D, p. 61).

It is important to mention that the surface of lignocellulosic fibers can show some non-fibrous components, such as oils (MANDAL and CHAKRABARTY, 2011; MOTAUNG and MOKHOTHU, 2016), but these components were not present in C_{raw} (Figure 33) neither in SCB_{raw} (Figure 34).

In order to confirm the presence of nanocellulose in sonicated samples of curaua and sugarcane bagasse, their suspensions were examined by DLS (Figure 35).

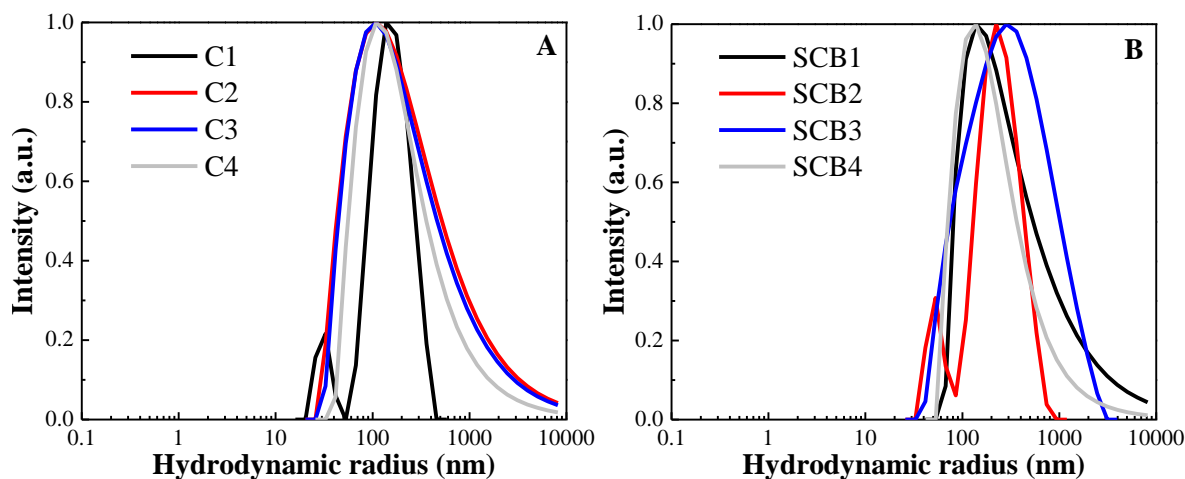


Figure 35 - DLS intensity distribution of sonicated samples of curaua (A) and sugarcane bagasse (B).

DLS results for all samples from curaua and sugarcane bagasse indicated the presence of nanocellulose, as it can be seen in Figure 35, which was also observed for sonicated bacterial cellulose (Figure 25, p. 54) and viscose residue (Figure 29, p. 58).

C1, C3 and C4 presented monomodal distribution while C2 showed a bimodal one (Figure 35A). C2 sample showed two main peaks at 30 and 145 nm and samples C1, C3 and C4 presented only one main peak at ~110 nm. Average peak among all samples was 119 (\pm 18) nm. HIUS conditions didn't appear to have a significant influence on size of particles extracted from curaua.

There are no data available in literature about DLS measurements to nanocellulose extracted from curaua. However, the properties of micrometric fibers of curaua are similar to those of pineapple (SENA NETO *et al.*, 2015). Mahardika *et al.* (2018) obtained nanocellulose from pineapple using high shear homogenization followed by 60 min of HIUS and observed DLS main peak at 55 nm. Balakrishnan *et al.* (2018) applied a sequence of chemical pretreatments and acid hydrolysis in distinct conditions to extract nanocellulose from pineapple, and their DLS analysis showed main peaks at 50, 60, 200 and 1500 nm. Ravindran, Sreekala and Thomas (2019) applied a chemical pretreatment, acid hydrolysis and ball milling for 3 h to extract nanocellulose from pineapple and observed a main DLS peak at 400 nm. In this research, HIUS process in a single step was used to obtain nanocellulose after 45 min (C3 sample) from curaua fiber, which presented similar or smaller DLS peaks than those described in the literature for pineapple.

SCB samples (Figure 35B) exhibited a bimodal distribution for SCB2 and monomodal for SCB1, SCB3 and SCB4. The main peaks for SCB1, SCB3 and SCB4 were 140 nm, 295 and 130 nm, respectively, and for SCB2 they were 50 and 235 nm. Value of average peak among all samples was 200 (\pm 79) nm. Nanocellulose extracted from sugarcane bagasse using a chemical method, acid hydrolysis, resulted in a nanomaterial with monomodal distributions and main peaks at 40 nm (MANDAL and CHAKRABARTY, 2011) or at 250 nm (SOFLA *et al.*, 2016) and bimodal distribution, with peaks at 20 and 200 nm (EL ACHABY *et al.*, 2017). On the other hand, the use of ball milling resulted in a material in nano scale range, with main peak at 300 nm, and also in the micrometer range, with peaks at 4 and 20 μ m (EL ACHABY *et al.*, 2017). In this manner, HIUS allowed an extraction of nanocellulose with similar dimensions to chemical or mechanical techniques, but there was no pretreatment neither a complex sequence of steps to obtain the nanomaterial.

For almost all sonicated samples of curaua and sugarcane bagasse shown in Figure 35, there were micrometer particles present too. They can be agglomerates or residues from the raw materials. In fact, there is an agglomeration tendency because the high specific area of nanocellulose and the intra- and intermolecular hydrogen bonds in cellulose (SOYEKWO *et al.*, 2016). Jakubek *et al.* (2018) even stated that this agglomeration can be reduced but not eliminated. So, SEM was carried out to evaluate these micrometer particles, and samples C3 and SCB3 were chosen due to their high crystallinity index, Table 6 (p. 47). Figure 36 presents SEM micrograph of C3 and SCB3.

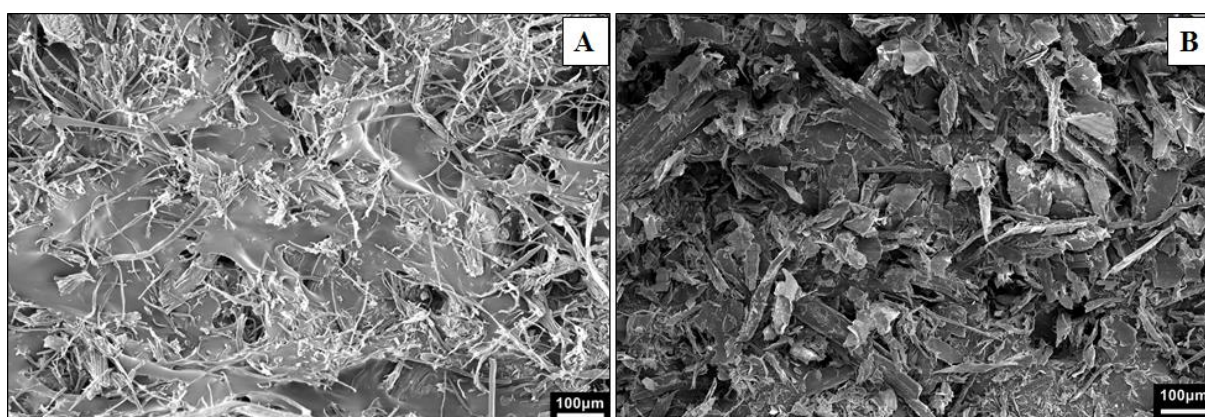


Figure 36 - SEM micrograph at x100 of sonicated: curaua C3 (A) and sugarcane bagasse SCB3 (B).

Figure 36A and B show that C3 and SCB3 samples presented many micrometric particles, similar to C_{raw} (Figure 33, p. 62) and SCB_{raw} (Figure 34, p. 63). Therefore, DLS (Figure 35) and SEM analysis (Figure 36) confirmed the existence of a mixture of particles in micro and nano scales. In the yielding determination, around 11 % of each sample was of

nanocellulose, as pointed out in Section 4.5, p. 77. A mixture of micro and nanofibrils after HIUS was reported to regenerated cellulose too (CHENG, WANG and HAN, 2010), but there is nothing about curaua or sugarcane bagasse in the literature.

TEM was carried out to characterize these nanomaterials (Figure 37) because DLS results may not be related to length or width of nanocellulose (EL ACHABY *et al.*, 2017; YANG *et al.*, 2017; JAKUBEK *et al.*, 2018). Samples C3 and SCB3 were chosen due to their high crystallinity (Table 6, p. 47) and low energy consumption (Figure 45, p. 78). Appendices D (p. 109) and E (p. 111) show more micrographs of samples C3 and SCB3, respectively.

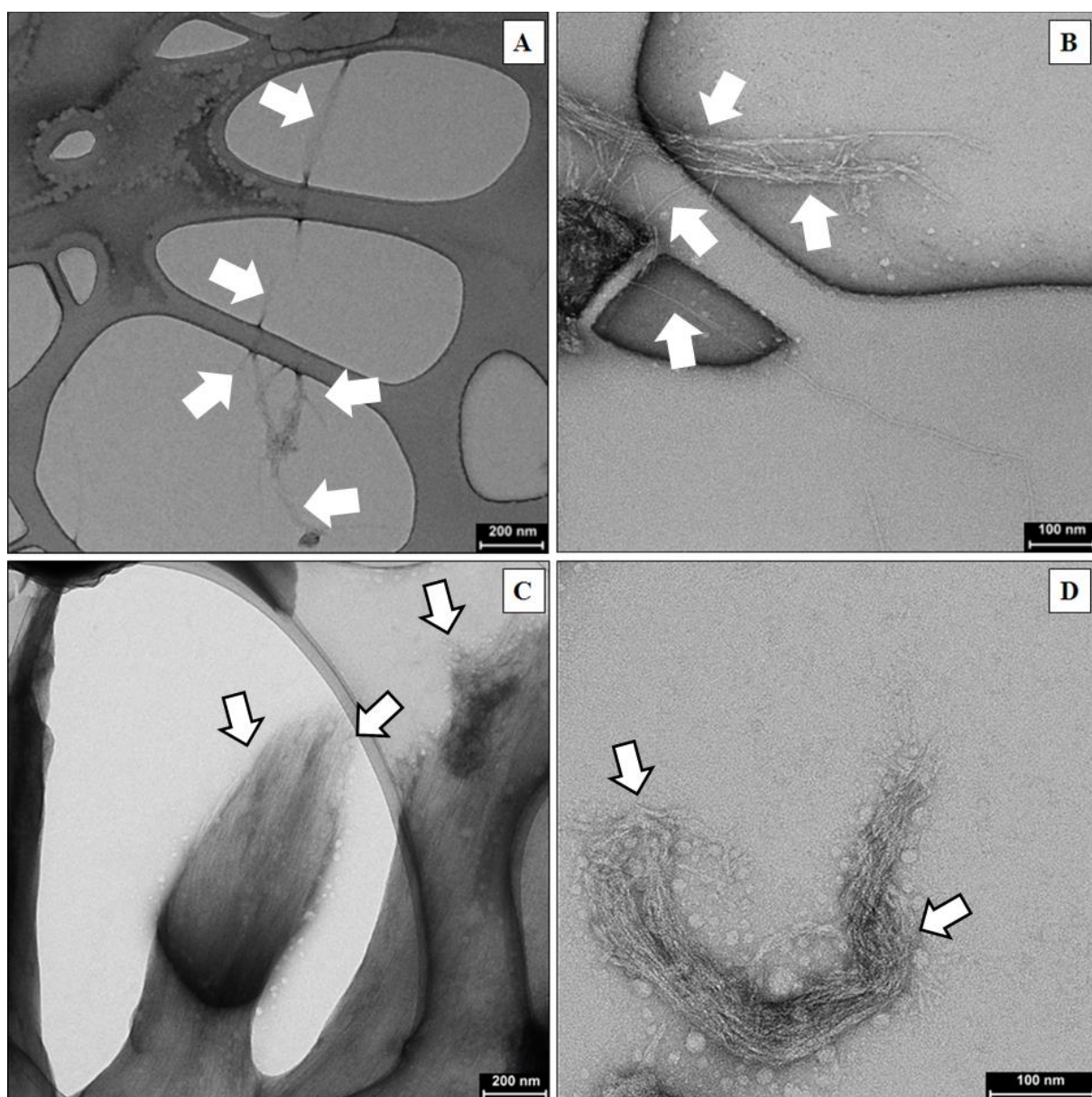


Figure 37 - TEM micrographs of sonicated: curaua C3 (A, B) and sugarcane bagasse SCB3 (C, D).

The presence of cellulose nanofibers (CNF) was verified both from curaua (Figure 37A and B) and sugarcane bagasse (Figure 37C and D), similar what was observed for sonicated viscose (Figure 31, p. 60). Moreover, Figure 37C helps to elucidate the process of extraction of nanocellulose. As discussed about Figure 3 (p. 4), cellulose microfibrils are constituted by several elementary fibrils with nanometric dimension. During the HIUS process, cavitation create water jets which can cause the fibrillation of the microfibrils of cellulose (ZHAO, FENG and GAO, 2007; CHENG, WANG and RIALS, 2009; WANG, LI and ZHANG, 2013; AMIN *et al.*, 2015; SANTUCCI *et al.*, 2016; NACAS *et al.*, 2017).

Campos *et al.* (2013) used a combination of enzymatic hydrolysis and sonication and they obtained CNF from curaua and sugarcane bagasse as well. Gilfillan, Moghaddam and Doherty (2014) extracted CNF from sugarcane bagasse after mechanical shearing. Corrêa *et al.* (2010) and Claro *et al.* (2018, 2019) produced CNF from curaua using acid hydrolysis.

The size distribution (length and diameter) considering all TEM measurements of C3 (curaua) and SCB3 (sugarcane bagasse) are presented in Figure 38.

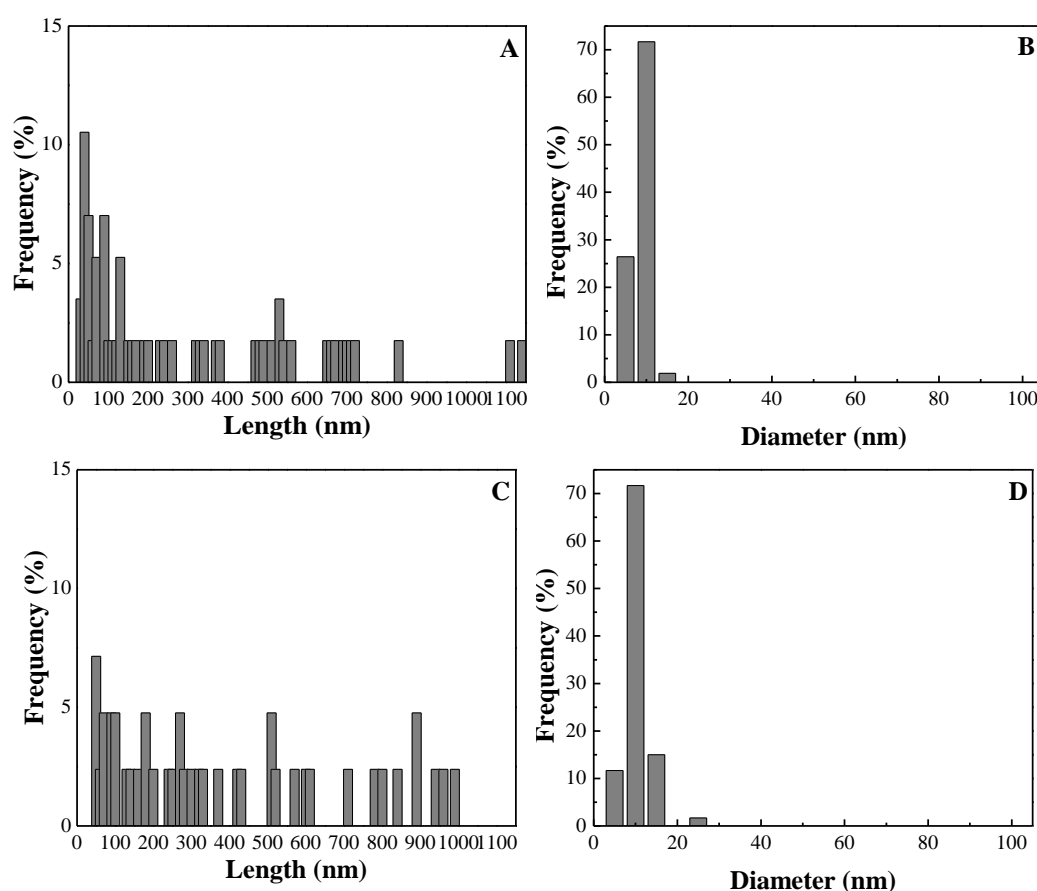


Figure 38 - Distribution histograms of length (A,C) and diameter (B,D) measured using all TEM micrographs for C3 (A,B) and SCB3 (C,D).

The length of C3 and SCB3 were from 30 to 1140 and from 50 to 990 nm while the diameter ranged between 5~15 and 5~25 nm, respectively, Figure 38. The weight averages of length and diameter (Eq. 7, p. 24) of C3 sample were 567 and 9 nm, respectively, resulting in an aspect ratio value of 60. Likewise, weight averages of length and diameter of SCB3 were 615 and 11 nm, respectively, so its aspect ratio was 54.

Campos *et al.* (2013) combined enzymatic hydrolysis with sonication to obtain nanocellulose from these sources. Their smallest diameter was 55 and 30 nm for curaua and sugarcane bagasse, respectively, with average length of 1280 and 255 nm, respectively. Among all their samples, the highest aspect ratios for curaua and sugarcane bagasse were 38 and 41, respectively.

Gilfillan, Moghaddam and Doherty (2014) applied mechanical shearing aiming to extract CNF from sugarcane bagasse, whose average diameter was 26 nm and the aspect ratio was 247.

Corrêa *et al.* (2010) as well as Claro *et al.* (2018, 2019) obtained CNF from curaua by acid hydrolysis. Corrêa *et al.* (2010) observed average length and diameter of 80-170 nm and 6-10 nm, respectively, with an aspect ratio around 13-17. Claro *et al.* (2018) measured only the diameter of CNF from curaua, 36 nm. Claro *et al.* (2019) verified average length and diameter of 400 and 34 nm, respectively, resulting in an aspect ratio of 12.

Aspect ratio of nanocellulose is an important parameter for improve mechanical properties of nanocomposites (MARIANO, EL KISSI and DUFRESNE, 2014; KARGARZADEH *et al.*, 2017). Except for results reported by Gilfillan, Moghaddam and Doherty (2014), samples C3 and SCB3 showed values that were similar or even better than those ones described in the literature.

4.3.4 Comparison of size distribution and morphology among cellulose sources

Turning back to the raw cellulosic materials, Koutsianitis *et al.* (2015) stated that low L/D of the microscopic fibers would favor the extraction of nanostructures using HIUS process. In addition, Wang and Cheng (2009) showed that shorter fibers would favor this process. In this context and based on the results of Sections 4.3.2 (p. 56) and 4.3.3 (p. 61), Figure 39 indicates the average values of length, diameter and L/D of raw curaua (C_{raw}), raw sugarcane bagasse (SCB_{raw}) and raw viscose residue (VR_{raw}). There is no datum about raw bacterial cellulose (BC_{raw}) in Figure 39 because its particles were not fibrous, as discussed about Figure 23 (p. 52).

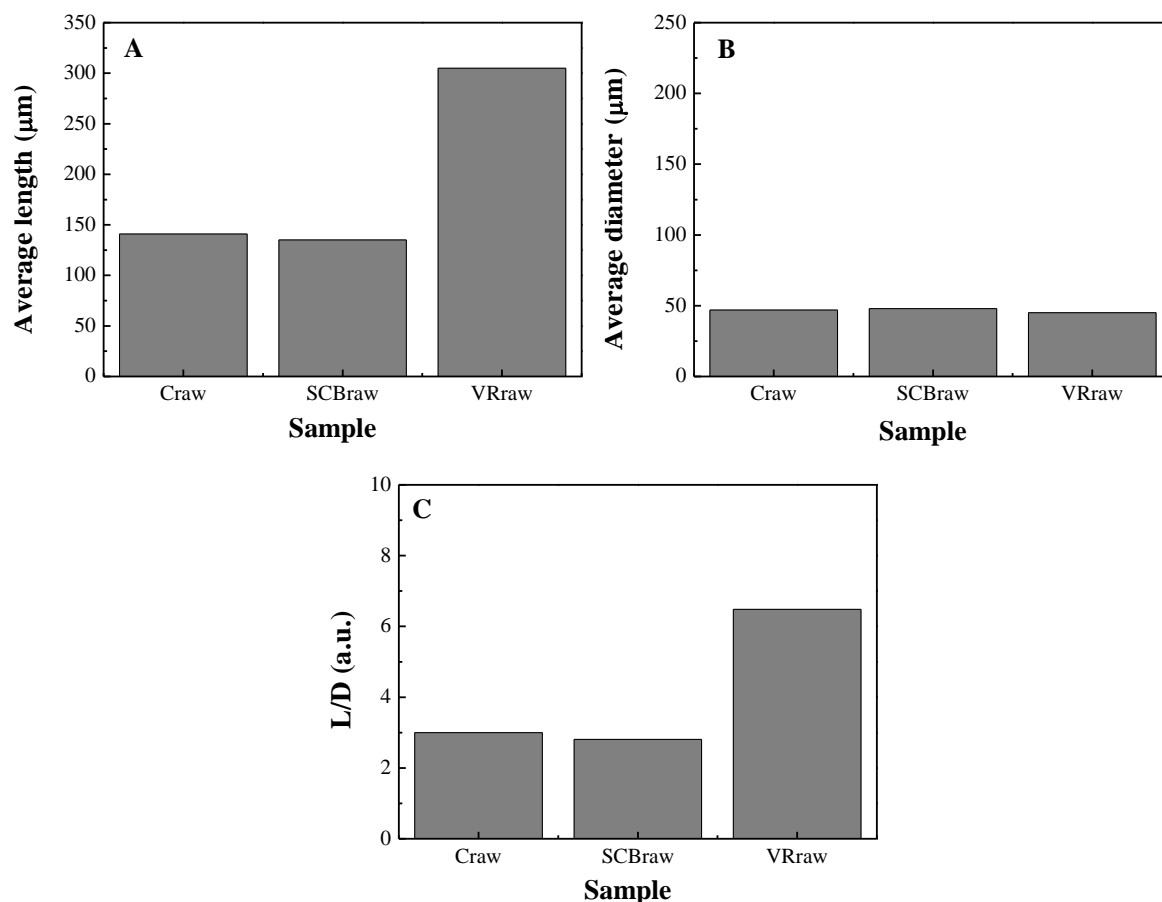


Figure 39 - Average length (A), average diameter (B) and aspect ratio L/D (C) of raw materials: curaua (C_{raw}), sugarcane bagasse (SCB_{raw}) and viscose residue (VR_{raw}).

Based only on the values of the L/D shown in Figure 39, C_{raw} or SCB_{raw} possibly would be most efficient sources to obtain nanocellulose instead of bacterial cellulose or viscose residues. However, comparing these data with the size distribution of sonicated samples and the energy demand of the process (p. 77), it is possible to verify that BC_{raw} and VR_{raw} , which are cellulose sources without hemicellulose and lignin, can provide smaller nanomaterials or consume less energy. In this manner, it is possible to conclude that only the size distribution of the raw materials is not enough to determine the efficiency of extraction using HIUS.

Figure 40 presents the average of the main peaks of hydrodynamic radius observed by DLS for sonicated materials of all cellulose sources, as pointed out in Sections 4.3.1 (p. 51), 4.3.2 (p. 56) and 4.3.3 (p. 61).

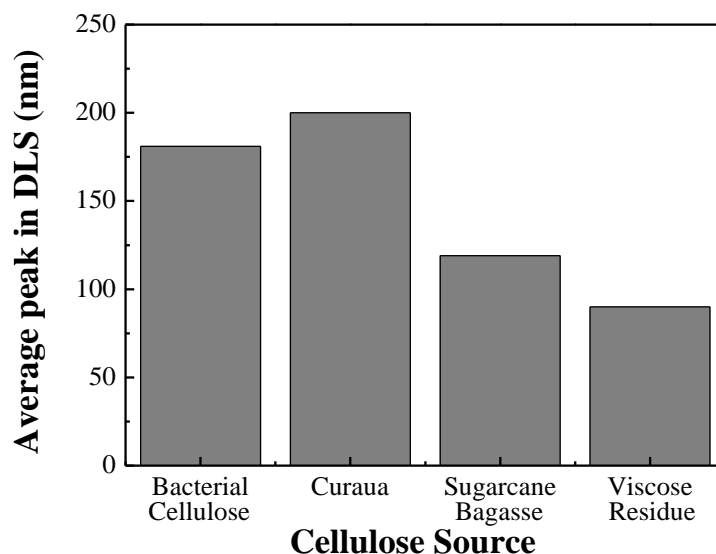


Figure 40 - Average of main peaks of hydrodynamic radius observed in DLS measurements after sonication.

DLS results presented in Figure 40 and in the specific measurements (Figure 25, p. 54; Figure 29, p. 58; Figure 35, p. 64) indicated that it was possible to obtain nanocellulose from all sources used in this research, but there were residues of particles with micrometric size in samples extracted from curaua, sugarcane bagasse and viscose residue.

Grishkewich *et al.* (2017) stated that the type of cellulose source will affect the nanocellulose dimensions. On the other hand, Santucci *et al.* (2016) applied chemical pretreatment, followed by enzymatic hydrolysis and HIUS to sugarcane bagasse, and they published that “regardless of chemical composition and previous refining methods”, the obtained cellulose nanofiber samples “present similar diameters”. The results in this Dissertation demonstrated that the same HIUS conditions lead to the formation of nanocellulose with distinct sizes according to DLS results together with those of morphology from AFM and TEM measurements.

4.4 Thermal degradation of cellulose before and after sonication process

4.4.1 Thermal degradation of bacterial cellulose

Understanding the thermal stability of cellulose is crucial in the field of composites and nanocomposites. According to the temperature where the degradation begins, it is possible to know beforehand if the nanomaterial will degrade during the processing with the polymeric matrix, what would lead to a reduction in the reinforcement (POLETTTO *et al.*, 2012).

In this manner, the thermogravimetry of all samples from bacterial cellulose before (BC_{raw}) and after HIUS (BC1, BC2, BC3 and BC4) are shown in Figure 41.

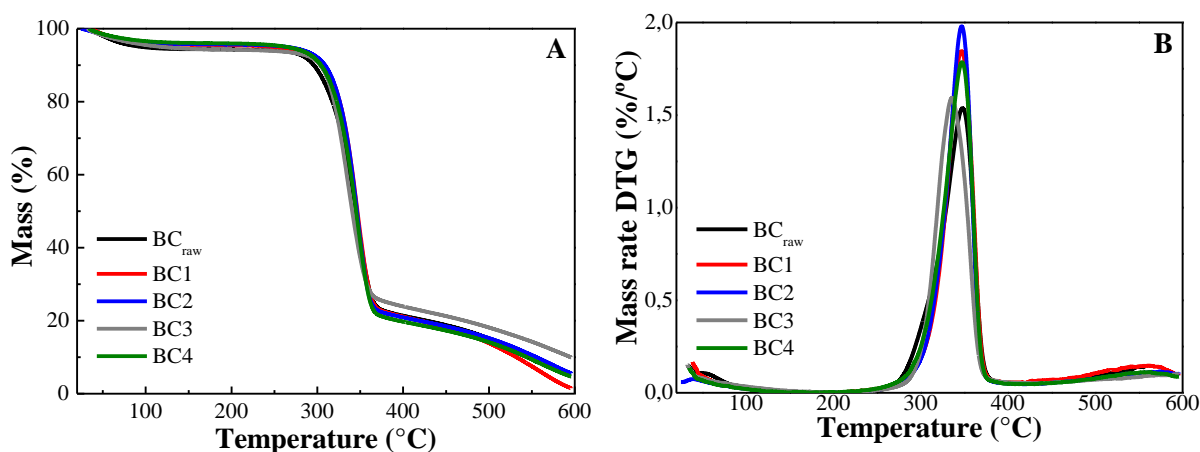


Figure 41 - TGA (A) and DTG (B) of bacterial cellulose before (BC_{raw}) and after sonication (BC1, BC2, BC3 and BC4).

All samples (BC_{raw} , BC1, BC2, BC3 and BC4) presented an initial mass loss up to 100 °C, Figure 41. In their FTIR spectra (Figure 11, p. 28), there was a band at $\sim 1630\text{ cm}^{-1}$, characteristic of absorbed water molecules (ÖZGENÇ *et al.*, 2017; BALAKRISHNAN *et al.*, 2017). Therefore, this mass loss can be related to the evaporation of this water, as expected (ROMAN and WINTER, 2004; YANG *et al.*, 2007; SPINACÉ *et al.*, 2009; WONG, KASAPIS and TAN, 2009; MANDAL and CHAKRABARTY, 2011; ROJO *et al.*, 2013; YANG *et al.*, 2017).

The behavior of all samples was similar above 100 °C, with a main narrow peak in DTG (Figure 41B). Results of TGA analysis are indicated in Table 9.

Table 9 - TGA results of bacterial cellulose before (BC_{raw}) and after sonication (BC1, BC2, BC3 and BC4).

Sample	T_{onset} (°C)	T_{endset} (°C)	$T_{\text{max-loss}}$ (°C)	SR ₅₀₀ (%)
BC_{raw}	277	376	348	18
BC1	284	374	347	12
BC2	275	373	348	14
BC3	283	373	337	17
BC4	264	379	348	13

In Table 9, T_{onset} and T_{endset} are the temperature which degradation starts and finishes, respectively. $T_{\text{max-loss}}$ is the temperature with the maximum mass loss rate while SR_{500} is the solid residue at 500 °C.

This process of degradation indicated in Figure 41 is basically related to cellulose pyrolysis (ROMAN and WINTER, 2004; YANG *et al.*, 2007; SPINACÉ *et al.*, 2009; WONG, KASAPIS and TAN, 2009; TISCHER *et al.*, 2010; ROJO *et al.*, 2013). The thermal degradation of pure cellulose generally occurs between 315 and 400 °C (YANG *et al.*, 2007), but there are reports for bacterial cellulose starting even at 208 °C (TISCHER *et al.*, 2010), 220 °C (CAI and KIM, 2010; KUMAR *et al.*, 2019) and 250 °C (ROMAN and WINTER, 2004; VASCONCELOS *et al.*, 2017). Pa'e *et al.* (2018) stated that the thermal stabilities of different samples of bacterial cellulose can be distinct because this property depends not only of chemical composition or crystallinity, but also of the method of fermentation and the used medium during the production of this material. The main mechanisms during cellulose degradation include the depolymerization of its chains, the dehydration, the cleavage of secondary bonds and the formation of a charred residue (ROMAN and WINTER, 2004; YANG *et al.*, 2007; SPINACÉ *et al.*, 2009; WONG, KASAPIS and TAN, 2009).

The onset temperature of decomposition (T_{onset}) of all sonicated samples was similar to BC_{raw} (277 °C) while the average value of T_{onset} for all sonicated samples was 277 (± 9) °C. However, comparing the sonicated samples among themselves, it was verified that longer sonication times (BC2 and BC4, 70 min) resulted in lower thermal stability than the shorter ones (BC1 and BC3, 45 min), with a reduction of 10~20 °C. The variation of mass loading did not affect this property.

Similar profiles of TGA and DTG curves before and after HIUS were observed. Tischer *et al.* (2010) also verified this behavior for sonicated bacterial cellulose in relation to its raw material. This similarity before and after HIUS process was expected because no chemical modification in FTIR spectra was verified (Figure 11, p. 28).

4.4.2 Thermal degradation of viscose residue

TGA and DTG curves for viscose samples before (VR_{raw}) and after HIUS (VR1, VR2, VR3 and VR4) are demonstrated in Figure 42.

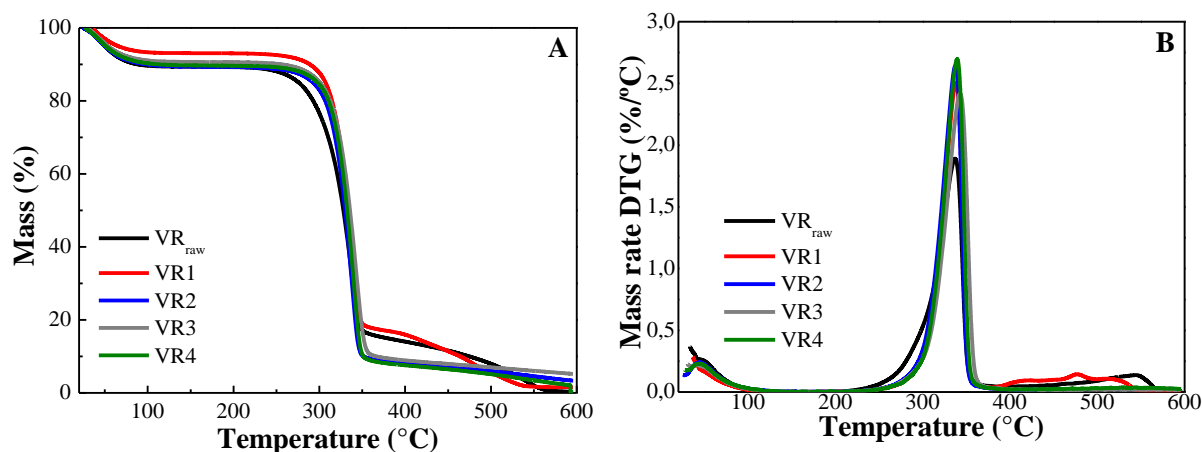


Figure 42 - TGA (A) and DTG (B) of viscose residues before (VR_{raw}) and after sonication (VR1, VR2, VR3 and VR4).

The initial mass loss up to 100 °C was due to absorbed water evaporation, as in bacterial cellulose samples (Figure 41, p. 71). After that, there was only one peak in DTG (Figure 42B), attributed to cellulose degradation. Results of TGA analysis are shown in Table 10, where T_{onset} and T_{endset} are the temperature which degradation starts and finishes, respectively. $T_{\text{max-loss}}$ is the temperature with the maximum mass loss rate while SR_{500} is the solid residue at 500 °C.

Table 10 - TGA results of viscose residues before (VR_{raw}) and after sonication (VR1, VR2, VR3 and VR4).

Sample	T_{onset} (°C)	T_{endset} (°C)	$T_{\text{max-loss}}$ (°C)	SR_{500} (%)
VR _{raw}	253	358	336	9
VR1	285	356	339	5
VR2	275	353	338	5
VR3	276	361	343	7
VR4	279	356	340	5

T_{onset} value for VR_{raw} was 253 °C, Table 10. Carrillo *et al.* (2004), Rojo *et al.* (2013) and Li *et al.* (2019) verified the thermal degradation of viscose started around 250 °C as well.

All samples presented values of ~20 °C higher than the raw material VR_{raw}, Table 10. Average T_{onset} of all sonicated samples was 279 (± 5) °C. However, comparing sonicated samples among themselves, there is no significant trend regarding the influence of mass loading or sonication time in the beginning of thermal degradation.

The general enhancement in thermal stability possibly is related to the higher CI of the sonicated samples (VR1, VR2, VR3, VR4 - Table 5, p. 44), as suggested in the literature

about cellulose and nanocellulose (CIOLACU and POPA, 2006; WANG, DING and CHENG, 2007; TISCHER et al., 2010; POLETO et al., 2012; MATTONAI *et al.*, 2018).

4.4.3 Thermal degradation of curaua and sugarcane bagasse

The thermal analyses of curaua and sugarcane bagasse samples before and after HIUS are demonstrated in Figure 43 A,B and C,D, respectively.

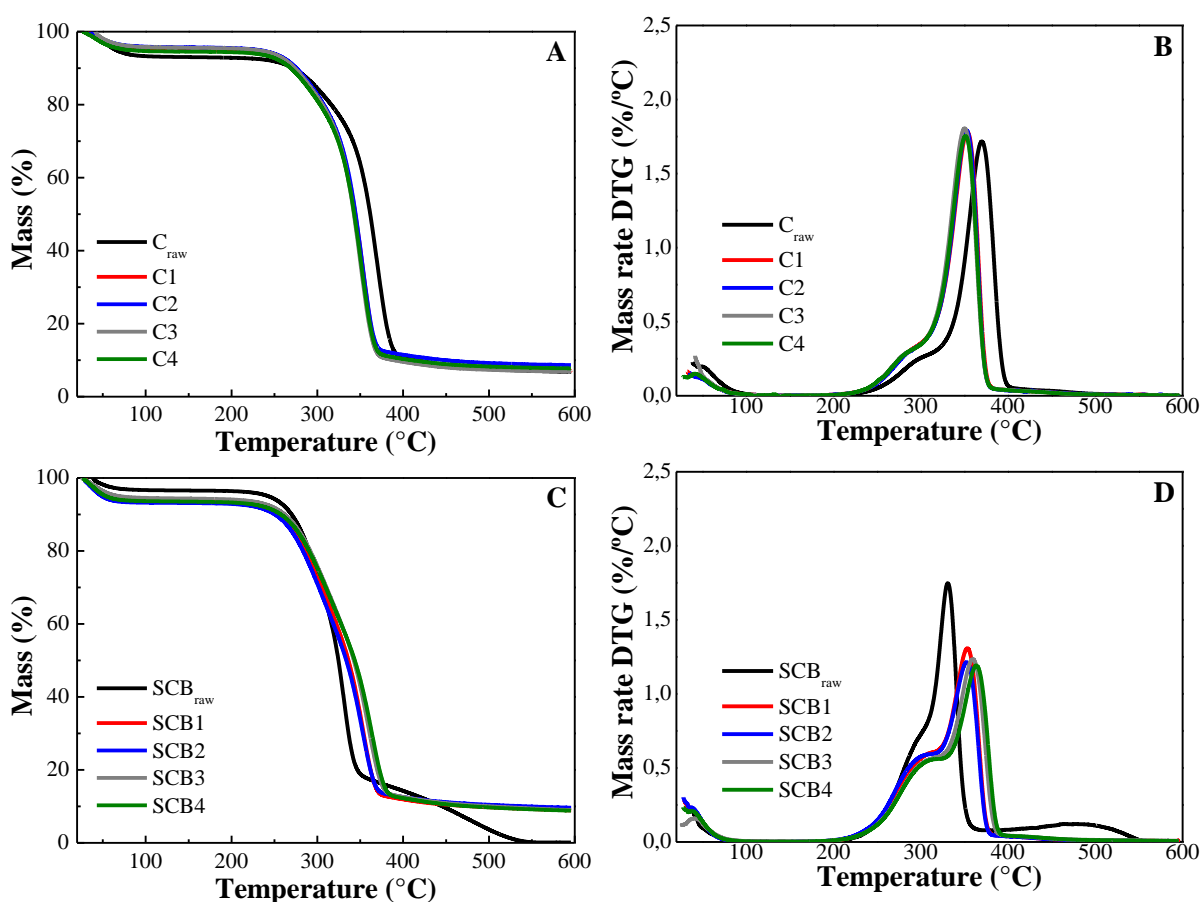


Figure 43 - TGA (A,C) and DTG (B,D) of: (A,B) curaua before (C_{raw}) and after sonication (C1, C2, C3 and C4); and (C,D) sugarcane bagasse before (SCB_{raw}) and after sonication (SCB1, SCB2, SCB3 and SCB4).

All samples showed a similar behavior (Figure 43). The first mass loss up to 100 °C happened because the evaporation of the absorbed water, like samples of bacterial cellulose (Figure 41, p. 71) and viscose residue (Figure 42, p. 73).

Then, there were other two events of degradation. DTG profiles of curaua and sugarcane bagasse (Figure 43) were alike, with a broad shoulder followed by a narrow peak. Results of TGA analysis are shown in Table 11.

Table 11 - TGA results of curaua and before (C_{raw}) and after sonication (C1, C2, C3 and C4) and of sugarcane bagasse before (SCB_{raw}) and after sonication (SCB1, SCB2, SCB3 and SCB4).

Sample	$T_{\text{onset-1}}$ (°C)	$T_{\text{max-loss-1}}$ (°C)	$T_{\text{onset-2}}$ (°C)	$T_{\text{max-loss-2}}$ (°C)	T_{endset} (°C)	SR ₅₀₀ (%)
C_{raw}	237	282	320	357	383	6
C1	222	289	304	354	378	7
C2	224	289	306	353	378	9
C3	228	283	305	351	377	7
C4	229	285	305	351	378	8
SCB_{raw}	244	292	313	330	350	3
SCB1	239	302	326	354	377	9
SCB2	229	302	324	353	377	10
SCB3	236	313	330	359	386	9
SCB4	236	310	333	364	389	9

The first process of degradation of curaua and sugarcane bagasse (Figure 43) was due to hemicellulose (YANG *et al.*, 2007; SPINACÉ *et al.*, 2009). Usually, the thermal decomposition of hemicelluloses happens at 220-315 °C (YANG *et al.*, 2007; TONOLI *et al.*, 2012). It takes place because amorphous structure of hemicellulose presents many branches, what favors its degradation (YANG *et al.*, 2007). This justifies why the thermal stabilities of C_{raw} and SCB_{raw} were lower than raw bacterial cellulose (BC_{raw} in Figure 41, p. 71) and viscose residue (VR_{raw} in Figure 42, p. 73).

The second process (narrow peak) is basically related to cellulose pyrolysis (ROMAN and WINTER, 2004; YANG *et al.*, 2007; SPINACÉ *et al.*, 2009; WONG, KASAPIS and TAN, 2009; TISCHER *et al.*, 2010; ROJO *et al.*, 2013). The thermal degradation of pure cellulose generally occurs between 315 and 400 °C (YANG *et al.*, 2007). The main mechanisms during its degradation include depolymerization, dehydration, cleavage of secondary bonds and formation of charred residue (ROMAN and WINTER, 2004; YANG *et al.*, 2007; SPINACÉ *et al.*, 2009; WONG, KASAPIS and TAN, 2009).

Another detail that cannot be ignored is the presence of lignin in curaua and sugarcane bagasse. It is not clear in Figure 43 possibly because lignin thermal decomposition occurs slowly from room temperature even to 900 °C, with a mass loss rate lower than hemicellulose and cellulose (YANG *et al.*, 2007; TONOLI *et al.*, 2012). Besides dehydration and formation of char, heating lignin may produce water, CO₂, CO and methane (YANG *et al.*, 2007; SPINACÉ *et al.*, 2009).

Looking to the properties of the raw fibers (C_{raw} and SCB_{raw}), the temperature of beginning of degradation was lower for all sonicated samples. T_{onset} of C_{raw} was 237 °C while the average T_{onset} of sonicated samples from curaua was 226 ± 3 °C. Likewise, T_{onset} of SCB_{raw} was 244 °C and the average T_{onset} of sonicated samples from sugarcane bagasse was 235 ± 4 °C. Yang *et al.* (2017) suggested that if cellulose chains were damaged during the process to extract nanocellulose, these low molecular segments would degrade first and reduce thermal stability. This can be assumed to occur with hemicellulose too, once this component is present not only in the raw fibers, but also in their nanocellulose, as proved by AFM-IR analyses (curaua: Figure 15, p. 35, sugarcane bagasse: Figure 16, p. 37). It was not observed any trend about the influence of sonication time in the beginning of thermal degradation of samples from curaua or sugarcane bagasse.

4.4.4 Comparison of thermal degradation among cellulose sources

The values of T_{onset} as a function of raw materials and sonicated samples in different conditions of mass loading (0.1 or 0.2 g) and sonication time (45 or 70 min) are shown in Figure 44.

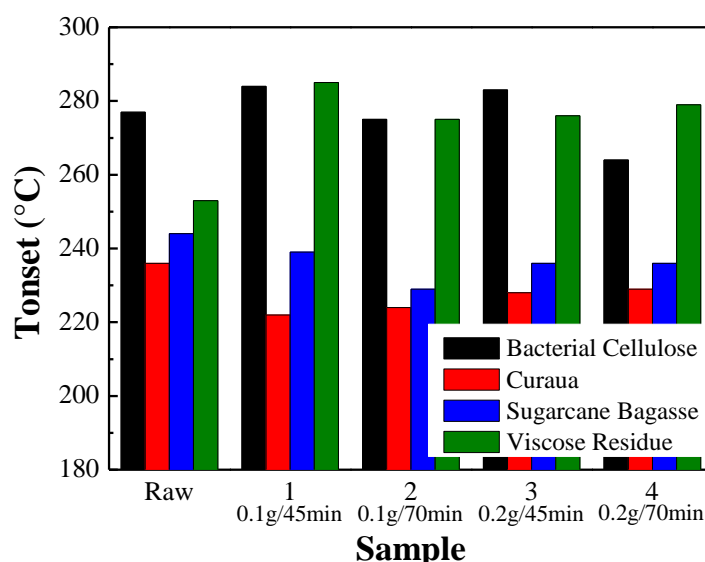


Figure 44 - Values of T_{onset} as a function of raw and sonicated samples.

Abral *et al.* (2018) studied the thermal degradation of nanocellulose produced using HIUS and they verified that smaller nanocellulose started to decompose sooner. This trend was observed in the results of Figure 44 as well. Size distribution of nanocellulose was analyzed in Section 4.3, especially for the condition 3 (0.2 g / 45 min). The average diameters

of bacterial cellulose BC3 (Figure 26, p. 55), viscose residue VR3 (Figure 31, p. 60), sugarcane bagasse SCB3 and curaua C3 (Figure 38, p. 67) were 80, 15, 11 and 9 nm, respectively. The smallest samples showed the smallest thermal stability as it can be seen in Figure 44.

Moreover, the influence of chemical composition in the thermal properties is noticed. Samples with hemicellulose and lignin (curaua and sugarcane bagasse, Figure 44) showed lower T_{onset} .

All sonicated samples from viscose residues showed higher T_{onset} than the raw material. The opposite behavior happened to lignocellulosic sources (curaua and sugarcane bagasse), where sonication decreased the thermal stability.

4.5 Yielding and energy demand of HIUS process to extract nanocellulose

Evaluating the efficiency of a process that aims to extract nanocellulose is crucial because it should allow the industrialization of this nanomaterial (NECHYPORCHUK, BELGACEM & BRAS, 2016). Based on that, the yielding and energy consumption were determined for all samples.

The average yielding of nanocellulose per sonication for samples from curaua, sugarcane bagasse and viscose residue was 11 (± 1) %. This parameter could not be determined for bacterial cellulose once all membrane parts had become a gel-like suspension. In this manner, the yielding for sonication of bacterial cellulose could be considered around 100 %. Li and Renneckar (2011) extracted nanocellulose from wood fibers using HIUS and calculated yielding ranging from 12 to 87 %. However, they used chemical pretreatments before HIUS and with more steps in the process, the yielding was higher. Here, the whole process has basically one step with no chemical pretreatment and no pollutant residue.

Compared to chemical processes, many acid hydrolysis procedures yield a maximum of 20~30% of nanocellulose, compared to the initial raw mass (YAHYA *et al.*, 2019). Yahya *et al.* (2019) reported a yielding of 81 % using hydrolysis as well. However, they needed at least 11,5 h of pretreatments for each sample and used several solutions of chemical reagents, such as toluene, ethanol, sodium hydroxide, hydrogen peroxide. The chemical procedure to obtain nanocellulose was relatively quick (20~100 min), but then it was necessary to carry out a dialysis process for 5 days. In this manner, some chemical methods can show a higher yielding, but they need many complex steps while the method in this dissertation (HIUS) was simpler and much faster.

The energy demand for extracting nanocellulose was estimated using Eq. 5 (p. 20), Figure 45.

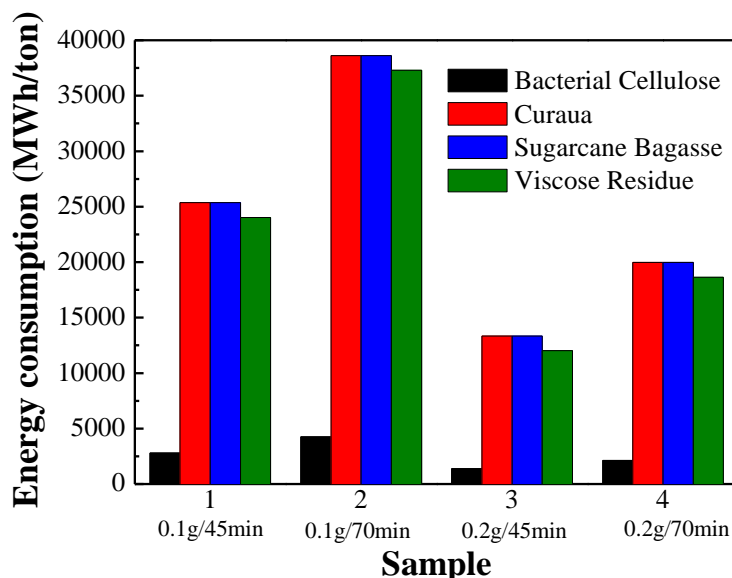


Figure 45 - Energy consumption for extracting nanocellulose as a function of cellulosic material and sonication condition.

The condition with the lowest energy demand (1396 MWh/ton) among all samples shown in Figure 45 was BC3, which used 0.2 g of bacterial cellulose during 45 min of HIUS. On the other hand, C2 and SCB2 showed the highest energy levels (38621 MWh/ton). The values for nanocellulose from viscose residues (VR from 12015 to 37288 MWh/ton) are lower than from curaua (C from 13348 to 38621 MWh/ton) or sugarcane bagasse (SCB from 13348 to 38621 MWh/ton) because VR did not used a hot bath to the raw material as the others (as described in Section 3.2, p. 20).

Wong, Kasapis and Tan (2009) as well as Wardhono, Kanani and Alfirano (2019) stated that HIUS could demand less energy than other mechanical methods, but they did not calculate it. Frone *et al.* (2011) extracted nanocellulose from microcrystalline cellulose using only HIUS for 10-20 min, consuming 330-1333 MWh/ton. Some years later, Ewulonu *et al.* (2019) applied ball milling and acid hydrolysis followed by HIUS for 2 h to sunflower stalks, reaching 820 MWh/ton. All these values are much lower than those shown in Figure 45. However, it is necessary to mention that Frone *et al.* (2011) and Ewulonu *et al.* (2019) sonicated suspensions with concentrations of 0.2 and 0.3 %wt, respectively, while here the concentrations were 0.06 or 0.13 %wt. So, an increase of one order of magnitude of concentration, changing 0.1 to 1.0g and 0.2 to 2.0g, would reduce ~90 % of the energy

necessary to extract nanocellulose from BC and VR or ~81 % from C or SCB. This increasing in mass loading could present energy consumption for BC3 of only 140 MWh/ton, which would be the lowest value in all literature of nanocellulose using HIUS.

However, it must be noticed that higher enhancement in mass concentration in HIUS would be necessary in order to compete with order mechanical methods, like high pressure homogenization (HPH) and extrusion. For instance, nanocellulose obtained using HPH consumed 70 MWh/ton (ERIKSEN, SYVERUD and GREGERSEN, 2008; NECHYPORCHUK, BELGACEM & BRAS, 2016). On the other hand, Lu et al. (2018) while used twin-screw extrusion and recorded 0.06 MWh/ton, but they combined it treatment with colloidal mill for mechanical refining and they didn't consider milling in the energy consumption.

Thereby, a new condition was studied, considering 2 g of bacterial cellulose during 45 min (BC3-M), Figure 46.

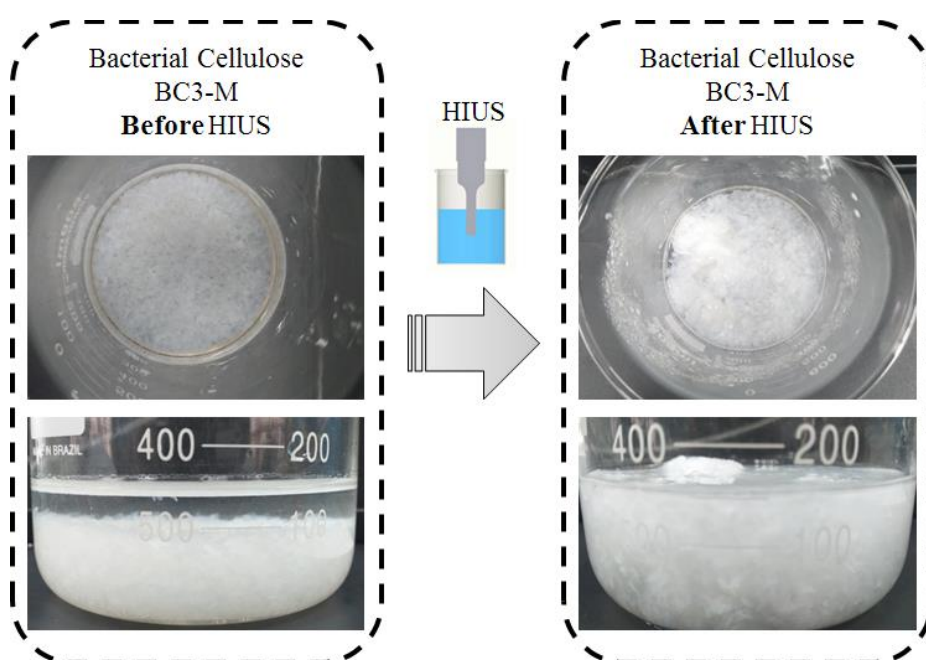


Figure 46 - Sample of bacterial cellulose BC3-M before and after application of HIUS.

Similar to what happen to BC3, sample BC3-M (Figure 46) showed a gel like suspension, with no visible raw membrane residues.

BC3-M was characterized in order to compare if the increasing of mass loading would change the properties of nanocellulose. Crystallinity index of BC3-M was $90.7 (\pm 1.5) \%$, this value is comparable to BC_{raw} ($92.9 (\pm 0.7) \%$) and sonicated condition BC3 ($91.8 (\pm 1.0) \%$), Table 4 (p. 40). In this manner, this value would provide a mechanical reinforcement in

polymeric nanocomposites as good as BC3 but consuming less energy since BC3-M demanded only 140 MWh/ton and BC3 needed 1396 MWh/ton.

This value of energy consumption is interesting for studies about application in large scale. In São Paulo State, the energy company Enel reported that in 2020, the tariff would be of 0,25588 R\$/kWh for the generation of electricity and 0,2571 R\$/kWh for the use of the distribution system (ENEL, 2020). If we consider the total cost of R\$ 0,51559 / kWh in São Paulo State, so BC3-M would require R\$ 71,98/kg (~U\$ 17,99/kg). It is still more expensive than cellulose fibers in microscale for commercial grade (~2,8 R\$/kg – CEPEA, 2019) or for research grade (~40 R\$/kg – SYNTH, 2019) . Notwithstanding, BC3-M is much cheaper than available nanocellulose that is sold at least by ~200 R\$/kg (supplied by CelluForce), but it can achieve even 220,000 R\$/kg (supplied by Cellulose Lab), as discussed about nanocellulose suppliers in Section 1.3.2 (p. 14).

Measurements of DLS and TGA of the BC3-M sample were carried out and are shown in Figure 47A.

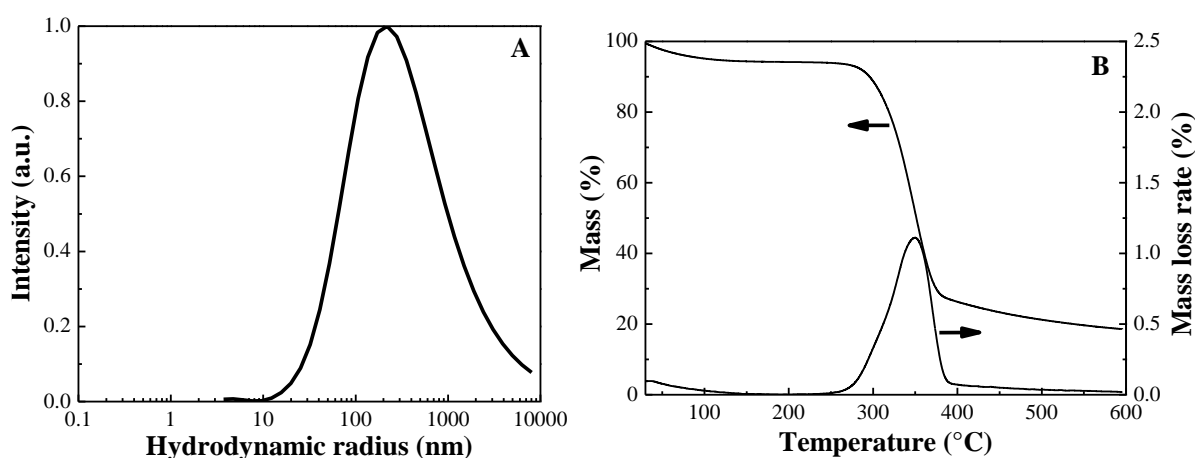


Figure 47 - DLS intensity distribution (A) and TGA and DTG curves (B) of sonicated bacterial cellulose with the highest mass BC3-M (2 g / 45 min).

The presence of particles in the nano scale suggests that the membrane structure was dismantled as happened to other samples of sonicated bacterial cellulose (BC1, BC2, BC3 and BC4). Distribution in Figure 47A was monomodal, with main peak at 219 nm. Main peaks of sonicated bacterial cellulose samples in Section 4.3.1 (Figure 25, p. 54) ranged between 135 and 215 nm. Despite of higher peak in BC3-M (indicating higher nanomaterials), this value is still lower than those observed for nanocellulose from bacterial cellulose using acid hydrolysis, whose peaks were 365~455 nm (WU *et al.*, 2018).

Thermal degradation events of BC3-M sample occurred from 273 to 385 °C, with maximum mass loss rate at 349 °C and 20 % of solid residue at 500 °C, Figure 47B. Its T_{onset} (273 °C) was lower than BC_{raw} (277 °C) and BC3 (283 °C), but it is still higher than all sonicated samples from sugarcane bagasse and curaua (Table 11, p. 75).

Moreover, T_{onset} of BC3-M (273 °C) guarantee that it would not degrade during processing with usual polymeric matrices in the area of composites and nanocomposites, such as high density polyethylene, whose melting temperature (T_m) is ~140 °C (ESSABIR *et al.*, 2016), polypropylene, whose T_m is ~165 °C (JANG, KIM and PARK, 2019), polyamide 6, whose T_m is ~220 °C (MAJKA, COKOT and PIELICHOWSKI, 2018), and polyethylene terephthalate, whose T_m is ~245 °C (ARAUJO and MORALES, 2018).

5 CONCLUSION

Four different cellulose sources, bacterial cellulose, curaua, sugarcane bagasse and viscose residue, were used to extract nanocellulose. This extraction was carried out using high intensity ultrasound (HIUS) with only deionized water, in four distinct conditions (changing mass loading, 0.1 to 0.2 g, and time, 45 to 70 min).

HIUS allowed the production of nanocellulose from all samples, maintaining or even increasing the crystallinity index in relation to the raw materials. This was confirmed by the analyses of DLS, AFM and TEM results. The highest enhancement in crystallinity index happened to nanocellulose from curaua, where the crystallinity index increased from 87.7 to 93.8 %. This is interesting for applications in reinforcement of polymeric nanocomposites.

However, there was a mixture of particles in micro and nano scales as verified by SEM analyses, except for samples from bacterial cellulose. The nanomaterials were mainly cellulose nanofibers, with dimensions comparable to nanocellulose extracted using chemical treatments, as acid hydrolysis.

Chemical structure of all materials did not change with HIUS application. In addition, results of FTIR and AFM-IR indicated that even the nanoscale particles from curaua and sugarcane bagasse showed the chemical groups of hemicellulose and lignin, which were present in their raw materials as well. This is interesting especially for the production of nanocomposites with hydrophobic polymer matrices (*e.g.* polyethylene, polypropylene or polystyrene), where hemicellulose and lignin could avoid the coalescence of nanocellulose and even improve their dispersion, increasing the mechanical properties of the nanocomposite.

Thermogravimetric properties of extracted nanocellulose demonstrated to be dependent of cellulose source, crystallinity and dimensions of the nanomaterial. Higher thermal stability could be achieved with pure cellulose source (such as bacterial cellulose), with high crystallinity index and larger nanomaterials.

At last, a new condition of sonication was carried out based aiming to reduce the energy consumption of HIUS process. This sample was produced using only 2 g of bacterial cellulose during 45 min in deionized water. This nanocellulose showed the lowest energy demand in the literature of nanocellulose using HIUS (140 MWh/ton). It would require less than 18 U\$/kg (~72 R\$/kg) of cost of production, while imported nanocellulose cost at least 50 U\$/kg (~200 R\$/kg). Moreover, it was still observed a high crystallinity degree (~90 %) as well as a high thermal stability (273 °C).

Therefore, HIUS process is a green environment friendly technique that showed potential to produce nanocellulose that could be applied, for example, in reinforcement of thermoplastic polymers. However, more studies are necessary in order to optimize the process and consume less energy, looking for a reduction of costs of this nanomaterial and to make it more accessible to the market.

6 REFERENCES

- ABRAL, H.; LAWRENSIUS, V.; HANDAYANI, D.; SUGIARTI, E. Preparation of nano-sized particles from bacterial cellulose using ultrasonication and their characterization. **Carbohydrate Polymers**, v. 191, p. 161-167, 2018.
- ADAK, B.; MUKHOPADHYAY, S. Effect of pressure on structure and properties of lyocell fabric-based all-cellulose composite laminates. **The Journal of the Textile Institute**, v. 108, p. 1010-1017, 2016.
- AMIN, K.N.M.; ANNAMALAI, P.K.; MORROW, I.C.; MARTIN, D. Production of cellulose nanocrystals *via* a scalable mechanical method. **RSC Advances**, v. 5, p. 57133-57140, 2015.
- ÅKERHOLM, M.; HINTERSTOISSER, B.; SALMÉN, L. Characterization of the crystalline structure of cellulose using static and dynamic FT-IR spectroscopy. **Carbohydrate Research**, v. 339, p. 569-578, 2004.
- ALBARELLI, J.; PAIDOSH, A.; SANTOS, D.; MARECHAL, F.; MEIRELES, M. Environmental, energetic and economic evaluation of implementing a supercritical fluid-based nanocellulose production process in a sugarcane biorefinery. **Chemical Engineering Transactions**, v. 47, p. 49-54, 2016.
- ARAÚJO JR, A.M.; BRAIDO, G.; SASKA, S.; BARUD, H.S.; FRANCHI, L.P.; ASSUNÇÃO, R.M.N.; SCAREL-CAMINAGA, R.M.; CAPOTE, T.S.O.; MESSADDEQ, Y.; RIBEIRO, S.J.L. Regenerated cellulose scaffolds: preparation, characterization and toxicological evaluation. **Carbohydrate Polymers**, v. 136, p. 892-898, 2016.
- ARAUJO, L.M.G.; MORALES, A.R. Compatibilization of recycled polypropylene and recycled poly (ethylene terephthalate) blends with SEBS-g-MA. **Polímeros**, v. 28, p. 84-91, 2018.
- ATALLA, R.H.; NAGEL, S.C. Cellulose: its regeneration in native lattice. **Science**, v. 185, p. 522-523, 1974.
- ATALLA, R.H. Raman spectral studies of polymorphism in cellulose - part 1, celluloses I and II. **IPC Technical paper series**, v. 19, 1-17, 1975.
- AUAD, M.L.; CONTOS, V. S.; NUTT, S.; ARANGUREN, M.I.; MARCOVICH, N.E. Characterization of nanocellulose-reinforced shape memory polyurethanes. **Polymer International**, v. 57, n. 4, p. 651-659, 2008.
- AZEREDO, H.M.C. Bacterial cellulose for food applications. **International Journal Of Advances in Medical Biotechnology-IJAMB**, v. 1, n. 2, p. 2-6, 2018.
- AZRINA, Z.A.Z.; BEG, M.D.H.; ROSLI, M.Y.; RAMLI, R.; JUNADI, N.; ALAM, A.K.M.M. Spherical nanocrystalline cellulose (NCC) from oil palm empty fruit bunch pulp via ultrasound assisted hydrolysis. **Carbohydrate Polymers**, v. 162, p. 115-120, 2017.

BAHRAMI, B.; BEHZAD, T.; ZAMANI, A.; HEIDARIAN, P.; NASRI-NASRABADI, B. Optimal design of ozone bleaching parameters to approach cellulose nanofibers extraction from sugarcane bagasse fibers. **Journal of Polymers and the Environment**, v. 26, p. 4085-4094, 2018.

BALAKRISHNAN, P.; SREEKALA, M.S.; KUNAVAR, M.; HUSKIC, M.; THOMAS, S. Morphology, transport characteristics and viscoelastic polymer chain confinement in nanocomposites based on thermoplastic potato starch and cellulose nanofibers from pineapple leaf. **Carbohydrate Polymers**, v. 169, p. 176-188, 2017.

BALAKRISHNAN, P.; GOPI, S.; GEETHAMMA, V.G.; KALARIKKAL, N.; THOMAS, S. Cellulose nanofiber vs nanocrystals from pineapple leaf fiber: A comparative studies on reinforcing efficiency on starch nanocomposites. **Macromolecular Symposia**, v. 380, p. 1800102, 2018.

BARKER, S.A.; BOURNE, E.J.; PINDARD, R.M.; WHIFFEN, D.H. Spectra of acetals. Part II. The infrared and Raman spectra of substituted 1: 3-dioxolans. **Journal of the Chemical Society (resumed)**, v. 0, p. 807-813, 1959.

BARROS NETO, B.; SCARMINIO, I.S.; BRUNS, R.E. **Planejamento e otimização de experimentos**. Editora da Unicamp: Campinas, 1995.

BETTAIEB, F.; KHIARI, R.; HASSAN, M.L.; BELGACEM, M.N.; BRAS, J.; DUFRESNE, A.; MHENNI, M.F. Preparation and characterization of new cellulose nanocrystals from marine biomass *Posidonia oceanica*. **Industrial Crops and Products**, v. 72, p. 175-182, 2015.

BLEDZKI, A.K.; GASSAN, J. Composites reinforced with cellulose based fibers. **Progress in Polymer Science**, v. 24, p. 221-274, 1999.

BOGOLITSYN, K.G.; OVCHINNIKOV, D.V.; KAPLITSIN, P.A.; DRUZHININA, A.S.; PARSHINA, A.E.; SHUL'GINA, E.V.; SEMUSHINA, M.P.; ALESHINA, L.A. Isolation and structural characterization of cellulose from arctic brown algae. **Chemistry of Natural Compounds**, v. 53, p. 533-537, 2017.

BOONMEE, N.; PONGSAMANA, P. Spontaneous ignition of bagasse stockpiles in Thailand: a fire safety concern. **Environment, Energy and Natural Resources**, v. 21, p. 37-50, 2017.

BRITO, B.S.L.; PEREIRA, F.V.; PUTAUX, J.-L.; JEAN, B. Preparation, morphology and structure of cellulose nanocrystals from bamboo fibers. **Cellulose**, v. 19, p. 1527-1536, 2012.

BROWN JR, R.M. Cellulose microfibril assembly and orientation: recent developments. **Journal of Cell Science**, v. 1985, p. 13-32, 1985.

BRUNS, R.E.; BARROS NETO, B.; SCARMINIO, I.S. **Statistical Design - Chemometrics**. Amsterdam: Elsevier, 2006.

BUSSEMAKER, M.J.; ZHANG, D. Effect of ultrasound on lignocellulosic biomass as a pretreatment for biorefinery and biofuel applications. **Industrial and Engineering Chemistry Research**, v. 52, p.3563-3580, 2013.

CAI, Z.; KIM, J. Bacterial cellulose/poly (ethylene glycol) composite: characterization and first evaluation of biocompatibility. **Cellulose**, v. 17, n. 1, p. 83-91, 2010.

CAMPOS, A.; CORREA, A.C.; CANNELLA, D.; TEIXEIRA, E.M.; MARCONCINI, J.M.; DUFRESNE, A.; MATTOSO, L.H.C.; CASSLAND, P.; SANADI, A.R. Obtaining nanofibers from curauá and sugarcane bagasse fibers using enzymatic hydrolysis followed by sonication. **Cellulose**, v. 20, p. 1491-1500, 2013.

CARASCHI, J.C.; LEÃO, A.L. Characterization of curaua fiber. **Molecular Crystals and Liquid Crystals Science and Technology - Section A.**, v. 353, p. 149-152, 2000.

CARRILLO, F.; COLOM, X.; SUNOL, J.J.; SAURINA, J. Structural FTIR analysis and thermal characterisation of lyocell and viscose-type fibres. **European Polymer Journal**, v. 40, n. 9, p. 2229-2234, 2004.

CASAS, A.; PALOMAR, J.; ALONSO, M.V.; OLIET, M.; OMAR, S.; RODRIGUEZ, F. Comparison of lignin and cellulose solubilities in ionic liquids by COSMO-RS analysis and experimental validation. **Industrial Crops and Products**, v. 37, p. 155-163, 2012.

CASTRO, D.O.; FROLLINI, E.; RUVOLO-FILHO, A.; DUFRESNE, A. “Green polyethylene” and curauá cellulose nanocrystal based nanocomposites: Effect of vegetable oils as coupling agent and processing technique. **Journal of Polymer Science Part B: Polymer Physics**, v. 53, n. 14, p. 1010-1019, 2015.

CELLUFORCE. **Nanocrystalline cellulose manufacturing expert**. 2019. <<https://www.celluforce.com>>. Accessed 21 Oct. 2019.

CELLULOSE LAB. **Nanocellulose, cellulose nanocrystal (CNC or NCC), cellulose nanofibrils (CNF) and bacterial cellulose (BC) supplier**. 2019. <<https://www.celluloselab.com>>. Accessed 21 Oct. 2019.

CEPEA – *Centro de Estudos Avançados em Economia Aplicada da ESALQ/USP. Informativo setor florestal*. n. 214, 2019. <<https://www.cepea.esalq.usp.br/upload/revista/pdf/0387623001573584659.pdf>>. Accessed 03 Dec. 2019.

CERQUEIRA, D.A.; RODRIGUES FILHO, G.; MEIRELES, C.S. Optimization of sugarcane bagasse cellulose acetylation. **Carbohydrate Polymers**, v. 69, p. 579-582, 2007.

CHANDRA, R.; TAKEUCHI, H.; HASEGAWA, T. Methane production from lignocellulosic agricultural crop wastes: a review in context to second generation of biofuel production. **Renewable and Sustainable Energy Reviews**, v. 16, p. 1462-1476, 2012.

CHEN, W.; YU, H.; LIU, Y. Preparation of millimeter-long cellulose I nanofibers with diameters of 30–80 nm from bamboo fibers. **Carbohydrate Polymers**, v. 86, p. 453-461, 2011.

CHEN, W.; YU, H.; LIU, Y.; CHEN, P.; ZHANG, M.; HAI, Y. Individualization of cellulose nanofibers from wood using high-intensity ultrasonication combined with chemical pretreatments. **Carbohydrate Polymers**, v. 83, p. 1804-1811, 2011.

CHEN, Y.W.; LEE, H.V.; JUAN, J.C.; PHANG, S.-M. Production of new cellulose nanomaterial from red algae marine biomass *Gelidium elegans*. **Carbohydrate Polymers**, v. 151, p. 1210-1219, 2016.

CHENG, Q.; WANG, S.; RIALS, T.G. Poly(vinyl alcohol) nanocomposites reinforced with cellulose fibrils isolated by high intensity ultrasonication. **Composites: Part A**, v. 40, p.218-224, 2009.

CHENG, Q.; WANG, S.; HAN, Q. Novel process for isolating fibrils from cellulose fibers by high-intensity ultrasonication, II: fibril characterization. **Journal of Applied Polymer Science**, v. 115, p. 2756-2762, 2010.

CHENG, M.; QIN, Z.; LIU, Y.; QIN, Y.; LI, T.; CHEN, L.; ZHU, M. Efficient extraction of carboxylated spherical cellulose nanocrystals with narrow distribution through hydrolysis of lyocell fibers by using ammonium persulfate as an oxidant. **Journal of Materials Chemistry A**, v. 2, p. 251-258, 2014.

CHOWDHURY, Z.Z.; CHANDRAN, R.; JAHAN, A.; KHALID, K.; RAHMAN, M.M.; AL-AMIN, M.; AKBARZADEH, O.; BADRUDDIN, I.A.; KHAN, T.M.Y.; KAMANGAR, S.; HAMIZI, N.A.B. WAHAB, Y.A.; JOHAN, R.B.; ADEBISI, G.A. Extraction of cellulose nano-whiskers using ionic liquid-assisted ultra-sonication: optimization and mathematical modelling using box-behnken design. **Symmetry**, v. 11, n. 9, p. 1148, 2019.

CINTAS, P.; LUCHE, J.-L. Green chemistry: the sonochemical approach. **Green Chemistry**, v. 1, p. 115-125, 1999.

CIOLACU, D.; POPA, V.I. On the thermal degradation of cellulose allomorphs. **Cellulose Chemistry and Technology**, v. 40, p. 445-449, 2006.

CLARO, P.I.C., CORRÊA, A.C.; CAMPOS, A.; RODRIGUES, V.B., LUCHESI, B.R.; SILVA, L.E.; MATTOSO, L.H.C.; MARCONCINI, J.M. Curaua and eucalyptus nanofibers films by continuous casting: mechanical and thermal properties. **Carbohydrate Polymers**, v. 181, p. 1093-1101, 2018.

CLARO, P.I.C., CAMPOS, A.; CORRÊA, A.; RODRIGUES, V., LUCHESI, B.; SILVA, L.; TONOLI, G.; MATTOSO, L.; MARCONCINI, J. Curaua and eucalyptus nanofiber films by continuous casting: mixture of cellulose nanocrystals and nanofibrils. **Cellulose**, v. 26, n. 4, p. 2453-2470, 2019.

COLOM, X.; CARRILLO, F. Crystallinity changes in lyocell and viscose-type fibres by caustic treatment. **European Polymer Journal**, v. 38, p. 2225-2230, 2002.

CORRÊA, A.C.; TEIXEIRA, E.M.; CARMONA, V.B.; TEODORO, K.B.R.; RIBEIRO, C.; MATTOSO, L.H.C.; MARCONCINI, J.M. Obtaining nanocomposites of polyamide 6 and cellulose whiskers via extrusion and injection molding. **Cellulose**, v. 21, p. 311-322, 2014.

CORRÊA, A.C.; TEIXEIRA, E.M.; PESSAN, L.A.; MATTOSO, L.H.C. Cellulose nanofibers from curaua fibers. **Cellulose**, v. 17, p. 1183-1192, 2010.

DASH, S.; MOHAPATRA, S.; SAMANTARAY, D.P.; SETHI, A.K. Production of polyhydroxyalkanoates by sugar cane rhizospheric soil bacterial isolates. **Journal of Pure and Applied Microbiology**, v. 8, n. 6, p. 4889-4895, 2014.

DRIEMEIER, C.; FRANCISCO, L.H. X-ray diffraction from faulted cellulose I constructed with mixed I α -I β stacking. **Cellulose**, v. 21, n. 5, p. 3161-3169, 2014.

DURÁN, N.; LEMES, A.P.; SEABRA, A.B. Review of cellulose nanocrystals patents: preparation, composites and general applications. **Recent Patents on Nanotechnology**, v. 6, p. 16-28, 2012.

EGGLESTON, G.; LIMA, I. Sustainability issues and opportunities in the sugar and sugar-bioproduct industries. **Sustainability**, v. 7, p. 12209-12235, 2015.

EL ACHABY, M.; EL MIRI, N.E.; ABOULKAS, A.; ZAHOUILY, M.; BILAL, E.; BARAKAT, A.; SOLHY, A. Processing and properties of eco-friendly bio-nanocomposite films filled with cellulose nanocrystals from sugarcane bagasse. **International Journal of Biological Macromolecules**, v. 96, p. 340-352, 2017.

EL MIRI, N.; ABDELOUAHDI, K.; BARAKAT, A.; ZAHOUILY, M.; FIIHRI, A.; SOLHY, A.; EL ACHABY, M. Bio-nanocomposite films reinforced with cellulose nanocrystals: Rheology of film-forming solutions, transparency, water vapor barrier and tensile properties of films. **Carbohydrate Polymers**, v. 129, p. 156-167, 2015.

EL-HENDAWY, A.-N.A. Variation in the FTIR spectra of a biomass under impregnation, carbonization and oxidation conditions. **Journal of Analytical and Applied Pyrolysis**, v. 75, p. 159-166, 2006.

ENEL. **Tarifa de energia elétrica - Enel**. 2020. Available on: <www.eneldistribuicao.com.br/para-seu-negocio/tarifa-de-energia-eletrica>. Accessed 27 Feb. 2020.

ERIKSEN, Ø.; SYVERUD, K.; GREGERSEN, Ø. The use of microfibrillated cellulose produced from kraft pulp as strength enhancer in TMP paper. **Nordic Pulp & Paper Research Journal**, v. 23, p. 299-304, 2008.

ESA, F.; TASIRIN, S.M.; RAHMAN, N.A. Overview of bacterial cellulose production and application. **Agriculture and Agricultural Science Procedia**, v. 2, p. 113-119, 2014

ESSABIR, H.; BOUJMAL, R.; BENSALAH, M.O.; RODRIGUE, D.; BOUHFID, R.; QAISS, A.E.K. Mechanical and thermal properties of hybrid composites: oil-palm fiber/clay reinforced high density polyethylene. **Mechanics of Materials**, v. 98, p. 36-43, 2016.

EWULONU, C.M.; LIU, X.; WU, M.; HUANG, Y. Ultrasound-assisted mild sulphuric acid ball milling preparation of lignocellulose nanofibers (LCNFs) from sunflower stalks (SFS). **Cellulose**, v. 26, n. 7, p. 4371-4389, 2019.

EXILVA. **Microfibrillated cellulose – Exilva, a product from Borregaard**. 2019. <www.exilva.com/>. Accessed 16 Dec. 2019.

FARUK, O.; BLEDZKI, A.K.; FINK, H.-P.; SAIN, M. Biocomposites reinforced with natural fibers: 2000–2010. **Progress in Polymer Science**, v. 37, p. 1552-1596, 2012.

FAVIER, V.; CHANZY, H.; CAVAILLÉ, J.Y. Polymer nanocomposites reinforced by cellulose whiskers. **Macromolecules**, v. 28, p. 6365-6357, 1995.

FENG, Y.-H.; CHENG, T.Y.; YANG, W.G.; MA, P.T.; HE, H.Z.; YIN, X.C.; YU, X.X. Characteristics and environmentally friendly extraction of cellulose nanofibrils from sugarcane bagasse. **Industrial Crops and Products**, v. 111, p. 285-291, 2018.

FERREIRA, F.V.; MARIANO, M.; RABELO, S.C.; GOUVEIA, R.F.; LONA, L.M.F. Isolation and surface modification of cellulose nanocrystals from sugarcane bagasse waste: from a micro- to a nano-scale view. **Applied Surface Science**, v. 436, p. 1113-1122, 2018.

FRONE, A.N.; PANAITESCU, D.M.; DONESCU, D.; SPATARU, C.I.; RADOVICI, C.; TRUSCA, R.; SOMOGHI, R. Preparation and characterization of PVA composites with cellulose nanofibers obtained by ultrasonication. **BioResources**, v. 6, n. 1, p. 487-512, 2011.

GARCÍA, A.; GANDINI, A.; LABIDI, J.; BELGACEM, N.; BRAS, J. Industrial and crop wastes: a new source for nanocellulose biorefinery. **Industrial Crops and Products**, v. 93, p. 26-38, 2016.

GARDNER, K.H.; BLACKWELL, J. The structure of native cellulose. **Biopolymers**, v. 13, p. 1975-2001, 1974.

GILFILLAN, W.N.; MOGHADDAM, L.; DOHERTY, W.O.S. Preparation and characterization of composites from starch with sugarcane bagasse nanofibres. **Cellulose**, v. 21, p. 2695-2712, 2014.

GOELZER, F.D.E.; TISCHER, P.C.S.F.; VITORINO, J.C.; SIERAKOWSKI, M.R.; TISCHER, C.A. Production and characterization of nanospheres of bacterial cellulose from *Acetobacter xylinum* from processed rice bark. **Materials Science and Engineering: C**, v. 29, p. 546-551, 2009.

GONG, J.; LI, J.; XU, J.; XIANG, Z.; MO, L. Research on cellulose nanocrystals produced from cellulose sources with various polymorphs. **RSC Advances**, v. 7, p. 33486-33493, 2017.

GOUVEIA, E.R.; NASCIMENTO, R.T.; SOUTO-MAIOR, A.M.; ROCHA, G.J.M. Validação de metodologia para a caracterização química de bagaço de cana-de-açúcar. **Química Nova**, v. 32, p. 1500-1503, 2009.

GRANDE, R.; TROVATTI, E.; PIMENTA, M.T.B.; CARVALHO, A.J. Microfibrillated cellulose from sugarcane bagasse as a biorefinery product for ethanol production. **Journal of Renewable Materials**, v. 6, p. 195-202, 2018.

GRISHKEWICH, N.; Mohammed, N.; Tang, J.; Tam, K.C. Recent advances in the application of cellulose nanocrystals. **Current Opinion in Colloid & Interface Science**, v. 29, p. 32-45, 2017.

GUIMARÃES, J.L.; FROLLINI, E.; SILVA, C.G.; WYPYCH, F.; SATYANARAYANA, K.G. Characterization of banana, sugarcane bagasse and sponge gourd fibers of Brazil. **Industrial Crops and Products**, v. 30, p. 407-415, 2009.

GWON, J.G.; LEE, S.Y.; DOH, G.H.; KIM, J.H. Characterization of chemically modified wood fibers using FTIR spectroscopy for biocomposites. **Journal of Applied Polymer Science**, v. 116, p. 3212-3219, 2010.

HABIBI, Y.; CHANZY, H.; VIGNON, M.R.; TEMPO-mediated surface oxidation of cellulose whiskers. **Cellulose**, v. 13, p. 679-687, 2006.

HABIBI, Y.; LUCIA, L.A.; ROJAS, O.J. Cellulose nanocrystals: chemistry, self-assembly, and applications. **Chemical Reviews**, v. 110, p. 3479-3500, 2010.

HANLEY, S.J.; REVOL, J.-F.; GODBOUT, L.; GRAY, D.G.; Atomic force microscopy and transmission electron microscopy of cellulose from *Micrasterias denticulata*; evidence for a chiral helical microfibril twist. **Cellulose**, v. 4, p. 209-220, 1997.

HARAGUCHI, S.K.; SILVA, A.A.; TENORIO-NETO, E.T.; CARVALHO, G.M.; MUNIZ, E.C.; RUBIRA, A.F. Glycerol-derived polyurethane nanocomposites containing cellulose nanowhiskers. **Acta Scientiarum**, v. 35, n. 4, p. 747-755, 2013.

HEATH, L.; THIELEMANS, W. Cellulose nanowhisker aerogels. **Green Chemistry**, v. 12, n. 8, p. 1448-1453, 2010.

HENDERSON-SELLERS, B.; HENDERSON-SELLERS, A. Sensitivity evaluation of environmental models using fractional factorial experimentation. **Ecological Modelling**, v. 86, p. 291-295, 1996.

HOAREAU, W.; TRINDADE, W.G.; SIEGMUND, B.; CASTELLAN, A.; FROLLINI, E. Sugar cane bagasse and curaua lignins oxidized by chlorine dioxide and reacted with furfuryl alcohol: characterization and stability. **Polymer Degradation and Stability**, v. 86, p. 567-576, 2004.

HOFSETZ, K.; SILVA, M.A. Brazilian sugarcane bagasse: energy and non-energy consumption. **Biomass and Bioenergy**, v. 46, p. 564-573, 2012.

HUANG, H.; YE, D.; HUANG, B.; WEI, Z. Vanadium supported on viscose-based activated carbon fibers modified by oxygen plasma for the SCR of NO. **Catalysis Today**, v. 139, p. 100-108, 2008.

HUERTA, R.R.; SALDAÑA, M.D.A. Sequential treatment with pressurized fluid processing and ultrasonication for biorefinery of canola straw towards lignocellulosic nanofiber production. **Industrial Crops and Products**, v. 139, p. 111521, 2019.

HULLEMAN, S.H.D.; VAN HAZENDONK, J.M.; VAN DAM, J.E.G. Determination of crystallinity in native cellulose from higher plants with diffuse reflectance Fourier transform infrared spectroscopy. **Carbohydrate Research**, v. 261, p. 163-172, 1994.

IOELOVICH, M. Recent findings and the energetic potential of plant biomass as a renewable source of biofuels - a review. **Bioresources**, v. 10, p. 1879-1914, 2015.

ISOGAI, A.; USUDA, M.; KATO, T.; URYU, T.; ATALLA, R.H. Solid state CP/MAS ^{13}C NMR study of cellulose polymorphs. **Macromolecules**, v. 22, p. 3168-3172, 2002.

JACINTO, A.A. **Obtenção de nanocristais de celulose a partir de fibra de bambu usando ultrassom de alta intensidade**. Thesis (Master's degree in Nanoscience and Advanced Materials) – Federal University of ABC. Santo André, 2016.

JACINTO, A.A.; SPINACÉ, M.A.S. Mapping of the Brazilian groups studying nanocellulose. **Journal of Renewable Materials**, v. 7, p. 428-439, 2019.

JAKUBEK, Z.J.; CHEN, M.; COUILLARD, M.; LENG, T.; LIU, L.; ZOU, S.; BAXA, U.; CLOGSTON, J.D.; HAMAD, W.Y.; JOHNSTON, L.J. Characterization challenges for a cellulose nanocrystal reference material: dispersion and particle size distributions. **Journal of Nanoparticle Research**, v. 20:98, p. 1-16, 2018.

JANG, B.K.; KIM, M.H.; PARK, O.O. Effects of crystallinity and molecular weight on the melting behavior and cell morphology of expanded polypropylene in bead foam manufacturing. **Macromolecular Research**, v. 27, p. 1-8, 2019.

JONAS, R.; FARAH, L.F. Production and application of microbial cellulose. **Polymer Degradation and Stability**, v. 59, p. 101-106, 1998.

KALIA, S.; DUFRESNE, A.; CHERIAN, B.M.; KAITH, B.S.; AVÉROUS, L.; NJUGUNA, J.; NASSIOPOULOS, E. Cellulose-based bio-and nanocomposites: a review. **International Journal of Polymer Science**, v. 2011, article ID 837875, 2011.

KARGARZADEH, H.; AHMAD, I.; ABDULLAH, I.; DUFRESNE, A.; ZAINUDIN, S.Y.; SHELTAMI, R.M. Effects of hydrolysis conditions on the morphology, crystallinity, and thermal stability of cellulose nanocrystals extracted from kenaf bast fibers. **Cellulose**, v. 19, p. 855-866, 2012.

KARGARZADEH, H.; MARIANO, M.; HUANG, J.; LIN, N.; AHMAD, I.; DUFRESNE, A.; THOMAS, S. Recent developments on nanocellulose reinforced polymer nanocomposites: a review. **Polymer**, v. 132, p. 368-393, 2017.

KETABCHI, M.R.; KHALID, M.; RATNAM, C.T.; MANICKAM, S.; WALVEKAR, R.; HOQUE, M.E. Sonosynthesis of cellulose nanoparticles (CNP) from kenaf fiber: effects of processing parameters. **Fibers and Polymers**, v. 17, n. 9, p. 1352-1358, 2016.

KHALIL, H.P.S.A.; SAURABH, C.K.; ADNAN, A.S.; FAZITA, M.R.N.; SYAKIRA, M.I.; DAVOUDPOUR, Y.; RAFATULLAH, M.; ABDULLAH, C.K.; HAAFIZ, M.K.M.; DUNGANI, R. A review on chitosan-cellulose blends and nanocellulose reinforced chitosan

biocomposites: properties and their applications. **Carbohydrate Polymers**, v. 150, p. 216-226, 2016.

KHALIL, H.P.S.A.; BHAT, A.H.; YUSRA, A.F.I. Green composites from sustainable cellulose nanofibrils: A review. **Carbohydrate Polymers**, v. 87, p. 963-979, 2012.

KHALIL, H.P.S.A.; DAVOUDPOUR, Y.; ISLAM, M.N.; MUSTAPHA, A.; SUDESH, K.; DUNGANI, R.; JAWAID, M. Production and modification of nanofibrillated cellulose using various mechanical processes: a review. **Carbohydrate Polymers**, v. 99, p. 649-665, 2014.

KHANDELWAL, M.; WINDLE, A.H. Small angle X-ray study of cellulose macromolecules produced by tunicates and bacteria. **International Journal of Biological Macromolecules**, v. 68, p. 215-217, 2014.

KIM, N.-H.; HERTH, W.; VUONG, R.; CHANZY, H. The cellulose system in the cell wall of Micrasterias. **Journal of Structural Biology**, v. 117, p. 195-203, 1996.

KIMURA, S.; OHSHIMA, C.; HIROSE, E.; NISHIKAWA, J.; ITOH, T. Cellulose in the house of the appendicularian *Oikopleura rufescens*. **Photoplasma**, v. 216, p. 71-74, 2001.

KLEMM, D.; Philipp, B.; Heinze, T.; Heinze, U.; Wagenknecht, W. **Comprehensive Cellulose Chemistry**. Volume I. Weinheim: Wiley, 1998.

KLEMM, D.; HEUBLEIN, B.; FINK, H.-P.; BOHN, A. Cellulose: fascinating biopolymer and sustainable raw material. **Angewandte Chemie International Edition**, v. 44, p. 3358-3393, 2005.

KLEMM, D.; KRAMER, F.; MORITZ, S.; LINDSTRÖM, T.; ANKERFORS, M.; GRAY, D.; DORRIS, A. Nanocelluloses: a new family of nature-based materials. **Angewandte Chemie International Edition**, v. 50, p. 5438-5466, 2011.

KLEMM, D.; CRANSTON, E.D.; FISCHER, D.; GAMA, M.; KEDZIOR, S.A.; KRALISCH, D.; KRAMER, F.; KONDO, T.; LINDSTRÖM, T.; NIETZSCHE, S.; PETZOLD-WELCKE, K.; RAUCHFUß, F. Nanocellulose as a natural source for groundbreaking applications in materials science: today's state. **Materials Today**, v. 21, n. 7, p. 720-748, 2018.

KOSHY, R.R.; MARY, S.K.; THOMAS, S.; POTHAN, L.A. Environment friendly green composites based on soy protein isolate – a review. **Food Hydrocolloids**, v. 50, p. 174-192, 2015.

KOUTSIANITIS, D.; MITANI, C.; GIAGLI, K.; TSALAGKAS, D.; HALÁSZ, K.; KOLONICS, O.; GALLIS, C.; CSÓKA, L. Properties of ultrasound extracted bicomponent lignocellulose thin films. **Ultrasonics Sonochemistry**, v. 23, p. 148-155, 2015.

KRAFT, G.; KRAFT, M.; ZEPPEZAUER, F.; WEBER, H.K.; MOZDYNIEWICZ, D.; RÖDER, T. Cellulose degradation during viscose processing. **Lenzinger Berichte**, v. 91, p.19-22, 2013.

KRUEGER, C.; THOMMES, M.; KLEINEBUDDE, P. "MCC SANAQ®burst" - a new type of cellulose and its suitability to prepare fast disintegrating pellets. **Journal of Pharmaceutical Innovation**, v. 5, p.45-57, 2010.

KRUGER. **The FiloCell advantage**. 2019. <biomaterials.kruger.com/products/the-filocell-advantage>. Accessed 16 Dec. 2019.

KUMAR, V.; SHARMA, D.K.; BANSAL, V.; MEHTA, D.; SANGWAN, R.D.; YADAV, S.K. Efficient and economic process for the production of bacterial cellulose from isolated strain of *Acetobacter pasteurianus* of RSV-4 bacterium. **Bioresource Technology**, v. 275, p. 430-433, 2019.

LA MANTIA, F.P.; MORREALE, M. Green composites: a brief review. **Composites: Part A**, v. 42, p.579-588, 2011.

LAM, N.T.; CHOLLAKUP, R.; SMITTHIPONG, W.; NIMCHUA, T.; SUKYAI, P. Utilizing cellulose from sugarcane bagasse mixed with poly (vinyl alcohol) for tissue engineering scaffold fabrication. **Industrial Crops and Products**, v. 100, p. 183-197, 2017.

LEAL NETA, L.S.; COSTELLA, A.M.S.; MELO FILHO, J.A.; GIACON, V.M. *Caracterização físico-química de fibras de curauá e sua aplicação em compósitos poliméricos*. **Scientia Amazonia**, v. 4, p. 21-27, 2015.

LEÃO, R.M.; MILÉO, P. C.; MAIA, J.M.; LUZ, S.M. Environmental and technical feasibility of cellulose nanocrystal manufacturing from sugarcane bagasse. **Carbohydrate Polymers**, v. 175, p. 518-529, 2017.

LEE, H.V.; HAMID, S.B.A.; ZAIN, S.K. Conversion of lignocellulosic biomass to nanocellulose: structure and chemical process. **The Scientific World Journal**, v. 2014, 2014.

LEITE, A.L.M.P.; ZANON, C.D.; MENEGALLI, F.C. Isolation and characterization of cellulose nanofibers from cassava root bagasse and peelings. **Carbohydrate Polymers**, v. 157, p. 962-970, 2017.

LEONELLI, C.; MASON, T.J. Microwave and ultrasonic processing: Now a realistic option for industry. **Chemical Engineering and Processing: process intensification**, v. 49, p. 885-900, 2010.

LI, C.; LI, L.; LI, J.; WU, X.; QI, L.; LI, W. Fabrication and characterisation of viscose fibre with photoinduced heat-generating properties. **Cellulose**, v. 26, n. 3, p. 1631-1640, 2019.

LI, Q.; RENNECKAR, S. Supramolecular structure characterization of molecularly thin cellulose I nanoparticles. **Biomacromolecules**, v. 12, n. 3, p. 650-659, 2011.

LI, W.; YUE, J.; LIU, S. Preparation of nanocrystalline cellulose via ultrasound and its reinforcement capability for poly(vinyl alcohol) composites. **Ultrasonics Sonochemistry**, v. 19, p. 479-485, 2012.

LIANG, C.Y.; MARCHESSAULT, R.H. Infrared spectra of crystalline polysaccharides. II. Native celluloses in the region from 640 to 1700 cm^{-1} . **Journal of Polymer Science Part A: general papers** banner, v. 39, p. 269-278, 1959.

LÖBMANN, K.; SVAGAN, A.J. Cellulose nanofibers as excipient for the delivery of poorly soluble drugs. **International Journal of Pharmaceutics**, v. 533, n. 1, p. 285-297, 2017.

LU, Q.; TANG, L.; LIN, F.; WANG, S.; CHEN, Y.; CHEN, X.; HUANG, B. Preparation and characterization of cellulose nanocrystals via ultrasonication-assisted FeCl_3 -catalyzed hydrolysis. **Cellulose**, v. 21, p. 3497-3506, 2014.

LU, H.; ZHANG, L.; LIU, C.; HE, Z.; ZHOU, X.; NI, Y. A novel method to prepare lignocellulose nanofibrils directly from bamboo chips. **Cellulose**, v. 25, p. 7043-7051, 2018.

LUNZ, J.N.; CORDEIRO, S.B.; MOTA, J.C.F.; MARQUES, M.F.V. Statistical experimental design for obtaining nanocellulose from curaua fiber. **Macromolecular Symposia**, v. 319, p. 99-107, 2012.

LUO, J.; FANG, Z.; SMITH JR, R.L. Ultrasound-enhanced conversion of biomass to biofuels. **Progress in Energy and Combustion Science**, v. 41, p. 56-93, 2014.

LUO, S.; NETRAVALI, A.N. Interfacial and mechanical properties of environment-friendly “green” composites made from pineapple fibers and poly(hydroxybutyrate-co-valerate) resin. **Journal of Materials Science**, v. 34, p. 3709-3719, 1999.

MAHARDIKA, M.; ABRAL, H.; KASIM, A.; ARIEF, S.; ASROFI, M. Production of nanocellulose from pineapple leaf fibers via high-shear homogenization and ultrasonication. **Fibers**, v. 6, n. 2, p. 28, 2018.

MAHESWARI, C.U.; REDDY, K.O.; MUZENDA, E.; GUDURI, B.R.; RAJULU, A.V.; Extraction and characterization of cellulose microfibrils from agricultural residue – *Cocos nucifera* L. **Biomass and Energy**, v. 46, p. 555-563, 2012.

MAJKA, T.M.; COKOT, M.; PIELICHOWSKI, K. Studies on the thermal properties and flammability of polyamide 6 nanocomposites surface-modified via layer-by-layer deposition of chitosan and montmorillonite. **Journal of Thermal Analysis and Calorimetry**, v. 131, p. 405-416, 2018.

MAN, Z.; MUHAMMAD, N.; SARWONO, A.; BUSTAM, M.A.; KUMAR, M.V.; RAFIQ, S. Preparation of cellulose nanocrystals using an ionic liquid. **Journal of Polymers and The Environment**, v. 19, p. 726-731, 2011.

MANDAL, A.; CHAKRABARTY, D. Isolation of nanocellulose from waste sugarcane bagasse (SCB) and its characterization. **Carbohydrate Polymers**, v. 86, p. 1291-1299, 2011.

MANO, B.; ARAÚJO, J.R.; SPINACÉ, M.A.S.; DE PAOLI, M.A. Polyolefin composites with curaua fibres: Effect of the processing conditions on mechanical properties, morphology and fibres dimensions. **Composites Science and Technology**, v. 70, p. 29-35, 2010.

MANZATO, L.; RABELO, L.C.A.; SOUZA, S.M.; SILVA, C.G.; SANCHES, E.A.; RABELO, D.; MARIUBA, L.A.M.; SIMONSEN, J. New approach for extraction of cellulose from tucumã's endocarp and its structural characterization. **Journal of Molecular Structure**, v. 1143, p. 229-234, 2017.

MARIANO, M.; CERCENÁ, R.; SOLDI, V. Thermal characterization of cellulose nanocrystals isolated from sisal fibers using acid hydrolysis. **Industrial Crops and Products**, v. 94, p. 454-462, 2016.

MARIANO, M.; EL KISSI, N.; DUFRESNE, A. Cellulose nanocrystals and related nanocomposites: review of some properties and challenges. **Journal of Polymer Science Part B: Polymer Physics**, v. 52, n. 12, p. 791-806, 2014.

MARQUES, G.; GUTIÉRREZ, A.; DEL RÍO, J.C. Chemical characterization of lignin and lipophilic fractions from leaf fibers of curaua (*Ananas erectifolius*). **Journal of Agricultural and Food Chemistry**, v. 55, p. 1327-1336, 2007.

MARSH, G. Next step for automotive materials. **Materials Today**, v. 6, p.36-43, 2003.

MARTÍNEZ-SANZ, M.; LOPEZ-SANCHEZ, P.; GIDLEY, M.J.; GILBERT, E.P. Evidence for differential interaction mechanism of plant cell wall matrix polysaccharides in hierarchically-structured bacterial cellulose. **Cellulose**, v. 22, p. 1541-1563, 2015.

MATTONAI, M.; PAWCENIS, D.; DEL SEPPIA, S.; ŁOJEWSKA, J.; RIBECHINI, E. Effect of ball-milling on crystallinity index, degree of polymerization and thermal stability of cellulose. **Bioresource Technology**, v. 270, p. 270-277, 2018.

MCKENDRY, P. Energy production from biomass (part 1): overview of biomass. **Bioresource Technology**, v. 83, p. 37-46, 2002.

MILANEZ, D.H.; AMARAL, R.M.D.; FARIA, L.I.L.D.; GREGOLIN, J.A.R. Assessing nanocellulose developments using science and technology indicators. **Materials Research**, v. 16, n. 3, p. 635-641, 2013.

MOHANTY, A.K.; MISRA, M.; DRZAL, L.T. Sustainable bio-composites from renewable resources: opportunities and challenges in the green materials world. **Journal of Polymers and the Environment**, v. 10, p. 19-26, 2002.

MOHANTY, A.K.; VIVEKANANDHAN, S.; PIN, J.M.; MISRA, M. Composites from renewable and sustainable resources: challenges and innovations. **Science**, v. 362, n. 6414, p. 536-542, 2018.

MOHOMANE, S.M.; LINGANISO, L.Z.; BUTHELEZI, T.; MOTAUNG, T.E. Effect of extraction period on properties of sugarcane bagasse and softwood chips cellulose. **Wood Research**, v. 62, p. 931-938, 2017.

MONTEIRO, S.; CALADO, V.; RODRIGUEZ, R.J.S.; MARGEM, F.M. Thermogravimetric behavior of natural fibers reinforced polymer composites - an overview. **Materials Science and Engineering: A**, v. 557, p. 17-28, 2012.

MOON, R.J.; MARTINI, A.; NAIRN, J.; SIMONSEN, J.; YOUNGBLOOD, J. Cellulose nanomaterials review: structure, properties and nanocomposites. **Chemical Society Reviews**, v. 40, p. 3941-3994, 2011.

MOTAUNG, T.E.; MOKHOTHU, T.H. The influence of supermasscolloider on the morphology of sugarcane bagasse and bagasse cellulose. **Fibers and Polymers**, v. 17, p. 343-348, 2016.

MULINARI, D.R.; VOORWALD, H.J.C.; CIOFFI, M.O.H.; SILVA, M.L.C.P.; LUZ, S.M. Preparation and properties of HDPE/sugarcane bagasse cellulose composites obtained for thermokinetic mixer. **Carbohydrate Polymers**, v. 75, p. 317-321, 2009.

NACAS, A.M.; SILVA, R.; DE PAOLI, M.-A.; SPINACÉ, M.A.S. Polypropylene composite reinforced with fibrillated curaua fiber and using maleic anhydride as coupling agent. **Journal of Applied Polymer Science**, v. 134, p. 44913-44921, 2017.

NADUPARAMBATH, S.; JINITHA, T.V.; SHANIBA, V.; SREEJITH, M.P.; BALAN, A.K.; PURUSHOTHAMAN, E. Isolation and characterization of cellulose nanocrystals from sago seed shells. **Carbohydrate Polymers**, v. 180, p. 13-20, 2018.

NASCIMENTO, S.A.; REZENDE, C.A. Combined approaches to obtain cellulose nanocrystals, nanofibrils and fermentable sugars from elephant grass. **Carbohydrate Polymers**, v. 180, p. 38-45, 2018.

NECHYPORCHUK, O.; BELGACEM, M.N.; BRAS, J. Production of cellulose nanofibrils: a review of recent advances. **Industrial Crops and Products**, v. 93, p. 2-25, 2016.

NELSON, M.L.; O'CONNOR, R.T. Relation of certain infrared bands to cellulose crystallinity and crystal latticed type. Part I. Spectra of lattice types I, II, III and of amorphous cellulose. **Journal of Applied Polymer Science**, v. 8, p. 1311-1324, 1964.

NIPPON PAPER. **Cellulose nanofiber manufacturing technology and application development**. 2019. <www.nipponpapergroup.com/english/research/organize/cnf.html>. Accessed 16 Dec. 2019.

NISHINO, T.; TAKANO, K.; NAKAMAE, K.; Elastic modulus of the crystalline regions of cellulose polymorphs. **Journal of Polymer Science: Part B**, v. 33, p. 1647-1651, 1995.

OH, S.Y.; YOO, D. II; SHIN, Y.; KIM, H.C.; KIM, H.Y.; CHUNG, Y.S.; PARK, W.H.; YOOK, J.H. Crystalline structure analysis if cellulose treated with sodium hydroxide and carbon dioxide by means of X-ray diffraction and FTIR spectroscopy. **Carbohydrate Research**, v. 340, p. 2376-2391, 2005.

OHSHIMA, N.; ITOH, T.; SHIGEMATSU, M.; SHIMOHATA, I.; TANAHASHI, M. Structural analysis for cellulose fibers treated by high pressure steam. **Sen'i Gakkaishi**, 59, p. 83-32, 2003.

OJI PAPER. **The world's first! Three forms of CNF**. 2019. <www.ojiholdings.co.jp/english/r_d/theme/cnf.html>. Accessed 16 Dec. 2019.

OLIVEIRA, R.L.; VIEIRA, J.G.; BARUD, H.S.; ASSUNÇÃO, R.M.N.; FILHO, G.R.; RIBEIRO, S.J.L.; MESSADEQQ, Y. Synthesis and characterization of methylcellulose produced from bacterial cellulose under heterogeneous condition. **Journal of the Brazilian Chemical Society**, v. 26, p. 1861-1870, 2015.

O'SULLIVAN, A. Cellulose: the structure slowly unravels. **Cellulose**, v. 4, p. 173-207, 1997.

ÖZGENÇ, O.; DURMAZ, S.; BOYACI, I.H.; EKSI-KOÇAK, H. Determination of chemical changes in heat-treated wood using ATR-FTIR and FT Raman spectrometry. **Spectrochimica Acta Part A: Molecular and Biomolecular Spectroscopy**, v. 171, p. 395-400, 2017.

PA'E, N.; Salehudin, M.H.; Hassan, N.D.; Marsin, A.M.; Muhamad, I.I. **Thermal behavior of bacterial cellulose based hydrogels with other composites and related instrumental analysis**. In: MONDAL, M.I.H. (ed.) Cellulose-based superabsorbent hydrogels. Cham: Springer Nature, 2018.

PANDEY, A.; SOCCOL, C.R.; NIGAM, P.; SOCCOL, V.T. Biotechnological potential of agro-industrial residues. I: sugarcane bagasse. **Bioresource Technology**, v. 74, p. 69-80, 2000.

PARK, S.; BAKER, J.O.; HIMMEL, M.E.; PARILLA, P.A.; JOHNSON, D.K. Cellulose crystallinity index: measurement techniques and their impact on interpreting cellulase performance. **Biotechnology for Biofuels**, v. 3, p. 1-10, 2010.

PASTAROVA, I.; BOTTO, R.E.; ARISZ, P.W.; BOON, J.J. Cellulose char structure: a combined analytical Py-GC-MS, FTIR, and NMR study. **Carbohydrate Research**, v. 262, p. 27-47, 1994.

PENG, H.; ZHOU, M.; YU, Z.; ZHANG, J.; RUAN, R.; WAN, Y.; LIU, Y. Fractionation and characterization of hemicelluloses from young bamboo (*Phyllostachys pubescens* Mazel) leaves. **Carbohydrate Polymers**, v. 95, p. 262-271, 2013.

PEREIRA, F.V.; PAULA, E.L.; MESQUITA, J.P.; ALMEIDA, A.L.; MANO, V. Bionanocompósitos preparados por incorporação de nanocristais de celulose em polímeros biodegradáveis por meio de evaporação de solvente, automontagem ou eletrofiação. **Química Nova**, v. 37, p. 1209-1219, 2014.

PINJARI, D.V.; PANDIT, A.B. Cavitation milling of natural cellulose to nanofibrils. **Ultrasonics Sonochemistry**, v. 17, p. 845-852, 2010.

POLETTTO, M.; ORNAGHI JR, H.L.; ZATTERA, A.J. Native cellulose: structure, characterization and thermal properties. **Materials**, v. 7, p. 6105-6119, 2014.

POLETTTO, M.; ZATTERA, A.J.; FORTE, M.M.; SANTANA, R.M. Thermal decomposition of wood: Influence of wood components and cellulose crystallite size. **Bioresource Technology**, v. 109, p. 148-153, 2012.

PRADO, K.S.; SPINACÉ, M.A.S. Characterization of fibers from pineapple's crown, rice husks and cotton textile residues. **Materials Research**, v. 18, p. 530-537, 2015.

PRADO, K.S.; GONZALES, D.; SPINACÉ, M.A.S. Recycling of viscose yarn waste through one-step extraction of nanocellulose. **International Journal of Biological Macromolecules**, v. 136, p. 729-737, 2019.

PRADO, K.S.; JACINTO, A.A.; SPINACÉ, M.A.S. Cellulose nanostructures extracted from pineapple fibres. In: JAWAID, M. *et al.* (ed) **Pineapple leaf fibers, green energy and technology**. Springer Nature: Singapore, 2020.

PURCHASE, B.S.; ROSETTENSTEIN, S.; BEZUIDENHOUDT, D.V. Challenges and potential solutions for storage of large quantities of bagasse for power generation. **Proceedings of the South African Sugar Technologists Association**, v. 86, p. 495-513, 2013.

RAJINIPRIYA, M.; NAGALAKSHMAIAH, M.; ROBERT, M.; ELKOUN, S. Importance of agricultural and industrial waste in the field of nanocellulose and recent industrial developments of wood based nanocellulose: a review. **ACS Sustainable Chemistry & Engineering**, v. 6, n. 3, p. 2807-2828, 2018.

RAMAMOORTHY, S.; SKRIFVAR, M.; PERSSON, A. A review of natural fibers used in biocomposites: plant, animal and regenerated cellulose fibers. **Polymer Reviews**, v. 55, p. 107-162, 2015.

RAMESH, M.; PALANIKUMAR, K.; REDDY, K.H. Plant fiber based bio-composites: sustainable and renewable green materials. **Renewable and Sustainable Energy Reviews**, v. 79, p. 558-584, 2017.

RANI, A.; MONGA, S.; BANSAL, M.; SHARMA, A. Bionanocomposites reinforced with cellulose nanofibers derived from sugarcane bagasse. **Polymer Composites**, v. 39, p. E55-E64, 2018.

RAVINDRAN, L.; SREEKALA, M.S.; THOMAS, S. Novel processing parameters for the extraction of cellulose nanofibres (CNF) from environmentally benign pineapple leaf fibres (PALF): structure-property relationships. **International Journal of Biological Macromolecules**, v. 131, p. 858-870, 2019.

REINIATI, I.; HRYMAK, A.N.; MARGARITIS, A. Recent developments in the production and applications of bacterial cellulose fibers and nanocrystals. **Critical Reviews in Biotechnology**, v. 37, p. 510-524, 2016.

REZENDE, C.A.; LIMA, M.A.; MAZIERO, P.; AZEVEDO, E.R.; GARCIA, W.; POLIKARPOV, I. Chemical and morphological characterization of sugarcane bagasse submitted to a delignification process for enhanced enzymatic digestibility. **Biotechnology for Biofuels**, v. 4, p. 1-18, 2011.

RÖDER, T.; MOOSBAUER, J.; SCHLADER, S.; WÖSS, K.; KRAFT, G. Man-made cellulose fibres – a comparison based on morphology and mechanical properties. **Lenzinger Berichte**, v. 91, p.7-12, 2013.

ROJO, E.; ALONSO, M.V.; DOMINGUEZ, J.C.; SAZ-OROZCO, B.D.; OLIET, M.; RODRIGUEZ, F. Alkali treatment of viscose cellulosic fibers from eucalyptus wood: structural, morphological, and thermal analysis. **Journal of Applied Polymer Science**, v. 130, p. 2198-2204, 2013.

ROMAN, M.; WINTER, W.T. Effect of sulfate groups from sulfuric acid hydrolysis on the thermal degradation behavior of bacterial cellulose. **Biomacromolecules**, v. 5, p. 1671-1677, 2004.

ROSA, M.F.; MEDEIROS, E.S.; MALMONGE, J.A.; GREGORSKI, K.S.; WOOD, D.F.; MATTOSO, L.H.C.; GLENN, G.; ORTS, W.J.; IMAM, S.H. Cellulose nanowhiskers from coconut husk fibers: Effect of preparation conditions on their thermal and morphological behavior. **Carbohydrate Polymers**, v. 81, p. 83-92, 2010.

SACUI, I.A.; NIEUWENDAAL, R.C.; BURNETT, D.J.; STRANICK, S.J.; JORFI, M.; WEDER, C.; FOSTER, E.J.; OLSSON, R.T.; GILMAN, J.W. Comparison of the properties of cellulose nanocrystals and cellulose nanofibrils isolated from bacteria, tunicate, and wood processed using acid, enzymatic, mechanical, and oxidative methods. **ACS Applied Materials & Interfaces**, v. 6, p. 6127-6138, 2014.

SAMIEE, S.; AHMADZADEH, H.; HOSSEINI, M.; LYON, S. Algae as a source of microcrystalline cellulose. In: HOSSEINI, M. (ed). **Advanced bioprocessing for alternative fuels, biobased chemicals, and bioproducts**. Woodhead Publishing: Cambridge, 2019. p. 331-350.

SANTOS, A.S.F.; PEREIRA-DA-SILVA, M.A.; OLIVEIRA, J.E.; MATTOSO, L.H.; MEDEIROS, E.S. Accelerated sonochemical extraction of cellulose nanowhiskers. **Journal of Nanoscience and Nanotechnology**, v. 16, n. 6, p. 6535-6539, 2016.

SANTOS, B.H.; JACINTO, A.A.; PRADO, K.S.; SPINACÉ, M.A.S. Influence of sugarcane bagasse fiber size on biodegradable composites of thermoplastic starch. **Journal of Renewable Materials**, v. 6, p. 176-182, 2018.

SANTUCCI, B.S.; BRAS, J.; BELGACEM, M.N.; CURVELO, A.A.S.; PIMENTA, M.T.B. Evaluation of the effects of chemical composition and refining treatments on the properties of nanofibrillated cellulose films from sugarcane bagasse. **Industrial Crops and Products**, v. 91, p. 238-248, 2016.

SATYANARAYANA, K.G.; ARIZAGA, G.G.C.; WYPYCH, F. Biodegradable composites based on lignocellulosic fibers - an overview. **Progress in Polymer Science**, v. 34, p. 982-1021, 2009.

SCHENZEL, K.; FISCHER, S. NIR FT Raman spectroscopy—a rapid analytical tool for detecting the transformation of cellulose polymorphs. **Cellulose**, v. 8, n. 1, p. 49-57, 2001.

SCHENZEL, K.; ALMLÖF, H.; GERMGÅRD, U. Quantitative analysis of the transformation process of cellulose I→ cellulose II using NIR FT Raman spectroscopy and chemometric methods. **Cellulose**, v. 16, n. 3, p. 407-415, 2009.

SCHWANNINGER, M.; RODRIGUES, J.C.; PEREIRA, H.; HINTERSTOISSER, B. Effects of short-time vibratory ball milling on the shape of FT-IR spectra of wood and cellulose. **Vibrational Spectroscopy**, v. 36, p. 23-40, 2004.

SEABRA, A.B.; BERNARDES, J.S.; FÁVARO, W.J.; PAULA, A.J.; DURÁN, N. Cellulose nanocrystals as carriers in medicine and their toxicities: a review. **Carbohydrate Polymers**, v. 181, p. 514-527, 2018.

SEKKAL, M.; DINCQ, V.; LEGRAND, P.; HUVENNE, J. P. Investigation of the glycosidic linkages in several oligosaccharides using FT-IR and FT Raman spectroscopies. **Journal of Molecular Structure**, v. 349, p. 349-352, 1995.

SENA NETO, A.R.; ARAUJO, M.A.; BARBOZA, R.M.; FONSECA, A.S.; TONOLI, G.H.; SOUZA, F.V.D.; MATTOSO, L.H.C.; MARCONCINI, J.M. Comparative study of 12 pineapple leaf fiber varieties for use as mechanical reinforcement in polymer composites. **Industrial Crops and Products**, v. 64, p. 68-78, 2015.

SERPA, A.; VELÁSQUEZ-COCK, J.; GAÑÁN, P.; CASTRO, C.; VÉLEZ, L.; ZULUAGA, R. Vegetable nanocellulose in food science: a review. **Food Hydrocolloids**, v. 57, p. 178-186, 2016.

SHAH, N.; UL-ISLAM, M.; KHATTAK, W.A.; PARK, J.K. Overview of bacterial cellulose composites: a multipurpose advanced material. **Carbohydrate Polymers**, v. 98, p. 1585-1598, 2013.

SHI, Z.; ZHANG, Y.; PHILLIPS, G.O.; YANG, G. Utilization of bacterial cellulose in food. **Food Hydrocolloids**, v. 35, p. 539-545, 2014.

SINGH, R.; PRAKASH, A.; BALAGURUMURTHY, B.; SINGH, R.; SARAN, S.; BHASKAR, T. Hydrothermal liquefaction of agricultural and forest biomass residue: comparative study. **Journal of Material Cycles and Waste Management**, v. 17, n. 3, p. 442-452, 2015.

SINGH, S.; GAIKWAD, K.K.; PARK, S.-I.; LEE, Y.S. Microwave-assisted step reduced extraction of seaweed (*Gelidiella acerosa*) cellulose nanocrystals. **International Journal of Biological Macromolecules**, v. 99, p. 506-510, 2017.

SINGH, S.C.; MURTHY, Z.V.P. Study of cellulosic fibres morphological features and their modifications using hemicelluloses. **Cellulose**, v. 24, p. 3119-3130, 2017.

SIRÓ, I.; PLACKETT, D. Microfibrillated cellulose and new nanocomposite materials: a review. **Cellulose**, v. 17, n. 3, p. 459-494, 2010.

SOFILA, M.R.K.; BROWN, R.J.; TSUZUKI, T.; RAINEY, T.J. A comparison of cellulose nanocrystals and cellulose nanofibres extracted from bagasse using acid and ball milling methods. **Advances in Natural Sciences: Nanoscience and Nanotechnology**, v. 7, p. 1-9, 2016.

SOYEKWO, F.; ZHANG, Q.G.; LIN, X.C.; WU, X.M.; ZHU, A.M.; LIU, Q.L. Facile preparation and separation performances of cellulose nanofibrous membranes. **Journal of Applied Polymer Science**, v. 133, p. 43544-43556, 2016.

SPINACÉ, M.A.S.; LAMBERT, C.S.; FERMOSELLI, K.K.G.; DE PAOLI, M.A. Characterization of lignocellulosic curaua fibres. **Carbohydrate Polymers**, v. 77, p. 47-53, 2009.

STEPANIK, T.M.; EWING, D.E.; WHITEHOUSE, R. Electron treatment of wood pulp for the viscose process. **Radiation Physics and Chemistry**, v. 57, p. 377-379, 2000.

SUGIYAMA, J.; OKANO, T.; YAMAMOTO, H.; HORII, F. Transformation of Valonia cellulose crystals by an alkaline hydrothermal treatment. **Macromolecules**, v. 23, p. 3196-3198, 1990.

SUSLICK, K.S. Sonochemistry. **Science**, v. 247, p. 1439-1445, 1990.

SUTKAR, V.S.; GOGATE, P.R.; CSÓKA, L. Theoretical prediction of cavitation activity distribution in sonochemical reactors. **Chemical Engineering Journal**, v. 158, p. 290-295, 2010.

SYNTH. **Celulose microcristalina P.A.** 2019. <<https://www.lojasynth.com/reagentes-analiticosmaterias-primas/reagentes-analiticosmaterias-primas/celulose-microcristalina-p-a>>. Accessed 21 Oct. 2019.

TERAUCHI, M.; NAGASATO, C.; INOUE, A.; ITO, T.; MOTOMURA, T. Distribution of alginate and cellulose and regulatory role of calcium in the cell wall of the brown alga *Ectocarpus siliculosus* (Ectocarpales, Phaeophyceae). **Planta**, v. 244, p. 361-377, 2016.

THOMAS, B.; RAJ, M.C.; JOY, J.; MOORES, A.; DRISKO, G.L.; SANCHEZ, C. Nanocellulose, a versatile green platform: from biosources to materials and their applications. **Chemical Reviews**, v. 118, n. 24, p. 11575-11625, 2018.

TIBOLLA, H.; PELISSARI, F.M.; RODRIGUES, M.I.; MENEGALLI, F.C. Cellulose nanofibers produced from banana peel by enzymatic treatment: Study of process conditions. **Industrial Crops and Products**, v. 95, p. 664-674, 2017.

TISCHER, P.C.S.F.; SIERAKOWSKI, M.R.; WESTFAHL JR, H.; TISCHER, C.A. Nanostructural reorganization of bacterial cellulose by ultrasonic treatment. **Biomacromolecules**, v. 11, p. 1217-1224, 2010.

TOMAK, E.D.; AY, N.; TOPALOGLU, E.; GUMUSKAYA, E.; YILDIZ, U.C. An FT-IR study of the changes in chemical composition of bamboo degraded by brown-rot fungi. **International Biodeterioration & Biodegradation**, v. 85, p. 131-138, 2013.

TONOLI, G.H.D.; TEIXEIRA, E.M.; CÔRREA, A.C.; MARCONCINI, J.M.; CAIXETA, L.A.; SILVA, M.A.P.; MATTOSO, L.H.C. Cellulose micro/nanofibres from *Eucalyptus* kraft pulp: preparation and properties. **Carbohydrate Polymers**, v. 89, p. 80-88, 2012.

UNIVERSITY OF MAINE. The process development center. 2019. <<https://umaine.edu/pdc/nanocellulose>>. Accessed 21 Oct. 2019.

URIBE, B.E.B.; CARVALHO, A.J.F.; TARPANI, J.R. Low-cost, environmentally friendly route to produce glass fiber-reinforced polymer composites with microfibrillated cellulose interphase. **Journal of Applied Polymer Science**, v. 133, n. 46, 2016.

URIBE, B.E.B.; CHIROMITO, E.M.S.; CARVALHO, A.J.F.; TARPANI, J.R. Low-cost, environmentally friendly route for producing CFRP laminates with microfibrillated cellulose interphase. **Express Polymer Letters**, v. 11, p. 47, 2017.

TRACHE, D.; HUSSIN, M.H.; HAAFIZ, M.K.M.; THAKUR, V.K. Recent progress in cellulose nanocrystals: sources and production. **Nanoscale**, v. 9, p. 1763-1786, 2017.

VANDERHART, D.L.; ATALLA, R.H. Studies of microstructure in native celluloses using solid-state ^{13}C NMR. **Macromolecules**, v. 17, p. 1465-1472, 1984.

VASCONCELOS, N.F.; FEITOSA, J.P.A.; GAMA, F.M.P.; MORAIS, J.P.S.; ANDRADE, F.K.; SOUZA, M.D.S.M.; ROSA, M.F. Bacterial cellulose nanocrystals produced under different hydrolysis conditions: properties and morphological features. **Carbohydrate Polymers**, v. 155, p. 425-431, 2017.

VELMURUGAN, R.; MUTHUKUMAR, K. Ultrasound-assisted alkaline pretreatment of sugarcane bagasse for fermentable sugar production: Optimization through response surface methodology. **Bioresource Technology**, v. 112, p. 293-299, 2012.

WANG, S.; CHENG, Q. A novel process to isolate fibrils from cellulose fibers by high-intensity ultrasonication, part 1: process optimization. **Journal of Applied Polymer Science**, v. 113, p. 1270-1275, 2009.

WANG, N.; DING, E.; CHENG, R. Thermal degradation behaviors of spherical cellulose nanocrystals with sulfate groups. **Polymer**, v. 48, p. 3486-3493, 2007.

WANG, H.; LI, D.; ZHANG, R. Preparation of ultralong cellulose nanofibers and optically transparent nanopapers derived from waste corrugated paper pulp. **Bioresources**, v. 8, p. 1374-1384, 2013.

WARDHONO, E.Y.; KANANI, N.; ALFIRANO, A. A simple process of isolation microcrystalline cellulose using ultrasonic irradiation. **Journal of Dispersion Science and Technology**, v. 40, p. 1-10, 2019.

WAS-GUBALA, J.; MACHNOWSKI, W. Application of Raman spectroscopy for differentiation among cotton and viscose fibers dyed with several dye classes. **Spectroscopy Letters**, v. 47, n. 7, p. 527-535, 2014.

WONG, S.-S.; KASAPIS, S.; TAN, Y.M. Bacterial and plant cellulose modification using ultrasound irradiation. **Carbohydrate Polymers**, v. 77, p. 280-287, 2009.

WU, H.; WILLIAMS, G.R.; WU, J.; WU, J.; LI, H.; NIU, S.; WANG, H.; ZHU, L. Regenerated chitin fibers reinforced with bacterial cellulose nanocrystals as suture biomaterials. **Carbohydrate Polymers**, v. 180, p. 304-313, 2018.

YANG, H.; YAN, R.; CHEN, H.; LEE, D.H.; ZHENG, C. Characteristics of hemicellulose, cellulose and lignin pyrolysis. **Fuel**, v. 86, p. 1781-1788, 2007.

YILDIZ, S.; GÜMÜSKAYA, E. The effects of thermal modification on crystalline structure of cellulose in soft and hardwood. **Building and Environment**, v. 42, p. 62-67, 2007.

YAMAMOTO, H.; HORII, F. CP/MAS ^{13}C NMR analysis of the crystal transformation induced for Valonia cellulose by annealing at high temperatures. **Macromolecules**, v. 26, p. 1313-1317, 1993.

YAMAMOTO, H.; HORII, F. In situ crystallization of bacterial cellulose I. Influences of polymeric additives, stirring and temperature on the formation celluloses I α and I β as revealed by cross polarization / magic angle spinning (CP/MAS) ^{13}C NMR spectroscopy. **Cellulose**, v. 1, p. 57-66, 1994.

YANG, X.; HAN, F.; XU, C.; JIANG, S.; HUANG, L.; LIU, L.; XIA, Z. Effects of preparation methods on the morphology and properties of nanocellulose (NC) extracted from corn husk. **Industrial Crops and Products**, v. 109, p. 241-247, 2017.

YAHYA, M.; CHEN, Y.W.; LEE, H.V.; HOCK, C.C.; HASSAN, W.H.W. A new protocol for efficient and high yield preparation of nanocellulose from *Elaeis guineensis* biomass: a response surface methodology (RSM) study. **Journal of Polymers and the Environment**, v. 27, n. 4, p. 678-702, 2019.

YE, S.; YU, H.Y.; WANG, D.; ZHU, J.; GU, J. Green acid-free one-step hydrothermal ammonium persulfate oxidation of viscose fiber wastes to obtain carboxylated spherical cellulose nanocrystals for oil/water Pickering emulsion. **Cellulose**, v. 25, p. 5139-5155, 2018.

ZABOROWSKA, M.; BODIN, A.; BÄCHDAHL, H.; POPP, J.; GOLDSTEIN, A.; GATENHOLM, P.; Microporous bacterial cellulose as a potential scaffold for bone regeneration. **Acta Biomaterialia**, v. 6, p. 2540-2547, 2010.

ZHANG, T.; CHENG, Q.; YE, D.; CHANG, C. Tunicate cellulose nanocrystals reinforced nanocomposite hydrogels comprised by hybrid cross-linked networks. **Carbohydrate Polymers**, v. 169, p. 139-148, 2017.

ZHANG, Q.; BENOIT, M.; VIGIER, K.O.; BARRAULT, J.; JÉGOU, G.; PHILIPPE, M.; JÉRÔME, F. Pretreatment of microcrystalline cellulose by ultrasounds: effect of particle size in the heterogeneously-catalyzed hydrolysis of cellulose to glucose. **Green Chemistry**, v. 15, p. 963-969, 2013.

ZHANG, K.; SUN, P.; LIU, H.; SHANG, S.; SONG, J.; WANG, D. Extraction and comparison of carboxylated cellulose nanocrystals from bleached sugarcane bagasse pulp using two different oxidation methods. **Carbohydrate Polymers**, v. 138, p. 237-243, 2016.

ZHAO, H-P.; FENG, X.-Q.; GAO, H. Ultrasonic technique for extracting nanofibers from nature materials. **Applied Physics Letters**, v. 90, p. 0731121-0731122, 2007.

ZHAO, D.; LIAO, Y.; ZHANG, Z. Toxicity of ionic liquids. **Clean–soil, air, water**, v. 35, p. 42-48, 2007.

ZHAO, Y.; ZHANG, Y.; LINDSTRÖM, M.E.; LI, J. Tunicate cellulose nanocrystals: preparation, neat films and nanocomposite films with glucomannans. **Carbohydrate Polymers**, v. 117, p. 286-296, 2015.

ZHOU, Y.; LI, Z.; HU, L.; FUJI, A.; NORTH, T.H. Mechanical properties of particulate MMO/AISI 304 friction joints. **ISIJ International**, v. 35, p. 1315-1321, 1995.

APPENDIX A – Micrograph of optical microscopy of raw cellulose sources

Some examples of micrographs of optical microscopy of raw cellulose sources before HIUS are shown in Figure 49.

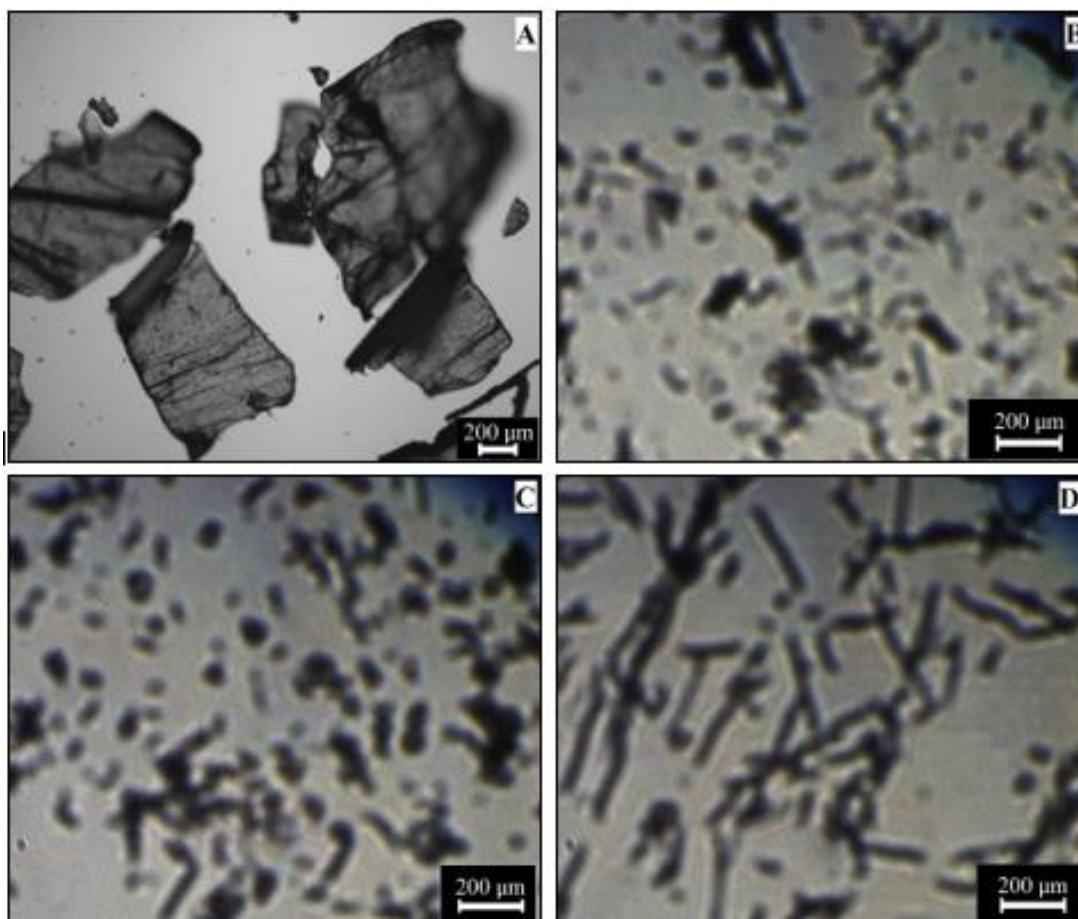


Figure 48 - Examples of micrographs of bacterial cellulose BCraw (A), curaua Crawl (B), sugarcane bagasse SCBraw (C) and viscose residue VRraw (D).

APPENDIX B – AFM micrograph of sonicated bacterial cellulose BC3

Some examples of AFM micrographs of sonicated bacterial cellulose, sample BC3, are shown in Figure 49.

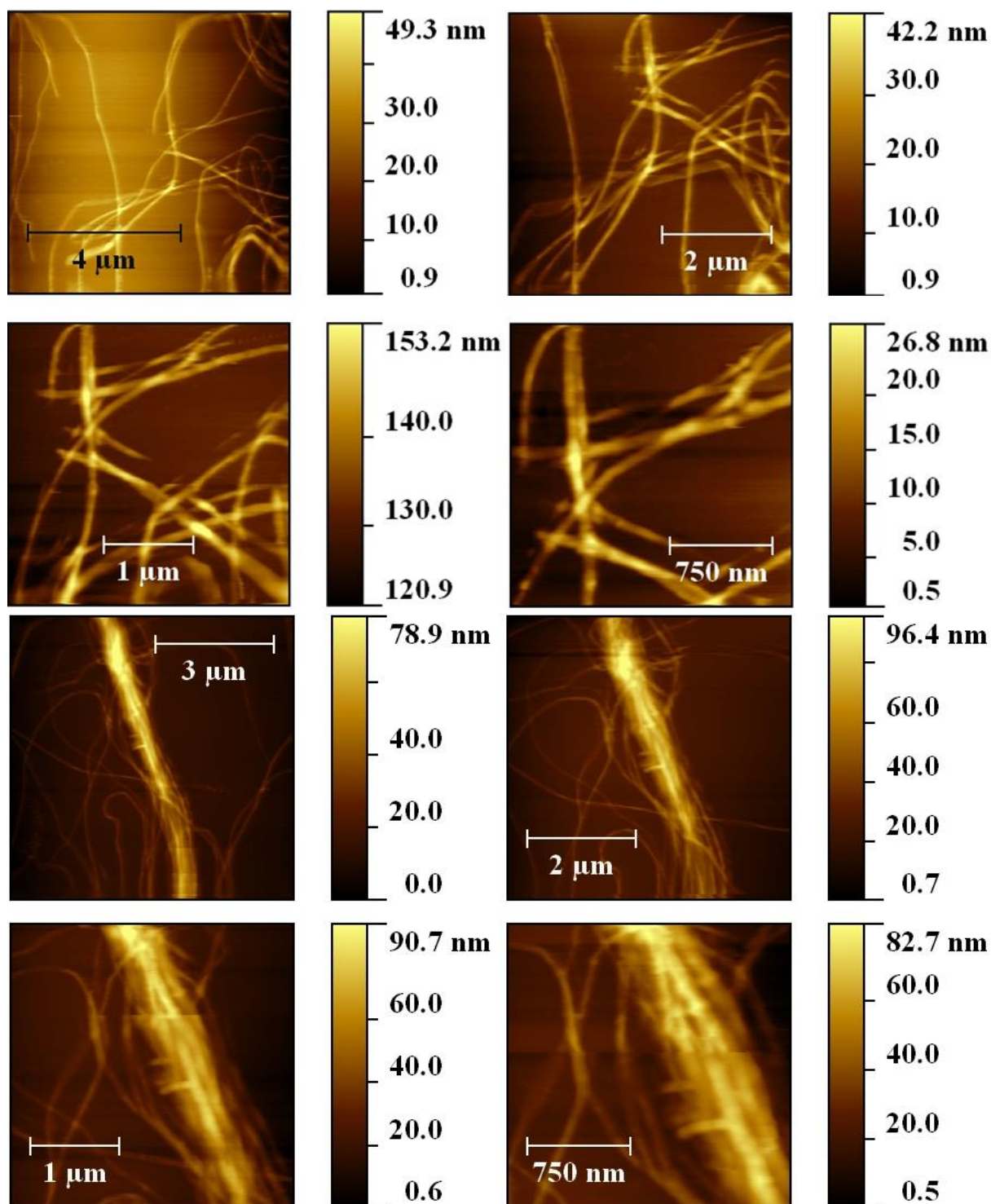


Figure 49 - AFM micrographs of topography (contact mode) of sonicated bacterial cellulose BC3.

APPENDIX C – TEM micrograph of sonicated viscose residue VR3

Some examples of TEM micrographs of sonicated viscose residue VR3 are shown in Figure 50 and Figure 51.

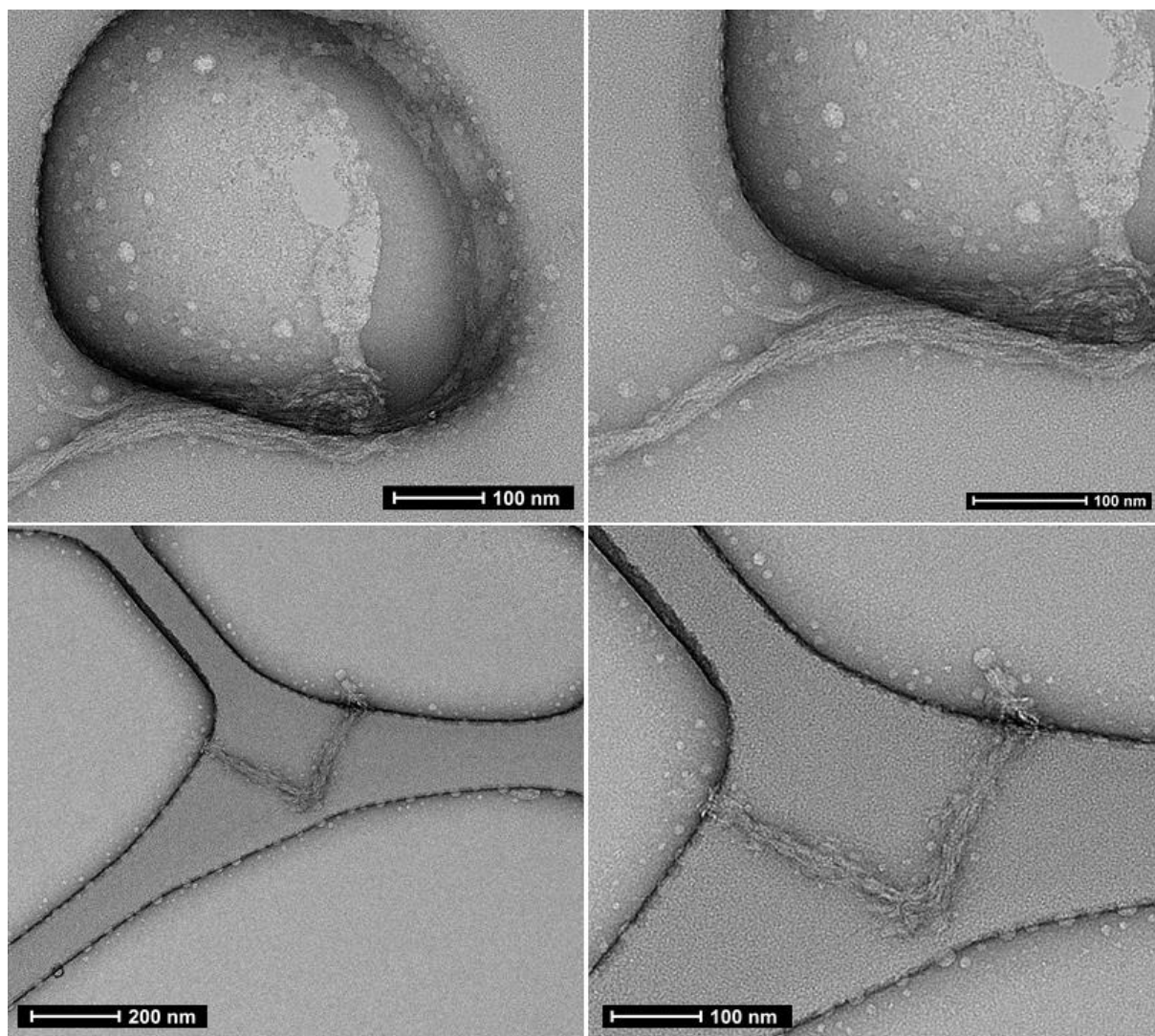


Figure 50 - TEM micrographs of sonicated viscose residue VR3.

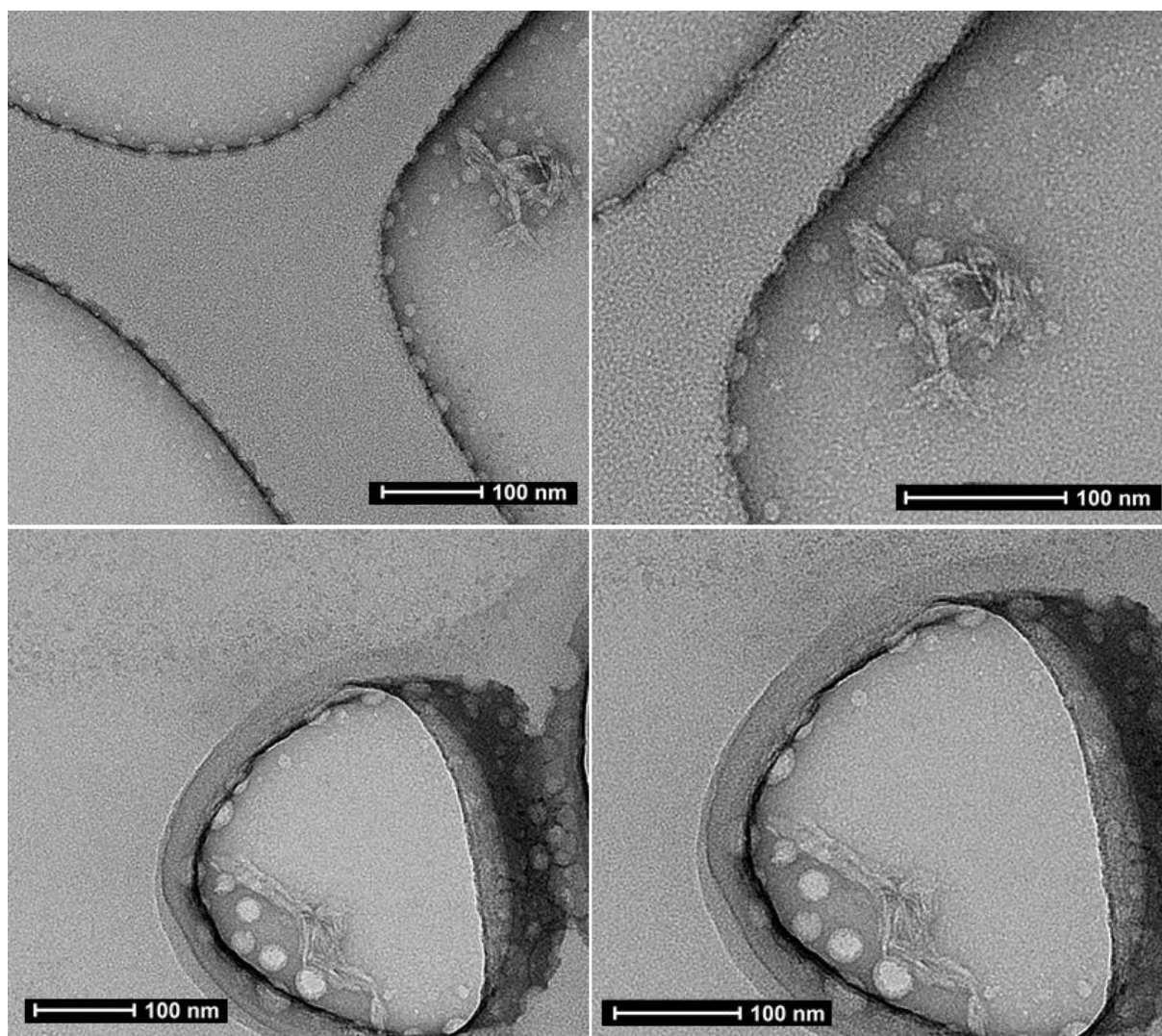


Figure 51 - TEM micrographs of sonicated viscose residue VR3.

APPENDIX D – TEM micrograph of sonicated curaua C3

Some examples of TEM micrographs of sonicated curaua C3 are shown in Figure 52 and Figure 53.

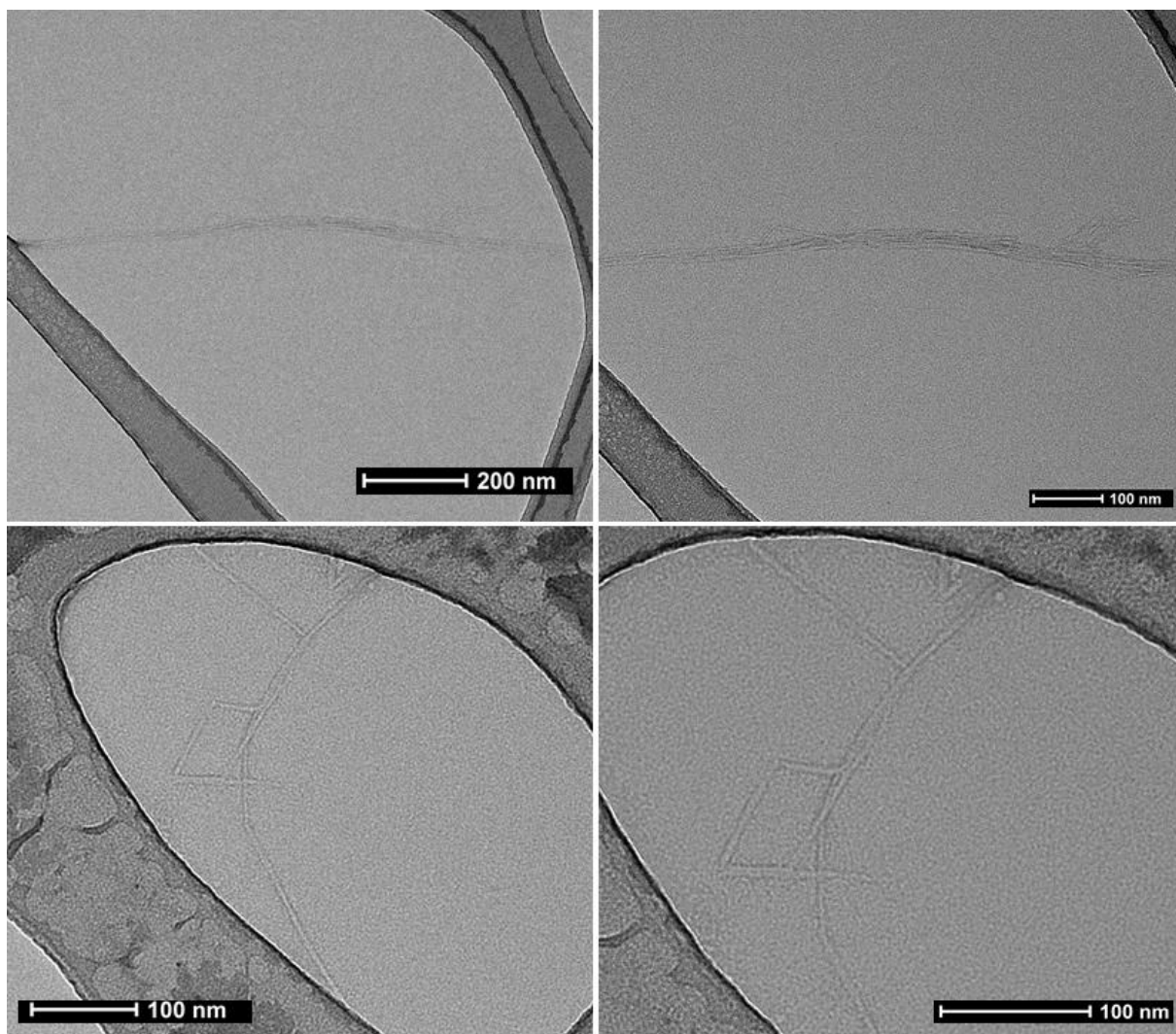


Figure 52 - TEM micrographs of sonicated curaua C3.

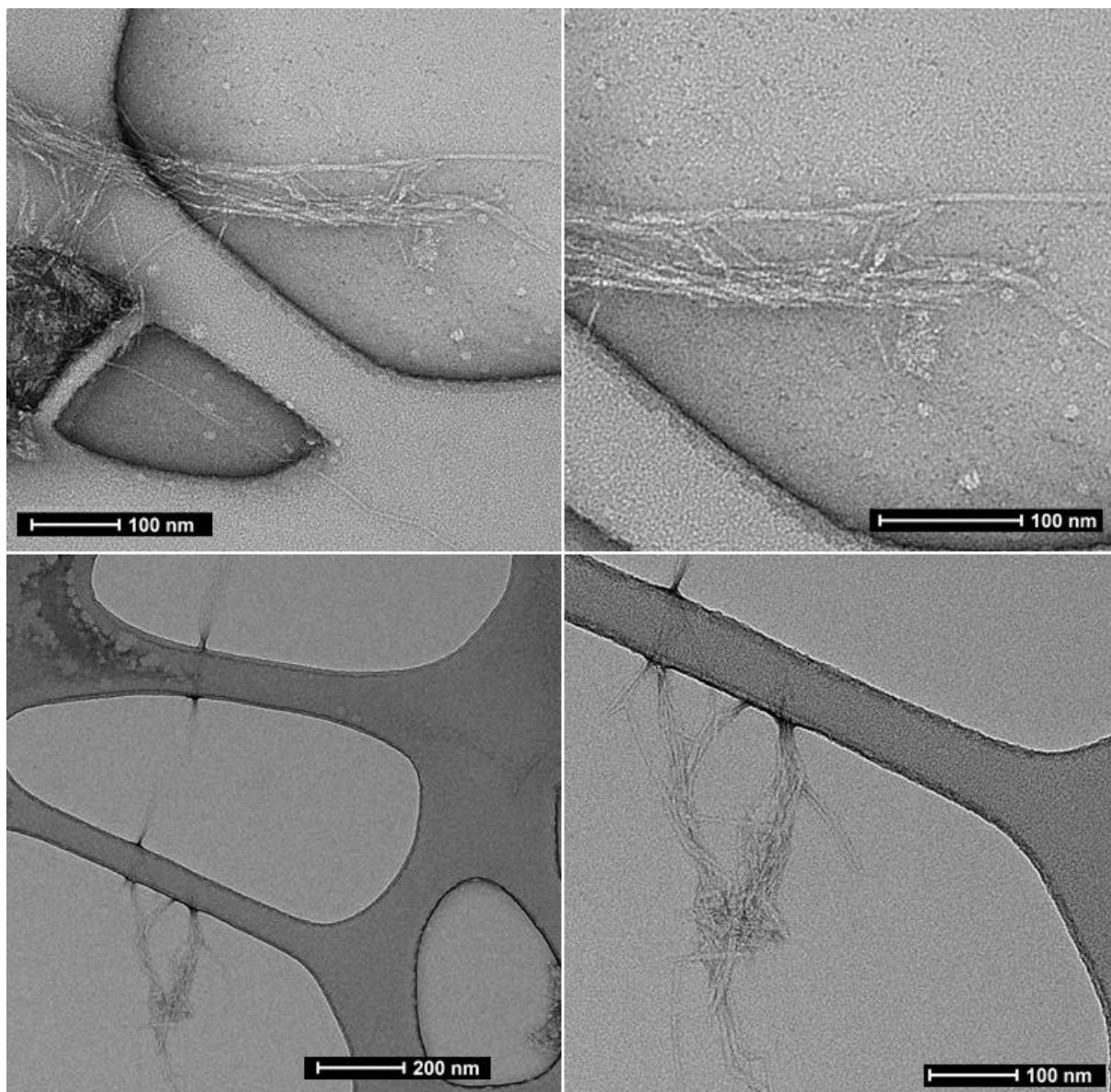


Figure 53 - TEM micrographs of sonicated curaua C3.

APPENDIX E – TEM micrograph of sonicated sugarcane bagasse SCB3

Some examples of TEM micrographs of sonicated sugarcane bagasse SCB3 are shown in Figure 54 and Figure 55.

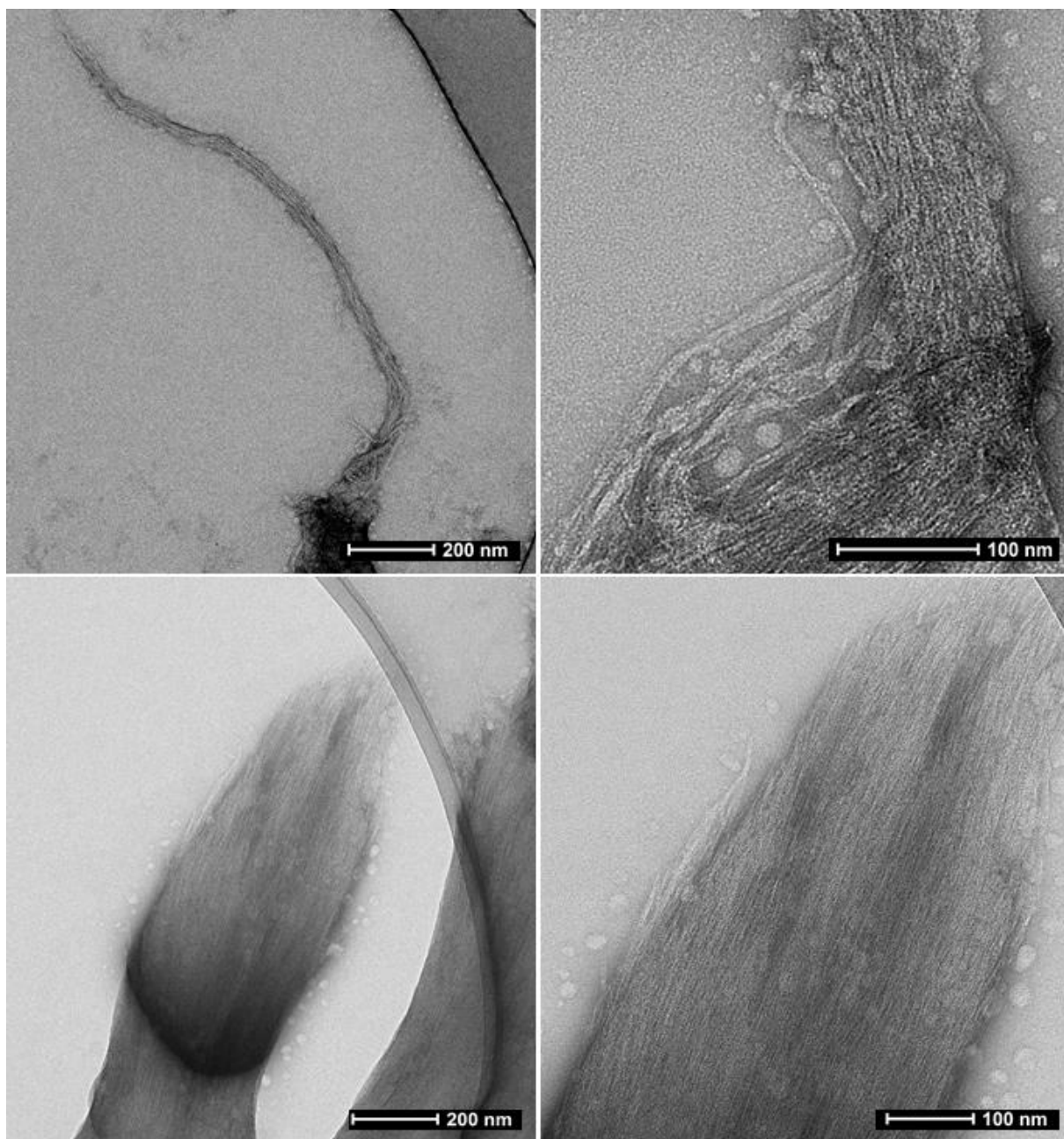


Figure 54 - TEM micrographs of sonicated sugarcane bagasse SCB3.

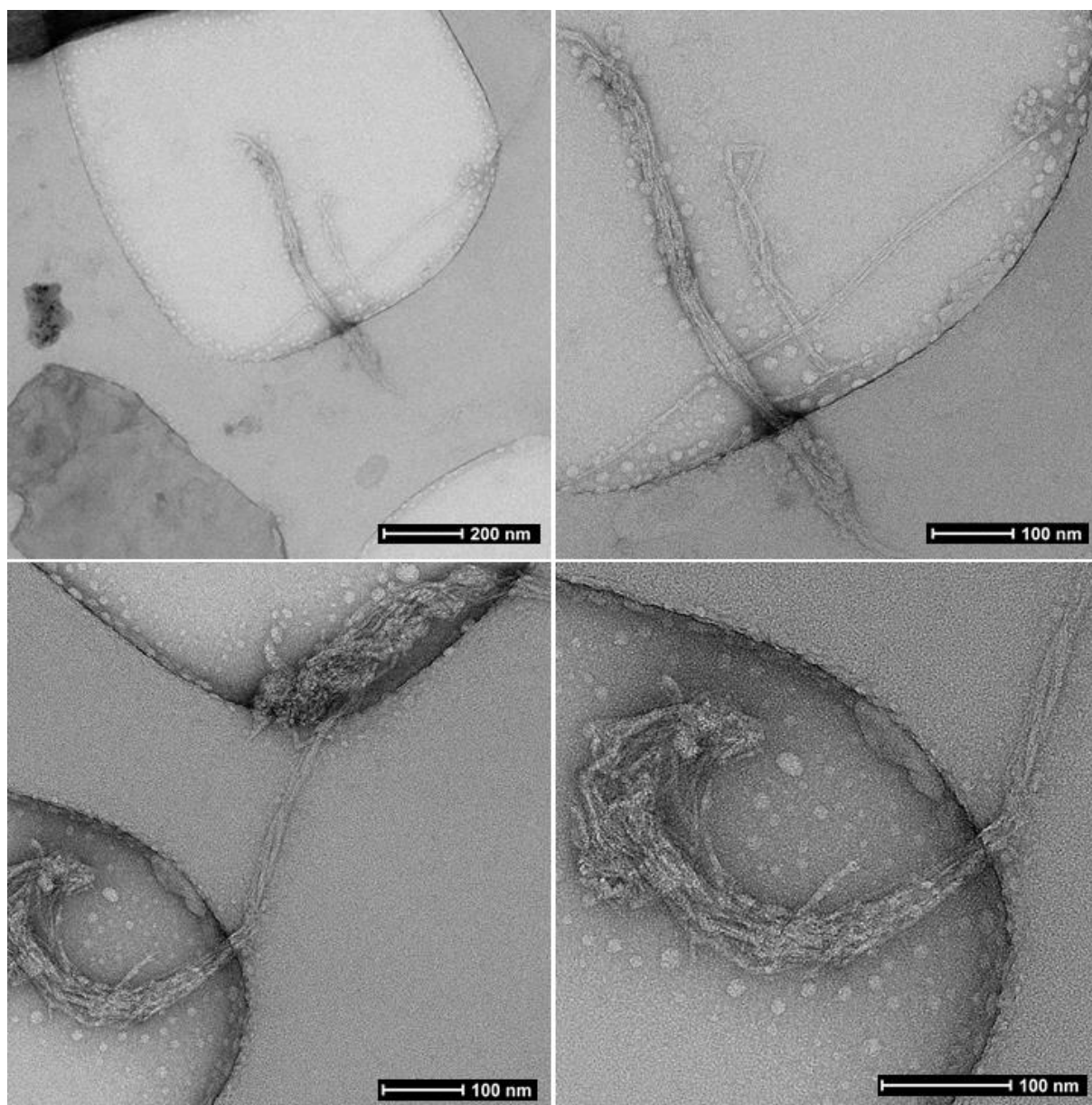


Figure 55 - TEM micrographs of sonicated sugarcane bagasse SCB3.